



Measurement of the CKM angle γ using $B_s^0 \rightarrow D_s K \pi \pi$ decays

P. d'Argent¹, E. Gersabeck², M. Kecke¹, M. Schiller³

¹*Physikalisches Institut, Ruprecht-Karls-Universität Heidelberg, Heidelberg, Germany*

²*School of Physics and Astronomy, University of Manchester, Manchester, United Kingdom*

³*School of Physics and Astronomy, University of Glasgow, Glasgow, United Kingdom*

Abstract

We present the first measurement of the weak phase $2\beta + \gamma$ obtained from a time-dependent (amplitude) analysis of $B_s^0 \rightarrow D_s K \pi \pi$ decays using proton-proton collision data corresponding to an integrated luminosity of xxx fb^{-1} recorded by the LHCb detector.

Contents

1	Introduction	1
2	Sensitivity studies	2
2.1	PDF	2
2.2	Results	4
3	Selection	7
3.1	Cut-based selection	7
3.2	Multivariate stage	8
4	Fits to invariant mass distributions of signal and normalization channel	11
4.1	Signal models for $m(D_s\pi\pi\pi)$ and $m(D_sK\pi\pi)$	11
4.2	Background models for $m(D_s\pi\pi\pi)$	12
4.3	Background models for $m(D_sK\pi\pi)$	12
4.4	Fit to $B_s^0 \rightarrow D_s\pi\pi\pi$ candidates	14
4.5	Fit to $B_s^0 \rightarrow D_sK\pi\pi$ candidates	14
4.6	Extraction of signal weights	14
5	Flavour Tagging	16
5.1	OS tagging calibration	17
5.2	SS tagging calibration	17
5.3	Tagging performance comparison between the signal and normalization channel	17
5.4	Combination of OS and SS taggers	18
6	Acceptance	21
6.1	MC corrections	21
6.1.1	Truth matching of simulated candidates	21
6.1.2	PID efficiencies	22
6.1.3	BDT efficiencies	23
6.1.4	Tracking efficiencies	24
6.2	Decay-time acceptance	25
6.2.1	Comparison of acceptance in subsamples	26
6.2.2	Results	28
6.3	Phasespace acceptance	32
7	Decay-time Resolution	33
7.1	Calibration for Run-I data	34
7.2	Calibration for Run-II data	35
7.3	Cross-checks	38
7.3.1	Kinematic dependence	38
7.3.2	DTF constraints	38
8	B_s Production Asymmetry	39
9	K^--π^+ Detection Asymmetry	40

10 Time dependent fit	44
10.1 sFit to $B_s^0 \rightarrow D_s\pi\pi\pi$ data	44
10.2 sFit to $B_s^0 \rightarrow D_sK\pi\pi$ data	44
10.3 Results	44
A Details of multivariate classifier	45
B Detailed mass fits	46
C Decay-time Resolution fits	50
D MC corrections	54
E Data distributions	59
E.1 Comparison of signal and calibration channel	59
E.2 Comparison of Run-I and Run-II data	61
E.3 Comparison of D_s final states	63
E.4 Comparison of trigger categories	65
E.5 Comparison of B_s and B_d decays	67
References	68

1 Introduction

- The weak phase γ is the least well known angle of the CKM unitary triangle. A key channel to measure γ is the time-dependent analysis of $B_s^0 \rightarrow D_s K$ decays [1], [2].
 The $B_s^0 \rightarrow D_s K\pi\pi$ proceeds at tree level via the transitions shown in Fig. 1.1 a) and b).

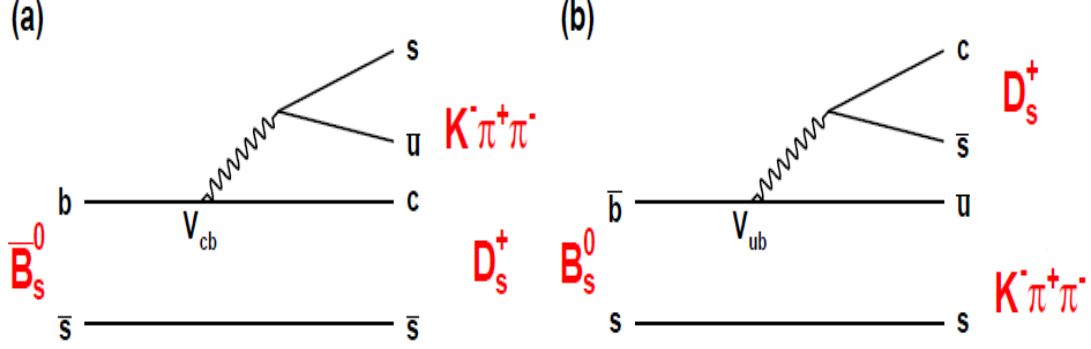


Figure 1.1: Feynman diagram of the $B_s^0 \rightarrow D_s K\pi\pi$ decay, proceeding via a) $b \rightarrow c$ transitions or b) $b \rightarrow u$ transitions.

To measure the weak CKM phase $\gamma \equiv \arg[-(V_{ud}V_{ub}^*)/(V_{cd}V_{cb}^*)]$, a decay with interference between $b \rightarrow c$ and $b \rightarrow u$ transitions at tree level is needed [1]. As illustrated in Fig. 1.1, this is the case for the presented decay mode. A measurement of γ using $B_s^0 \rightarrow D_s K\pi\pi$ decays, where the $K\pi\pi$ subsystem is dominated by excited kaon states such as the $K_1(1270)$ and $K_1(1400)$ resonances, is performed. It is complementary to the above mentioned analysis of $B_s^0 \rightarrow D_s K$, making use of a fully charged final state, where every track is detected in the vertex locator. To account for the non-constant strong phase across the Dalitz plot, one can either develop a time-dependent amplitude model or select a suitable phase-space region and introduce a coherence factor as additional hadronic parameter to the fit.

This analysis is based on the first observation of the $B_s^0 \rightarrow D_s K\pi\pi$ decay presented in [3] and [4], where its branching ratio is measured relative to $B_s^0 \rightarrow D_s \pi\pi\pi$. The result obtained by the previous analysis is $0.052 \pm 0.005 \pm 0.003$, where the uncertainties are statistical and systematical, respectively. In this note, we present a measurement of γ , making use of the full phase space by using a 6 dimensional time- and amplitude-dependent fit.

2 Sensitivity studies

2.1 PDF

First, we define the purely hadronic amplitudes for a given phasespace point x . The weak phase dependence is written latter explicitly in the pdf.

$$A(B_s^0 \rightarrow D_s^- K^+ \pi\pi) \equiv A(x) = \sum_i a_i A_i(x) \quad (2.1)$$

$$A(B_s^0 \rightarrow D_s^+ K^- \pi\pi) \equiv \bar{A}(\bar{x}) = \sum_i \bar{a}_i \bar{A}_i(\bar{x}) \quad (2.2)$$

$$A(\bar{B}_s^0 \rightarrow D_s^- K^+ \pi\pi) = \bar{A}(x) \text{ (Assuming no direct CPV)} \quad (2.3)$$

$$A(\bar{B}_s^0 \rightarrow D_s^+ K^- \pi\pi) = A(\bar{x}) \text{ (Assuming no direct CPV)} \quad (2.4)$$

The full time-dependent amplitude pdf is given by:

$$\begin{aligned} P(x, t, q_t, q_f) \propto & [(|A(x)|^2 + |\bar{A}(x)|^2) \cosh\left(\frac{\Delta\Gamma t}{2}\right) \\ & + q_t q_f (|A(x)|^2 - |\bar{A}(x)|^2) \cos(m_s t) \\ & - 2\text{Re}(A(x)^* \bar{A}(x) e^{-iq_f(\gamma-2\beta_s)}) \sinh\left(\frac{\Delta\Gamma t}{2}\right) \\ & - 2q_t q_f \text{Im}(A(x)^* \bar{A}(x) e^{-iq_f(\gamma-2\beta_s)}) \sin(m_s t)] e^{-\Gamma t} \end{aligned} \quad (2.5)$$

where $q_t = +1$ (-1) for a B_s^0 (\bar{B}_s^0) tag and $q_f = +1$ (-1) for $D_s^- K^+ \pi\pi$ ($D_s^+ K^- \pi\pi$) final states.

Integrating over the phasespace, we get

$$\begin{aligned} \int P(x, t, q_t, q_f) dx \propto & [\cosh\left(\frac{\Delta\Gamma t}{2}\right) \\ & + q_t q_f \left(\frac{1-r^2}{1+r^2}\right) \cos(m_s t) \\ & - 2 \left(\frac{\kappa r \cos(\delta - q_f(\gamma-2\beta_s))}{1+r^2}\right) \sinh\left(\frac{\Delta\Gamma t}{2}\right) \\ & - 2q_t q_f \left(\frac{\kappa r \sin(\delta - q_f(\gamma-2\beta_s))}{1+r^2}\right) \sin(m_s t)] e^{-\Gamma t} \\ = & [\cosh\left(\frac{\Delta\Gamma t}{2}\right) + q_t q_f C \cos(m_s t) - \kappa D_{q_f} \sinh\left(\frac{\Delta\Gamma t}{2}\right) - q_t \kappa S_{q_f} \sin(m_s t)] e^{-\Gamma t} \end{aligned} \quad (2.6)$$

where the C, D_{q_f}, S_{q_f} are defined exactly as for $D_s K$. The coherence factor is defined as :

$$\kappa e^{i\delta} \equiv \frac{\int A(x)^* \bar{A}(x) dx}{\sqrt{\int |A(x)|^2 dx} \sqrt{\int |\bar{A}(x)|^2 dx}} \quad (2.7)$$

$$r \equiv \frac{\sqrt{\int |\bar{A}(x)|^2 dx}}{\sqrt{\int |A(x)|^2 dx}} \quad (2.8)$$

³¹ and appears in front of the D_{q_f}, S_{q_f} terms. This means one additional fit parameter for
³² the lifetime fit. In the limit of only one contributing resonance $\kappa \rightarrow 1$.

³³

³⁴ **2.2 Results**

³⁵ Assumptions:

- ³⁶ • Use amplitudes from flavor-averaged, time-integrated fit
- ³⁷ • $r = 0.4$ (ratio of CKM elements)
- ³⁸ • PDG values for: $\tau, \Delta m_s, \Delta\Gamma, \beta_s$
- ³⁹ • $\epsilon(x, t) = \text{const.}$, perfect resolution
- ⁴⁰ • $\epsilon_{Tag} = 0.66, \langle \omega \rangle = 0.4$
- ⁴¹ • $N_{signal} = 3000$ (Run1+15/16 data)

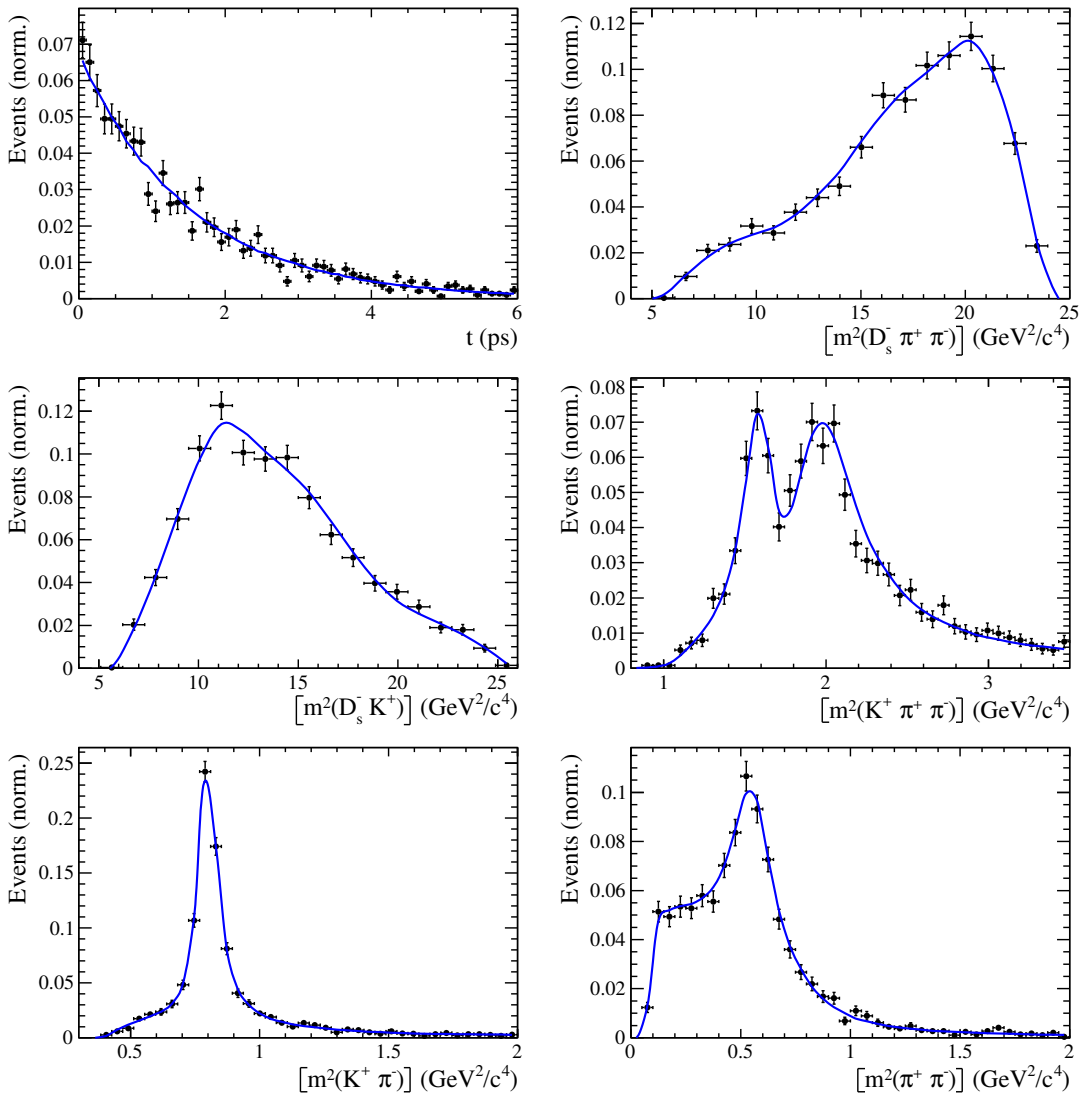
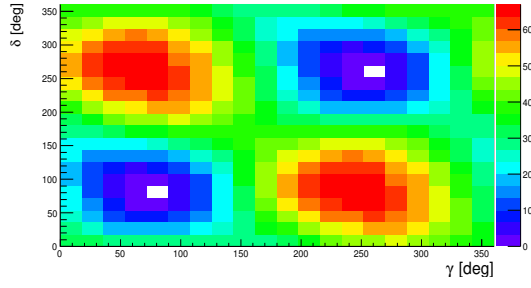


Figure 2.1: Example toy fit



Generated values:

$$\gamma = 70^\circ, \delta = 100^\circ$$

Fit result:

$$\begin{aligned} \gamma &= 74 \pm 15^\circ, \delta = 84 \pm 15^\circ \\ (\gamma &= 254 \pm 15^\circ, \delta = 264 \pm 15^\circ) \end{aligned}$$

Figure 2.2: Likelihood scan

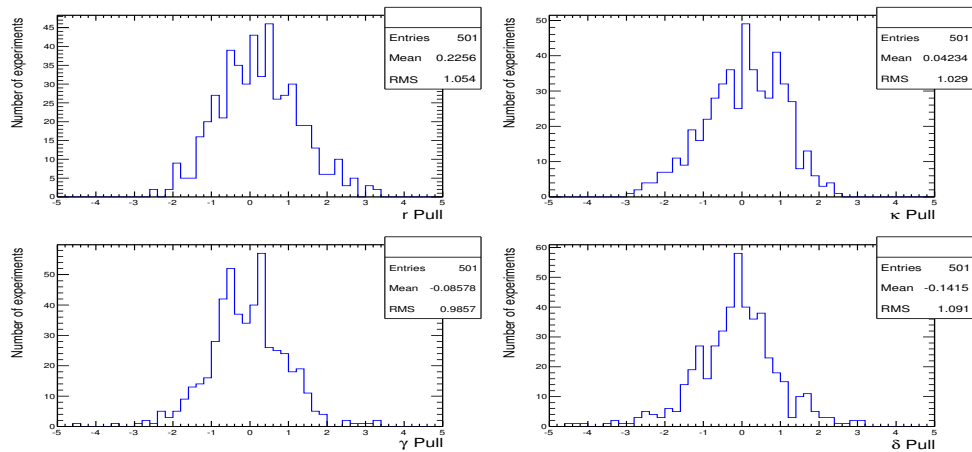


Figure 2.3: Pulls

Table 2.1

	Generated	Full PDF	Phasespace integrated
r	0.4	0.38 ± 0.06	unstable
κ	0.2	0.23 ± 0.13	0.2 (fixed)
δ	100	99 ± 22	unstable
γ	70	70 ± 17	unstable

	Generated	Full PDF	Phasespace integrated
r	0.4	0.44 ± 0.07	0.43 ± 0.11
κ	0.4	0.41 ± 0.14	0.4 (fixed)
δ	100	101 ± 19	95 ± 41
γ	70	69 ± 16	66 ± 40

	Generated	Full PDF	Phasespace integrated
r	0.4	0.41 ± 0.08	0.39 ± 0.11
κ	0.6	0.60 ± 0.13	0.6 (fixed)
δ	100	98 ± 17	92 ± 25
γ	70	68 ± 17	65 ± 28

	Generated	Full PDF	Phasespace integrated
r	0.4	0.42 ± 0.09	0.39 ± 0.09
κ	1.0	0.96 ± 0.03	1.0 (fixed)
δ	100	100 ± 17	100 ± 17
γ	70	66 ± 17	67 ± 17

42 **3 Selection**

43 For the presented analysis, we reconstruct the $B_s^0 \rightarrow D_s K\pi\pi$ decay through two different
 44 final states of the D_s meson, $D_s \rightarrow KK\pi$ and $D_s \rightarrow \pi\pi\pi$. Of those two final states
 45 $D_s \rightarrow KK\pi$ is the most prominent one, while $\mathcal{BR}(D_s \rightarrow \pi\pi\pi) \approx 0.2 \cdot \mathcal{BR}(D_s \rightarrow KK\pi)$
 46 holds for the other one.

47 A two-fold approach is used to isolate the $B_s^0 \rightarrow D_s K\pi\pi$ candidates from data passing
 48 the stripping line. First, further one-dimensional cuts are applied to reduce the level of
 49 combinatorial background and to veto some specific physical background. This stage is
 50 specific to the respective final state in which the D_s meson is reconstructed, since different
 51 physical backgrounds, depending on the respective final state, have to be taken into
 52 account. After that, a multivariate classifier is trained which combines the information
 53 of several input variables, including their correlation, into one powerful discriminator
 54 between signal and combinatorial background. For this stage, all possible D_s final states
 55 are treated equally.

56 **3.1 Cut-based selection**

57 In order to minimize the contribution of combinatorial background to our samples, we
 58 apply the following cuts to the b hadron:

- 59 • DIRA > 0.99994
- 60 • min IP $\chi^2 < 20$ to any PV,
- 61 • FD $\chi^2 > 100$ to any PV,
- 62 • Vertex $\chi^2/\text{nDoF} < 8$,
- 63 • $(Z_{D_s} - Z_{B_s^0}) > 0$, where Z_M is the z-component of the position \vec{x} of the decay vertex
 64 for the B_s^0/D_s meson.

65 Additionally, we veto various physical backgrounds, which have either the same final
 66 state as our signal decay, or can contribute via a single misidentification of $K \rightarrow \pi$ or
 67 $K \rightarrow p$. In the following, the vetoes are ordered by the reconstructed D_s final state they
 68 apply to:

69 1. All:

- 70 (a) $B_s^0 \rightarrow D_s^+ D_s^-$: $|M(K\pi\pi) - m_{D_s}| > 20$ MeV/ c^2 .
- 71 (b) $B_s^0 \rightarrow D_s^- K^+ K^- \pi^+$: possible with single missID of $K^- \rightarrow \pi^-$, rejected by
 72 requiring π^- to fulfill $\text{DLL}_{K\pi} < 5$.

73 2. $D_s \rightarrow KK\pi$

- 74 (a) $B^0 \rightarrow D^+(\rightarrow K^+\pi^-\pi^+) K\pi\pi$: possible with single missID of $\pi^+ \rightarrow K^+$, vetoed
 75 by changing particle hypothesis and recompute $|M(K^+\pi^-\pi^+) - m_{D_p}| > 30$
 76 MeV/ c^2 , or the K^+ has to fulfill $\text{DLL}_{K\pi} > 10$.

- 77 (b) $\Lambda_b^0 \rightarrow \Lambda_c^+ (\rightarrow pK^-\pi^+)K\pi\pi$: possible with single missID of $p \rightarrow K^+$, vetoed by
 78 changing particle hypothesis and recompute $M(pK^-\pi^+) - m_{\Lambda_c^+} > 30 \text{ MeV}/c^2$,
 79 or the K^+ has to fulfill $(\text{DLL}_{K\pi} - \text{DLL}_{p\pi}) > 5$.
 80 (c) $D^0 \rightarrow KK$: D^0 combined with a random π can fake a $D_s \rightarrow KK\pi$ decay and
 81 be a background to our signal, vetoed by requiring $M(KK) < 1840 \text{ MeV}/c^2$.

82 3. $D_s \rightarrow \pi\pi\pi$

- 83 (a) $D^0 \rightarrow \pi\pi$: combined with a random π can fake a $D_s \rightarrow \pi\pi\pi$ decay and be a
 84 background to our signal, vetoed by requiring both possible combinations to
 85 have $M(\pi\pi) < 1700 \text{ MeV}/c^2$.

86 The most prominent final state used in this analysis is $B_s^0 \rightarrow D_s(\rightarrow KK\pi)K\pi\pi$, where
 87 the D_s decay can either proceed via the narrow ϕ resonance, the broader K^{*0} resonance, or
 88 non resonant. Depending on the decay process being resonant or not, we apply additional
 89 PID requirements on this final state:

- 90 • resonant case:

- 91 – $D_s^+ \rightarrow \phi\pi^+$, with $|M(K^+K^-) - m_\phi| < 20 \text{ MeV}/c^2$: no additional requirements,
 92 since ϕ is narrow and almost pure K^+K^- .
- 93 – $D_s^+ \rightarrow \bar{K}^{*0}K^+$, with $|M(K^-\pi^+) - m_{K^{*0}}| < 75 \text{ MeV}/c^2$: $\text{DLL}_{K\pi} > 0$ for kaons,
 94 since this resonance is more than ten times broader than ϕ .

- 95 • non resonant case: $\text{DLL}_{K\pi} > 5$ for kaons, since the non resonant category has
 96 significant charmless contributions.

97 For the $D_s \rightarrow \pi\pi\pi$ final state, we apply global PID requirements:

- 98 • $\text{DLL}_{K\pi} < 10$ for all pions.
 99 • $\text{DLL}_{p\pi} < 10$ for all pions.

100 3.2 Multivariate stage

101 We use TMVA [5] to train a multivariate discriminator, which is used to further improve
 102 the signal to background ratio. The following variables are used for the training:

- 103 • $\max(\text{ghostProb})$ over all tracks
 104 • $\text{cone}(p_T)$ asymmetry of every track, which is defined to be the difference between the
 105 p_T of the π/K and the sum of all other p_T in a cone of radius $r = \sqrt{(\Delta\Phi)^2 + (\Delta\eta)^2}$
 106 $< 1 \text{ rad}$ around the signal π/K track.
 107 • $\min(\text{IP}\chi^2)$ over the X_s daughters
 108 • $\max(\text{DOCA})$ over all pairs of X_s daughters
 109 • $\min(\text{IP}\chi^2)$ over the D_s daughters

- D_s and B_s^0 DIRA
- D_s FD significance
- $\max(\cos(D_s h_i))$, where $\cos(D_s h_i)$ is the cosine of the angle between the D_s and another track i in the plane transverse to the beam
- B_s^0 IP χ^2 , FD χ^2 and Vertex χ^2

Various classifiers were investigated in order to select the best performing discriminator. Consequently, a boosted decision tree with gradient boost (BDTG) is chosen as nominal classifier. We use truth-matched MC as signal input. Simulated signal candidates are required to pass the same trigger, stripping and preselection requirements, that were used to select the data samples. For the background we use events from the high mass sideband ($m_{B_s^0 \text{candidate}} > 5600 \text{ MeV}/c^2$) of our data samples. As shown in Fig. 3.1, this mass region is sufficiently far away from signal structures and is expected to be dominantly composed of combinatorial background. For completeness, the mass distribution of preselected $D_s \rightarrow hh$ candidates (where $h = \pi$ or $h = K$) is also shown in Fig. 3.1.

124

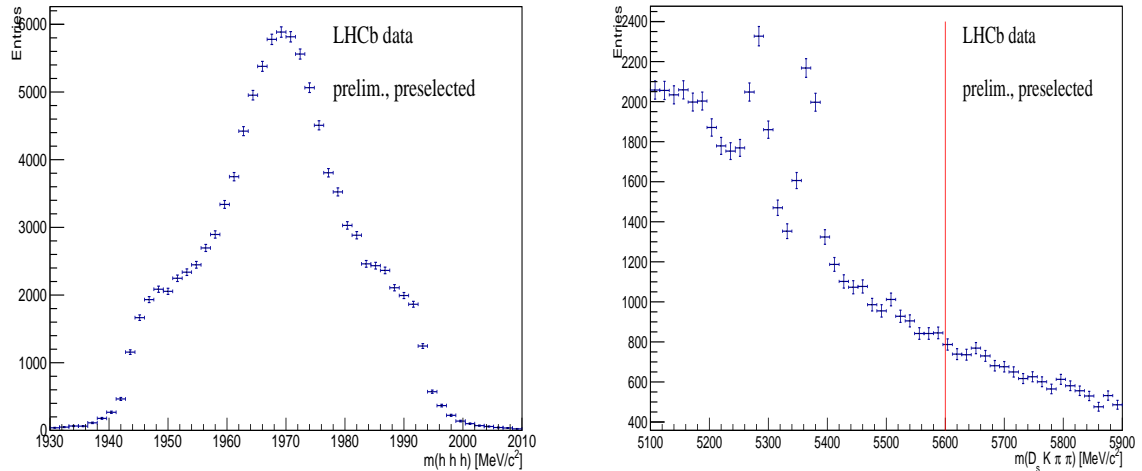


Figure 3.1: Invariant mass distribution of preselected (left) $D_s \rightarrow hh$ and (right) $B_s^0 \rightarrow D_s K\pi\pi$ candidates. For the $B_s^0 \rightarrow D_s K\pi\pi$ candidates, the region right from the red colored line with $m_{B_s^0 \text{candidate}} > 5600 \text{ MeV}/c^2$ is used as background input for the boosted decision tree.

125 The distributions of the input variables for signal and background and the BDTG
126 output distribution are shown in the appendix.

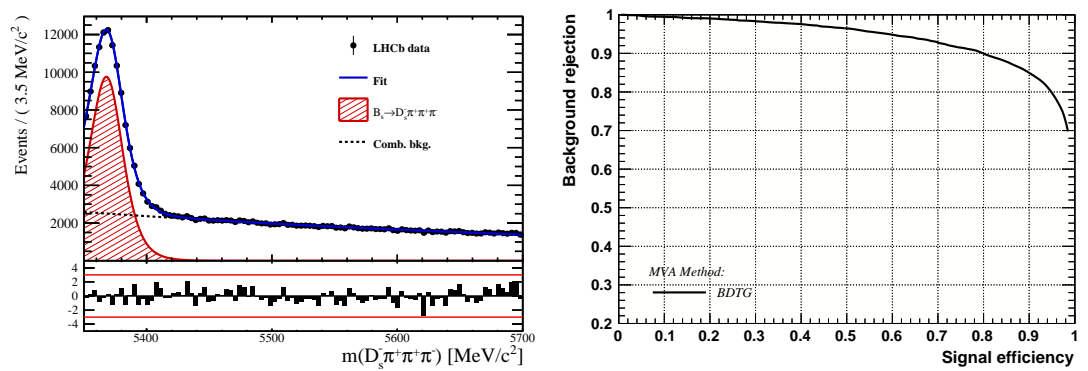


Figure 3.2

127 **4 Fits to invariant mass distributions of signal and**
 128 **normalization channel**

129 In order to properly model the invariant mass distribution of $B_s^0 \rightarrow D_s K\pi\pi$ and $B_s^0 \rightarrow$
 130 $D_s \pi\pi\pi$ candidates, the expected signal shape, as well as the expected shape for the
 131 combinatorial and physical background has to be known. This model can then be used to
 132 fit the distributions and obtain signal sWeights [6], which are employed to suppress the
 133 residual background that is still left in the sample, for the time-dependent amplitude fit.

134 **4.1 Signal models for $m(D_s \pi\pi\pi)$ and $m(D_s K\pi\pi)$**

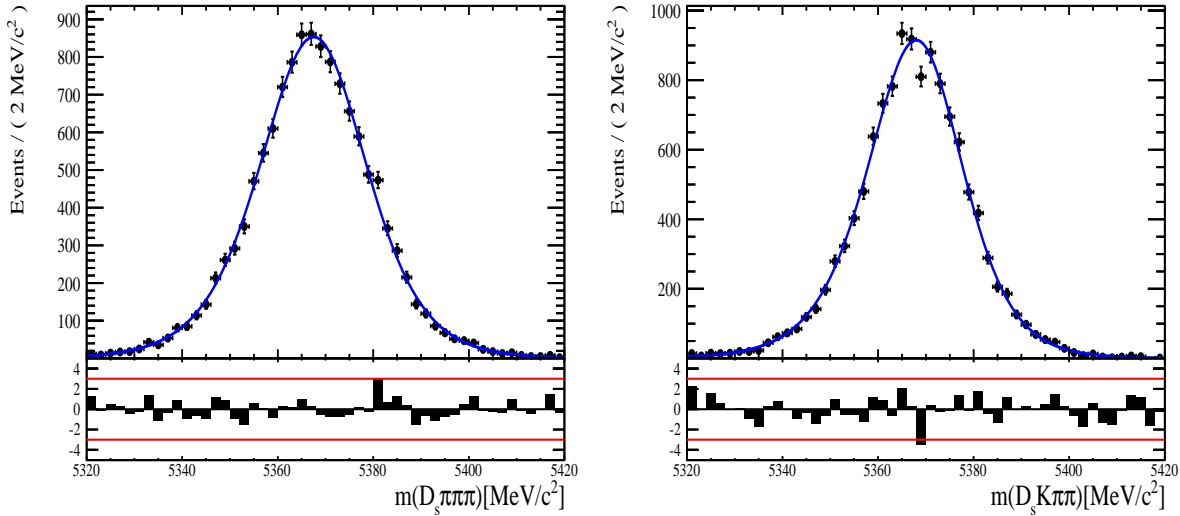


Figure 4.1: Invariant mass distributions of simulated (left) $B_s^0 \rightarrow D_s \pi\pi\pi$ and (right) $B_s^0 \rightarrow D_s K\pi\pi$ events. A fit of a RooJohnsonSU function to each distribution is overlaid.

135 The mass distribution of $B_s^0 \rightarrow D_s K\pi\pi$ signals is modeled using a Johnson SU
 136 function [7], which is a gaussian function with a Landau-like tail on one side,

$$J(m_{B_s^0}; \mu, \sigma, \gamma, \delta) = \frac{\delta}{\sigma 2\pi \sqrt{1 + (\frac{m_{B_s^0} - \mu}{\sigma})^2}} \exp\left(-\frac{1}{2}[\gamma + \delta \operatorname{Argsh}\left(\frac{m_{B_s^0} - \mu}{\sigma}\right)^2]\right). \quad (4.1)$$

137 The sign of γ in Eq. 4.1 determines whether the tail is located at lower ($\gamma > 0$)
 138 or higher ($\gamma < 0$) invariant mass values than the mean μ of the gaussian function and
 139 δ describes the (a)symmetry of the fitted distribution. Higher values of δ result in a
 140 more symmetric, gaussian-like function. Another Johnson SU function function is used
 141 to account for the contribution of the $B^0 \rightarrow D_s K\pi\pi$ decay, which is also present in
 142 the $m(D_s K\pi\pi)$ spectrum. The width, as well as the tail parameters are fixed to values
 143 obtained by a fit to the invariant mass distribution of simulated events shown in Fig 4.1.
 144 A linear scaling factor for the mean μ and width σ is floated in the fit to account for
 145 possible differences between the simulation and real data.

146 The same approach is used to describe the invariant mass distribution of $B_s^0 \rightarrow D_s \pi\pi\pi$

147 candidates. A Johnson SU function is used to model the signal, the parameters are
148 determined by a fit to the invariant mass of simulated $B_s^0 \rightarrow D_s\pi\pi\pi$ decays, shown in
149 Fig 4.1. A scale factor for the width and the mean is floated to account for differences
150 between data and MC.

151 4.2 Background models for $m(D_s\pi\pi\pi)$

152 Different background sources arise in the invariant mass spectrum of candidates in the
153 normalization mode.

154 The following backgrounds have to be accounted for:

- 155 • Combinatorial background: This contribution arises from either a real D_s , which is paired with random tracks to form the B_s^0 candidates, or via real X_d 's, which are combined with three tracks that fake a D_s candidate to form a fake B_s^0 .
- 158 • Partially reconstructed $B^0/B_s^0 \rightarrow D_s^*\pi\pi\pi$ decays, with $D_s^* \rightarrow D_s\gamma$ or $D_s^* \rightarrow D_s\pi^0$, where the γ/π^0 is not reconstructed in the decay chain.

160 In both cases of combinatorial background, the distribution in the invariant mass of
161 B_s^0 candidates is expected to be smooth and decrease with higher masses. Therefore, one
162 exponential function is used to model these contributions.

163 The shape of the $B_s^0 \rightarrow D_s^*\pi\pi\pi$ contribution is expected to be peaking in the $m(D_s\pi\pi\pi)$
164 spectrum, with large tails due to the missing momentum, which is carried away by the π^0
165 or γ . The pion or photon from $D_s^* \rightarrow D_s(\gamma/\pi^0)$ is excluded from the reconstruction. We
166 model the shape of this contribution using the sum of three bifurcated Gaussian functions.
167 The shape parameters, as well as the yield of this contribution, are directly determined
168 on data from a fit to the $m(D_s\pi\pi\pi)$ invariant mass distribution.

169 4.3 Background models for $m(D_sK\pi\pi)$

170 For the signal channel, the following background sources have to be considered:

- 171 • Combinatorial background: same contributions as discussed in Sec. 4.2.
- 172 • Partially reconstructed $B_s^0 \rightarrow D_s^*K\pi\pi$ decays, with $D_s^* \rightarrow D_s\gamma$ or $D_s^* \rightarrow D_s\pi^0$, where the γ/π^0 is not reconstructed in the decay chain.
- 174 • Partially reconstructed $B^0 \rightarrow D_s^*K\pi\pi$ decays, with $D_s^* \rightarrow D_s\gamma$ or $D_s^* \rightarrow D_s\pi^0$, where the γ/π^0 is not reconstructed in the decay chain.
- 176 • Misidentified $B_s^0 \rightarrow D_s\pi\pi\pi$ decays, where one of the pions is wrongly identified as a kaon $\pi \rightarrow K$.
- 178 • Misidentified, partially reconstructed $B_s^0 \rightarrow D_s^*\pi\pi\pi$ decays, where one of the pions is wrongly identified as a kaon $\pi \rightarrow K$ and the γ/π^0 from $D_s^* \rightarrow D_s\gamma/\pi^0$ is not reconstructed.

181 The combinatorial background is expected to be non-peaking in the spectrum of the
182 invariant mass of $B_s^0 \rightarrow D_sK\pi\pi$ candidates. An exponential function is used to model
183 this contribution.

184 The shape of the partially reconstructed background without misID is taken from our
 185 normalization channel, where it can be directly fitted by the sum of three bifurcated
 186 Gaussian functions as described above. In the signal mass fit, all shape parameters for
 187 the $B_s^0 \rightarrow D_s^* K\pi\pi$ background are fixed to the input values from our normalization fit.

188 For the contribution of the $B^0 \rightarrow D_s^* K\pi\pi$ background, the same shape is used but
 189 the means μ_i of the bifurcated gaussians are shifted down by $m_{B_s^0} - m_{B^0}$ [?]. The yields
 190 of both contributions are directly determined in the nominal fit.

191 To determine the shape of misidentified $B_s^0 \rightarrow D_s\pi\pi\pi$ candidates in the $m(D_s K\pi\pi)$
 192 spectrum, we take a truth-matched signal MC sample of our normalization channel. We
 193 then use the PIDCalib package to determine the $\pi \rightarrow K$ fake rate. For every candidate
 194 in our MC sample, a (momentum) p and (pseudorapidity) η -dependent event weight is
 195 computed and assigned. We flip the particle hypothesis from pion to kaon for the π with
 196 the biggest miss-ID weight for each event and recompute the invariant B_s^0 mass. This
 197 distribution is then modeled using two Crystal Ball functions. The distribution and the
 198 fit are shown in Fig. 4.2(left).

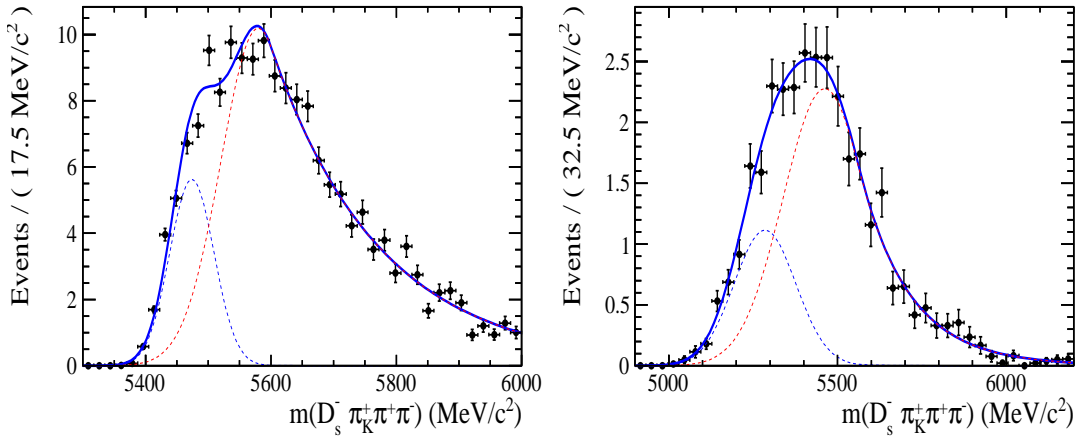


Figure 4.2: Invariant mass distribution of (left) simulated $B_s^0 \rightarrow D_s\pi\pi\pi$ events, where one of the π 's is reconstructed as a K and the misID probability for each event is taken into account. The corresponding distribution for simulated $B_s^0 \rightarrow D_s^*\pi\pi\pi$ events, where the γ/π^0 from the D_s^* is excluded from reconstruction, is shown on the right. The solid, black curve on each plot corresponds to the fit consisting of two Crystal Ball functions.

199 The expected yield of misidentified $B_s^0 \rightarrow D_s\pi\pi\pi$ candidates in the $m(D_s K\pi\pi)$ spec-
 200 trum is computed by multiplying the fake probability of $\propto 3.2\%$, which is derived from
 201 PIDCalib, by the yield of $B_s^0 \rightarrow D_s\pi\pi\pi$ signal candidates, determined in the nominal
 202 mass fit of our normalization channel.

203 In the same way as mentioned above, we can determine the rate of misidentified, partially
 204 reconstructed $B_s^0 \rightarrow D_s^*\pi\pi\pi$ decays in our sample of $B_s^0 \rightarrow D_s K\pi\pi$ decays using PIDCalib
 205 and a MC sample of $B_s^0 \rightarrow D_s^*\pi\pi\pi$ events. The invariant mass distribution we obtain
 206 when we exclude the γ/π^0 , flip the the particle hypothesis $\pi \rightarrow K$ and apply the event
 207 weights given by the fake rate, is shown in Fig. 4.2 (right). The fit of two Crystal Ball
 208 functions to this distribution is overlaid. The yield of this contribution is determined
 209 from the yield of $B_s^0 \rightarrow D_s^*\pi\pi\pi$ candidates in the nominal mass fit of our normalization
 210 channel, multiplied by the misID probability of $\propto 3.6\%$.

211 4.4 Fit to $B_s^0 \rightarrow D_s\pi\pi\pi$ candidates

212 An unbinned maximum likelihood fit is performed simultaneously to the invariant mass
 213 distribution of $B_s^0 \rightarrow D_s\pi\pi\pi$ candidates. As discussed in Sec. ??, the fit is given
 214 as a Johnson SU signal model for the B_s^0 and B^0 signal, the sum of three bifurcated
 215 Gaussian functions to model the partially reconstructed $B_s^0 \rightarrow D_s^*\pi\pi\pi$ background and
 216 an Exponential function to account for combinatorial background. The invariant mass
 217 distribution and the fit is shown in Fig. 4.3. All simultaneously performed fits to the
 218 $m(D_s\pi\pi\pi)$ distribution, ordered by the respective D_s final state, can be found in the
 219 Appendix ???. The obtained yields are summarized in Table 4.1.

220 4.5 Fit to $B_s^0 \rightarrow D_sK\pi\pi$ candidates

221 The shape of the invariant mass distribution of $B_s^0 \rightarrow D_sK\pi\pi$ candidates is described by
 222 Johnson SU functions for the B^0 and B_s^0 signal, two sums of three bifurcated Gaussians
 223 for the $B_s^0/B^0 \rightarrow D_s^*K\pi\pi$ partially reconstructed background contributions and two
 224 sums of double Crystal Ball functions for the single misID $B_s^0 \rightarrow D_s\pi\pi\pi$ and the partially
 225 reconstructed, misidentified $B_s^0 \rightarrow D_s^*\pi\pi\pi$ decays. A simultaneous unbinned maximum
 226 likelihood fit is performed and the result is shown in Fig. 4.3. All simultaneously performed
 227 fits to the $m(D_sK\pi\pi)$ distribution, ordered by the respective D_s final state, can be found
 228 in the Appendix ???. The obtained yields are summarized in Table 4.1.

229 4.6 Extraction of signal weights

230 The sPlot technique [6] is used to extract signal weights from the fits to the invariant
 231 mass distributions of our signal and normalization channel. This statistical tool assigns
 232 a weight to every event, according to its position in the respective mass distribution,
 233 given the fitted signal and background models. The weights can then be used to suppress
 234 the background components in every other observable distribution of interest. Figure ??
 235 shows the distribution of weights across the invariant mass spectra of $B_s^0 \rightarrow D_s\pi\pi\pi$ and
 236 $B_s^0 \rightarrow D_sK\pi\pi$ candidates.

fit component	yield 2011	yield 2012	yield 2015	yield 2016
$m(D_sK\pi\pi)$				
$B_s^0 \rightarrow D_sK\pi\pi$	392 ± 25	860 ± 38	309 ± 21	1984 ± 55
$B^0 \rightarrow D_sK\pi\pi$	276 ± 26	692 ± 41	261 ± 23	1385 ± 58
$B^0/B_s^0 \rightarrow D_s^*K\pi\pi$	7 ± 25	171 ± 75	114 ± 25	893 ± 84
$B_s^0 \rightarrow D_s^{(*)}\pi\pi\pi$	63 ± 0	158 ± 0	53 ± 0	314 ± 0
combinatorial	1482 ± 53	2884 ± 100	605 ± 43	4261 ± 133
$m(D_s\pi\pi\pi)$				
$B_s^0 \rightarrow D_s\pi\pi\pi$	9183 ± 105	22083 ± 166	7574 ± 95	43773 ± 245
$B^0 \rightarrow D_s\pi\pi\pi$	289 ± 58	716 ± 95	229 ± 54	968 ± 147
$B_s^0 \rightarrow D_s^*\pi\pi\pi$	3640 ± 130	9086 ± 232	3047 ± 110	17827 ± 421
combinatorial	4991 ± 154	11127 ± 271	3728 ± 126	24589 ± 500

Table 4.1: Summary of yields obtained from the fits to Run1 and Run2 data.

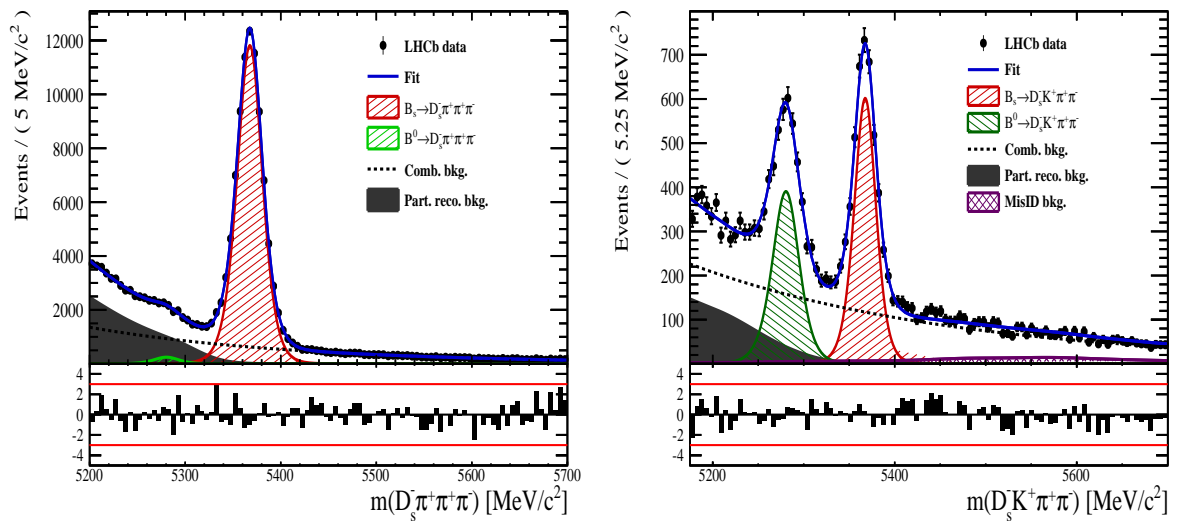


Figure 4.3: Invariant mass distribution of (left) $B_s^0 \rightarrow D_s \pi^+ \pi^+ \pi^-$ and (right) $B_s^0 \rightarrow D_s K^+ \pi^+ \pi^-$ candidates for Run1 and Run2 data. The respective fit described in the text is overlaid.

237 5 Flavour Tagging

238 To successfully perform a time- and amplitude-dependent measurement of γ , the identifi-
 239 cation of the initial state flavour of the B_s^0 meson is crucial. In the presented analysis,
 240 a number of flavour tagging algorithms are used that either determine the flavour of
 241 the non-signal b-hadron produced in the event (opposite site, OS), or they use particles
 242 produced in the fragmentation of the signal candidate B_s^0/\bar{B}_s^0 (same side, SS).

243 For the same side, the algorithm searching for the charge of an additional kaon that accom-
 244 panies the fragmentation of the signal candidate is used (SS-nnetKaon). For the opposite
 245 site, four different taggers are chosen: The Two algorithms that use the charge of an
 246 electron or a muon from semileptonic B decays (OS- e,μ), the tagger that uses the charge
 247 of a kaon from a $b \rightarrow c \rightarrow s$ decay chain (OS-nnetKaon) and the algorithm that determines
 248 the B_s^0/\bar{B}_s^0 candidate flavour from the charge of a secondary vertex, reconstructed from
 249 the OS b decay product (OS-VtxCharge). All four taggers are then combined into a signal
 250 OS tagger.

251 Every single tagging algorithm is prone to misidentify the signal candidate at a certain
 252 mistag rate $\omega = (\text{wrongtags})/(\text{alltags})$. This might be caused by particle misidentifica-
 253 tion, flavour oscillation of the neutral opposite site B-meson or by tracks that are wrongly
 254 picked up from the underlying event. For every signal B_s^0/\bar{B}_s^0 candidate, each tagging
 255 algorithm predicts a mistag probability η , which is calculated using a combination of
 256 inputs such as the kinematics of the tagging particles. The inputs are then combined
 257 to a predicted mistag using neural networks. These are trained on simulated samples
 258 of $B_s^0 \rightarrow D_s^- \pi^+$ (SS algorithm) and $B^+ \rightarrow J/\psi K^+$ (OS algorithms) decays. For the
 259 presented analysis, the measurable CP-violating coefficients are damped by the tagging
 260 dilution D , that depends on the mistag rate:

$$D = 1 - 2\omega. \quad (5.1)$$

261 This means that the statistical precision, with which these coefficients can be measured,
 262 scales as the inverse square root of the effective tagging efficiency,

$$\epsilon_{eff} = \epsilon_{tag}(1 - 2\omega)^2, \quad (5.2)$$

263 where ϵ_{tag} is the fraction of events that have a tagging decision. The flavour
 264 tagging algorithms are optimised for highest ϵ_{eff} on data, using the $B_s^0 \rightarrow D_s^- \pi^+$ and
 265 $B^+ \rightarrow J/\psi K^+$ samples.

266 Utilizing flavour-specific final states, the predicted mistag η of each tagger has to be
 267 calibrated to match the observed mistag ω on the data sample. For the calibration, a
 268 linear model of the form

$$\omega(\eta) = p_0 + p_1 \cdot (\eta - \langle \eta \rangle), \quad (5.3)$$

269 where the values of p_0 and p_1 are determined using the $B_s^0 \rightarrow D_s \pi \pi \pi$ normalization
 270 mode and $\langle \eta \rangle$ is the average estimated mistag probability $\langle \eta \rangle = \sum_{i=1}^{N_{cand}} (\eta_i)/N_{cand}$.
 271 Following this model, a perfectly calibrated tagger would lead to $\omega(\eta) = \eta$ and one would
 272 expect $p_1 = 1$ and $p_0 = \langle \eta \rangle$. Due to the different interaction cross-sections of oppositely
 273 charged particles, the tagging calibration parameters depend on the initial state flavour of
 274 the B_s^0 . Therefore, the flavour asymmetry parameters Δp_0 , Δp_1 and $\Delta \epsilon_{tag}$ are introduced.
 275 For this analysis, the calibrated mistag is treated as per-event variable, giving a larger

weight to events that are less likely to have an incorrect tag. This adds one additional observable to the time- and amplitude-dependent fit.
 The tagging calibration is determined using a time-dependent fit to the full $B_s^0 \rightarrow D_s\pi\pi\pi$ sample, where the mixing frequency Δm_s is fixed to the nominal PDG value [8]. The calibration procedure for the OS tagging algorithms (Sec.5.1) and the SS kaon tagger (Sec.5.2) is applied on the full Run I and 2015 and 2016 Run II $B_s^0 \rightarrow D_s\pi\pi\pi$ data sample, which is selected following the steps described in Sec. 3. The similar selection ensures as close as possible agreement between the $B_s^0 \rightarrow D_s\pi\pi\pi$ and $B_s^0 \rightarrow D_sK\pi\pi$ samples in terms of the decay kinematics, which are crucial for the flavour tagging. Section 5.3 shows the compatibility of both samples. After applying the calibration, the response of the OS and SS taggers are combined, which is shown in Sec. 5.4.

5.1 OS tagging calibration

The responses of the OS electron, muon, neural net kaon and the secondary vertex charge taggers are combined for the mistag calibration. Figure ?? shows the distribution of the predicted OS mistag for signal candidates from $B_s^0 \rightarrow D_s\pi\pi\pi$. The extracted calibration parameters and tagging asymmetries are summarized in Table 5.1 and the measured tagging power for the OS combination is $\epsilon_{eff,OS} = 4.81\%$.

p_0	p_1	$<\eta>$	ϵ_{tag}	Δp_o	Δp_1	$\epsilon_{eff} [\%]$
0.025 ± 0.005	0.944 ± 0.048	0.347	0.517 ± 0.002	0.028 ± 0.005	0.037 ± 0.045	$4.81 \pm 0.04 (\text{stat}) \pm 0.37 (\text{cal})$

Table 5.1: Calibration parameters and tagging asymmetries of the OS tagger extracted from $B_s^0 \rightarrow D_s\pi\pi\pi$ decays.

5.2 SS tagging calibration

The SS neural net kaon tagger can be calibrated using the flavour-specific $B_s^0 \rightarrow D_s\pi\pi\pi$ decay. It's development, performance and calibration is described in detail in [9]. Figure ?? shows the distribution of the predicted mistag of the neural net kaon tagger. The extracted calibration parameters and tagging asymmetries are summarized in Table 5.2 and the measured tagging power for this algorithm is $\epsilon_{eff,SS} = 3.22\%$.

p_0	p_1	$<\eta>$	ϵ_{tag}	Δp_o	Δp_1	$\epsilon_{eff} [\%]$
0.008 ± 0.004	1.086 ± 0.059	0.381	0.571 ± 0.002	-0.017 ± 0.004	0.135 ± 0.058	$3.22 \pm 0.03 (\text{stat}) \pm 0.26 (\text{cal})$

Table 5.2: Calibration parameters and tagging asymmetries of the SS tagger extracted from $B_s^0 \rightarrow D_s\pi\pi\pi$ decays.

5.3 Tagging performance comparison between the signal and normalization channel

To justify the usage of the tagging calibration, obtained using the $B_s^0 \rightarrow D_s\pi\pi\pi$ sample, for our signal decay, the performance of the taggers in the two decay channels needs to be compatible. This is verified using both, simulated signal samples of both decays and

sweighted data, to compare the similarity of the mistag probabilities, tagging decisions and kinematic observables that are correlated with the tagging response, on simulation and data.

The distributions of the predicted mistag probability η for the OS combination and the SS kaon tagger are shown in Fig. ?? (simulation) and Fig. 5.1 (data).

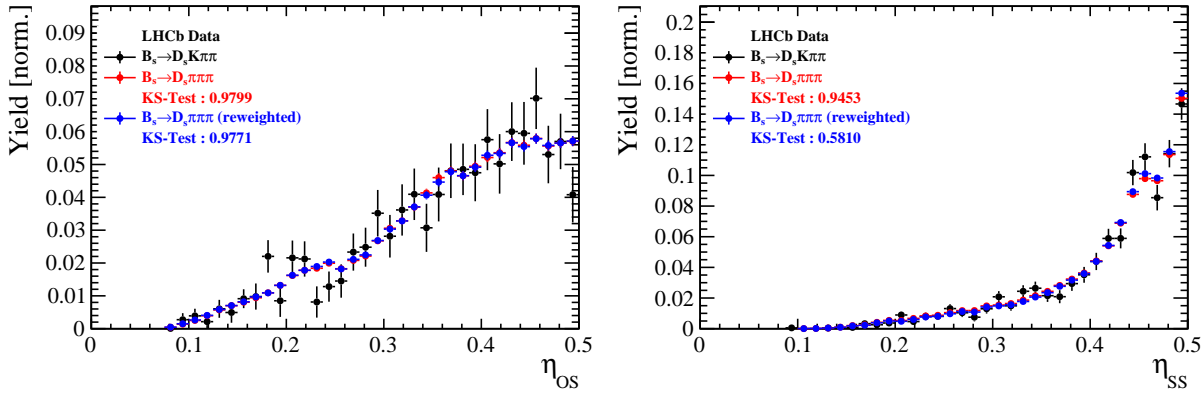


Figure 5.1: Distributions of the predicted mistag η for the OS combination (left) and the SS kaon tagger (right) for signal candidates in the $B_s^0 \rightarrow D_s K\pi\pi$ (black) and $B_s^0 \rightarrow D_s \pi\pi\pi$ (red) data samples.

Both, data and simulated samples, show good agreement between the signal and normalization channel. Compatibility is also seen in Fig. ??, which shows the comparison of the tagging decision distributions of the OS and SS tagger for sweighted data.

Fig. ?? shows the signal data distributions of the transverse B_s^0 momentum p_T , the pseudorapidity η of the signal candidate and the number of reconstructed tracks per event. Sufficient agreement is observed.

To justify the portability of the flavour tagging calibration obtained from $B_s^0 \rightarrow D_s \pi\pi\pi$ to the $B_s^0 \rightarrow D_s K\pi\pi$ channel, besides the good agreement of the distributions shown above, the dependence of the measured mistag ω on the predicted mistag η has to be compatible in both channel. This dependence is shown in Fig. 5.2 for simulated signal events of both channels, where good agreement is observed.

5.4 Combination of OS and SS taggers

In the time- and amplitude-dependent fit to $B_s^0 \rightarrow D_s K\pi\pi$ data, the obtained tagging responses of the OS and SS tagger will be combined after the calibration described in the previous sections is applied. Events that acquire a mistag probability greater than 0.5 after the calibration will have their tagging decision flipped. For events where only one of the two taggers fired, the combination of the tagging decision is trivial. In those events where both taggers made a decision, we use the standard combination of taggers [10] provided by the flavour tagging group. In the nominal fit, the calibrated mistags ω are combined event by event for the OS and SS tagger, thus adding one variable to observable to the fit procedure. This ensures that the uncertainties of the OS and SS tagging calibration parameters are propagated properly to the combined tagging response for each event. The tagging performance for the combined tagger in the categories SS tagged only, OS

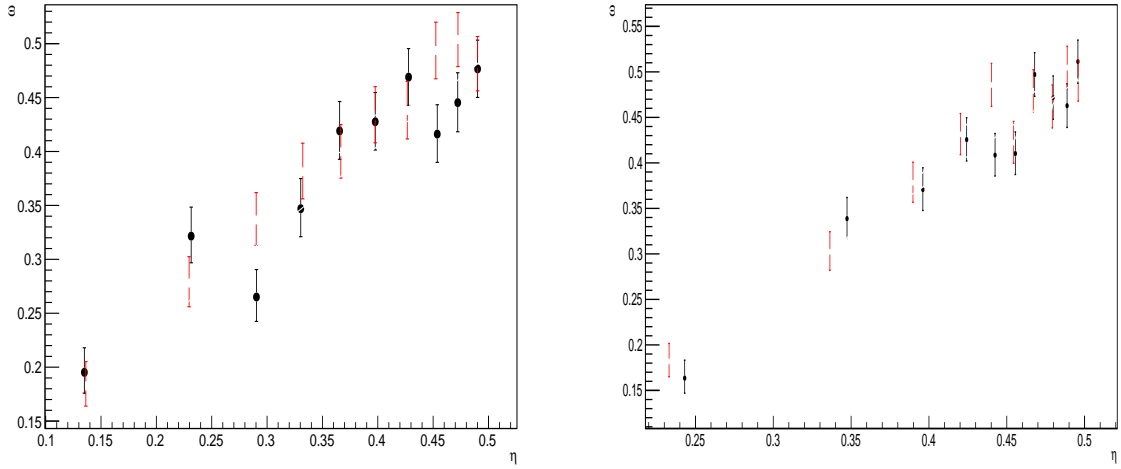


Figure 5.2: Dependence of the observed mistag ω on the predicted mistag η for the (left) OS combination and the (right) SS kaon tagger, found in the simulated $B_s^0 \rightarrow D_s K\pi\pi$ (black) and $B_s^0 \rightarrow D_s \pi\pi\pi$ (red) signal samples.

332 tagged only and SS+OS tagged, are shown in Tab. 5.4 for the signal and normalization
 333 channel. The distribution of the observed mistag ω as a function of the combined mistag
 334 probability η for $B_s^0 \rightarrow D_s \pi\pi\pi$ decays is shown in Fig. 5.3.

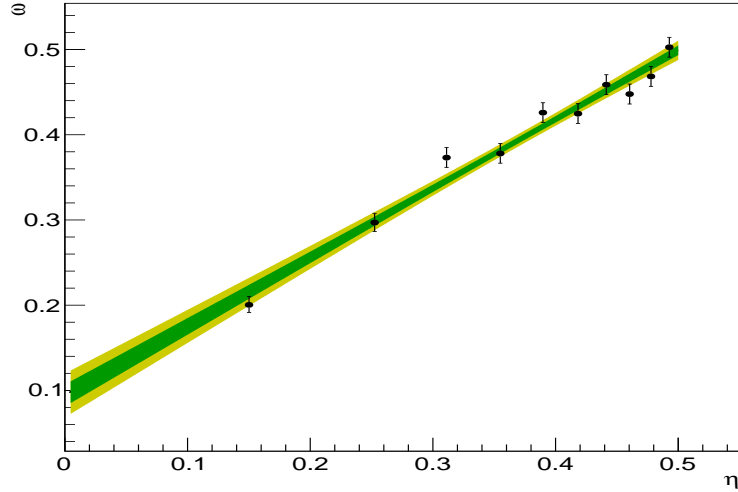


Figure 5.3: Distribution of the predicted combined mistag probability η versus the observed mistag ω for $B_s^0 \rightarrow D_s \pi\pi\pi$ signal candidates. The fit with a linear polynomial, used to determine p_0 and p_1 is overlaid.

$B_s^0 \rightarrow D_s\pi\pi\pi$		ϵ_{tag}	ϵ_{eff}
SS only		$(28.586 \pm 0.165)\%$	$(1.408 \pm 0.018(\text{stat}) \pm 0.082(\text{cal}))\%$
OS only		$(17.221 \pm 0.138)\%$	$(2.027 \pm 0.029(\text{stat}) \pm 0.100(\text{cal}))\%$
SS+OS		$(39.981 \pm 0.179)\%$	$(5.690 \pm 0.047(\text{stat}) \pm 0.196(\text{cal}))\%$
total			
$B_s^0 \rightarrow D_sK\pi\pi$		ϵ_{tag}	ϵ_{eff}
SS only		$(30.094 \pm 0.960)\%$	$(1.379 \pm 0.082(\text{stat}) \pm 0.085(\text{cal}))\%$
OS only		$(18.923 \pm 0.819)\%$	$(1.768 \pm 0.121(\text{stat}) \pm 0.099(\text{cal}))\%$
SS+OS		$(27.277 \pm 0.932)\%$	$(3.914 \pm 0.194(\text{stat}) \pm 0.220(\text{cal}))\%$
total			

Table 5.3: Flavour tagging performances for $B_s^0 \rightarrow D_s\pi\pi\pi$ and $B_s^0 \rightarrow D_sK\pi\pi$ events which are only OS tagged, only SS tagged or tagged by both.

335 6 Acceptance

336 6.1 MC corrections

337 6.1.1 Truth matching of simulated candidates

338 We use the `BackgroundCategory` tool to truth match our simulated candidates. Candidates
 339 with background category (`BKGCAT`) 20 or 50 are considered to be true signal. Background
 340 category 60 is more peculiar since it contains both badly reconstructed signal candidates
 341 and ghost background. This is due to the fact that the classification algorithms identifies
 342 all tracks for which less than 70% of the reconstructed hits are matched to generated
 343 truth-level quantities as ghosts. In particular for signal decays involving many tracks (as
 344 in our case), this arbitrary cutoff is not 100% efficient. Moreover, the efficiency is expected
 345 to depend on the kinematics which would lead to a biased acceptance determination if
 346 candidates with `BKGCAT`= 60 would be removed.

347 We therefore include `BKGCAT`= 60 and statistically subtract the ghost background by
 348 using the `sPlot` technique. The `sWeights` are calculated from a fit to the reconstructed B_s
 349 mass. The signal contribution is modeled as described in Sec. 4.1 and the background
 350 with a polynomial. The fit is performed simultaneously in two categories; the first includes
 351 events with `BKGCAT` = 20 or 50 and the second events with `BKGCAT` = 60. To account
 352 for the different mass resolution we use a different σ for each category, while the mean
 353 and the tail parameters are shared between them. The background component is only
 354 included for the second category.

355 A significant fraction of 8% of the true signal candidates are classified as ghosts, while
 356 only 20% of the events classified with `BKGCAT`= 60 are indeed genuine ghosts.

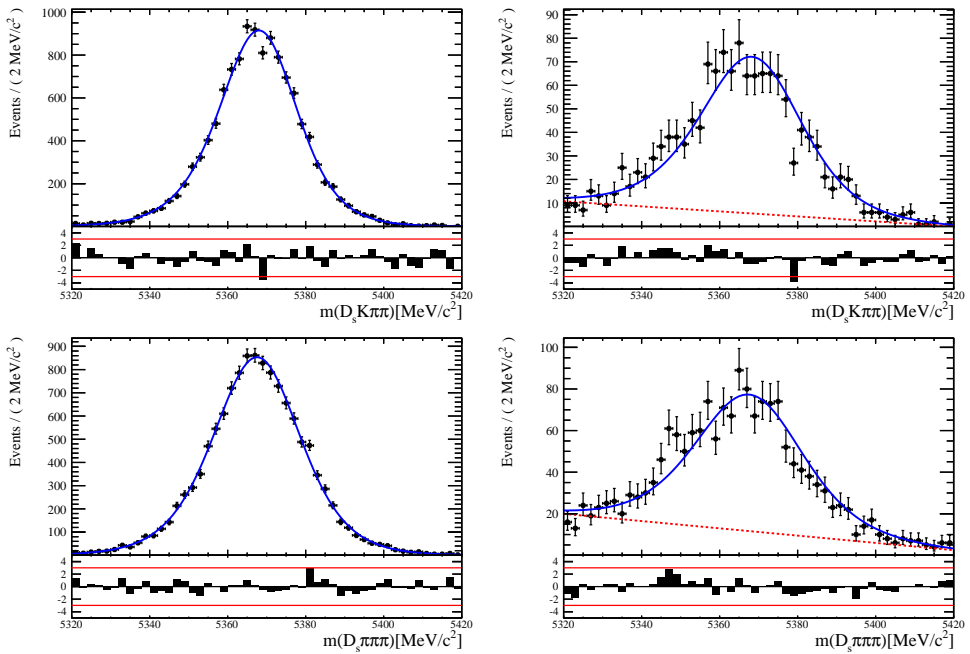


Figure 6.1: The reconstructed B_s mass distribution for simulated $B_s \rightarrow D_s K\pi\pi$ (top) and $B_s \rightarrow D_s \pi\pi\pi$ (bottom) decays classified with `BKGCAT` = 20 or 50 (left) and `BKGCAT` = 60 (right) after the full selection.

357 6.1.2 PID efficiencies

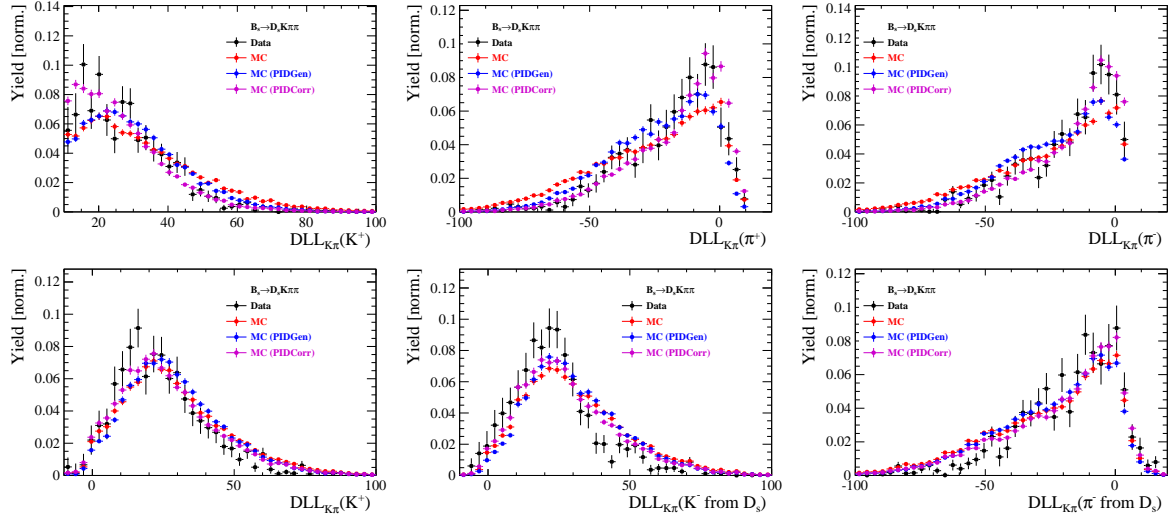


Figure 6.2

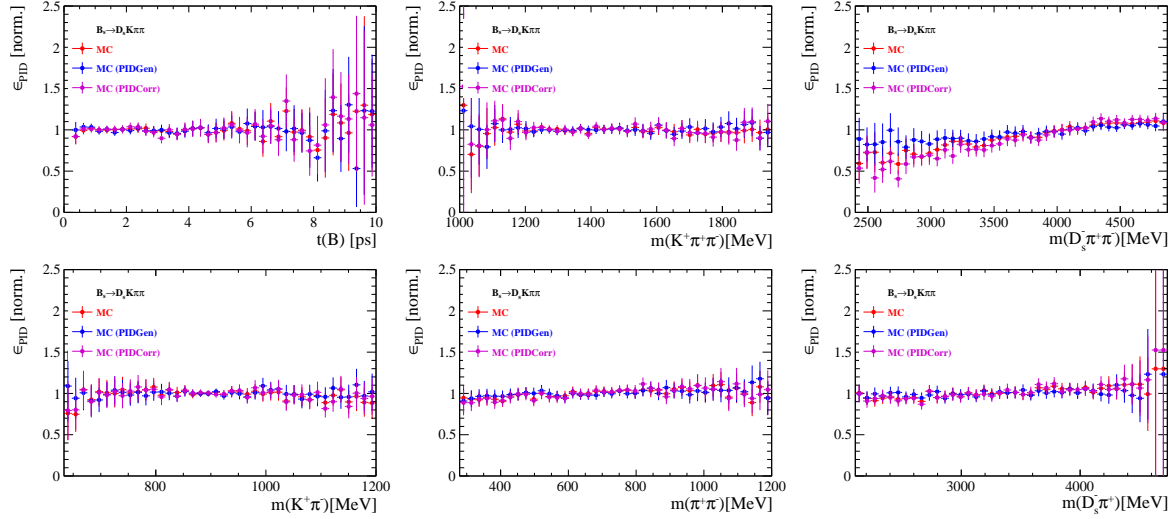


Figure 6.3

358 6.1.3 BDT efficiencies

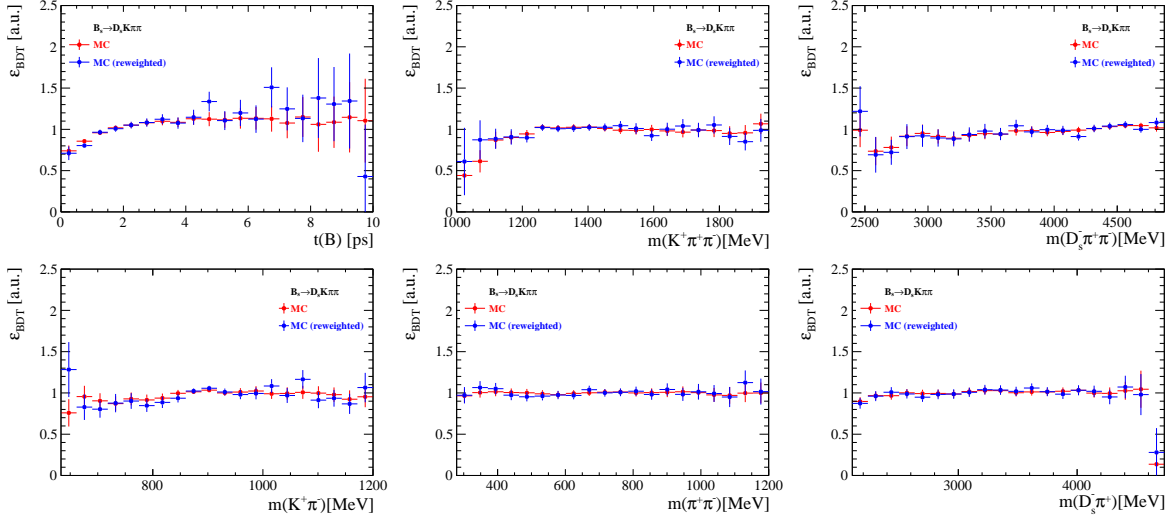


Figure 6.4

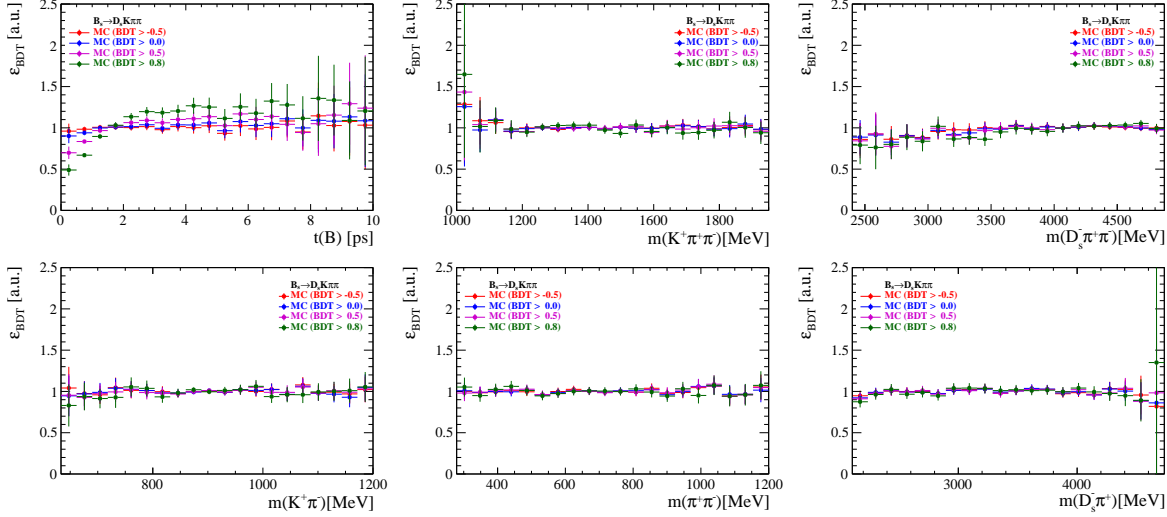


Figure 6.5

³⁵⁹ 6.1.4 Tracking efficiencies

360 **6.2 Decay-time acceptance**

361 The decay-time distribution of the B_s^0 mesons is sculpted due to the geometry of the LHCb
 362 detector and the applied selection cuts, which are described in Section 3. In particular,
 363 any requirement on the flight distance (FD), the impact parameter (IP) or the direction
 364 angle (DIRA) of the B_s^0 mesons, as well as the direct cut on the lifetime, will lead to a
 365 decay-time dependent efficiency $a(t)$. This efficiency will distort the theoretically expected,
 366 time-dependent decay rate

$$\frac{\Gamma(t)^{observed}}{dt} = \frac{\Gamma(t)^{theory}}{dt} \cdot a(t), \quad (6.1)$$

367 and has to be modelled correctly, in order to describe the observed decay rate. We
 368 use our control channel for this measurement, because for $B_s^0 \rightarrow D_s K\pi\pi$ decays the
 369 decay-time acceptance is correlated with the CP-observables which we aim to measure.
 370 Therefore, floating the CP-observables and the acceptance shape at the same time is
 371 not possible. Hence, a fit to the decay-time distribution of $B_s^0 \rightarrow D_s \pi\pi\pi$ candidates is
 372 performed and the obtained acceptance shape is corrected by the difference in shape found
 373 for the $B_s^0 \rightarrow D_s K\pi\pi$ and $B_s^0 \rightarrow D_s \pi\pi\pi$ MC.

374 A PDF of the form

$$\mathcal{P}(t', \vec{\lambda}) = \left[(e^{\Gamma_s t} \cdot \cosh(\frac{\Delta\Gamma_s t}{2}) \times \mathcal{R}(t - t')) \right] \cdot \epsilon(t', \vec{\lambda}), \quad (6.2)$$

375 is fit to the decay time distribution of $B_s^0 \rightarrow D_s \pi\pi\pi$ candidates in data. Since the
 376 fit is performed untagged, the PDF shown in Eq. 6.2 contains no terms proportional
 377 to Δm_s . The values for Γ_s and $\Delta\Gamma_s$ are fixed to the latest HFAG results [11]. The
 378 decay-time acceptance $\epsilon(t', \vec{\lambda})$ is modelled using the sum of cubic polynomials $v_i(t)$, so
 379 called Splines [12]. The polynomials are parametrised by so-called knots which determine
 380 their boundaries. Knots can be set across the fitted distribution to account for local
 381 changes in the acceptance shape. Using more knots is equivalent to using more base
 382 splines which are defined on a smaller sub-range. In total, $n + 2$ base splines $v_i(t)$ are
 383 needed to describe an acceptance shape which is parametrised using n knots.

384 For fits shown in the following, the knots have been placed at $t = [0.5, 1.0, 1.5, 2.0, 3.0, 9.5] ps$. To accommodate these 6 knot positions, 8 basic splines
 385 v_i , $i = [1, \dots, 8]$ are used. Since a rapid change of the decay time acceptance at low
 386 decay times due to the turn-on effect generated by the lifetime and other selection cuts is
 387 expected, more knots are placed in that regime. At higher decay times we expect linear
 388 behavior, with a possible small effect due to the VELO reconstruction. Therefore fewer
 389 knots are used. Furthermore, v_7 is fixed to 1 in order to normalize the overall acceptance
 390 function. To stabilise the last spline, v_8 is fixed by a linear extrapolation from the two
 392 previous splines:

$$v_N = v_{N-1} + \frac{v_{N-2} - v_{N-1}}{t_{N-2} - t_{N-1}} \cdot (t_N - t_{N-1}). \quad (6.3)$$

393 Here, $N = 8$ and t_{N-1} corresponds to the knot position associated with v_{N-1} .

394 6.2.1 Comparison of acceptance in subsamples

395 It is possible that the decay-time dependent efficiency deviates in different subsamples of
 396 our data. In particular, the acceptance could differentiate in subsamples with different
 397 final state kinematics, such as the run I & run II sample, the various D_s final states and
 398 the ways an event is triggered at the L0 stage. To investigate possible deviations, the
 399 full selected $B_s^0 \rightarrow D_s\pi\pi\pi$ sample is split into subsamples according to the categories
 400 mentioned above (run, D_s state, L0 trigger). For each subsample, the fit procedure
 401 described at the beginning of this chapter, using the pdf given by Eq. 6.2, is repeated
 402 and the obtained values for the spline coefficients v_i are compared. Figure 6.6 shows the
 403 comparison of the obtained spline coefficients for the different D_s final states.

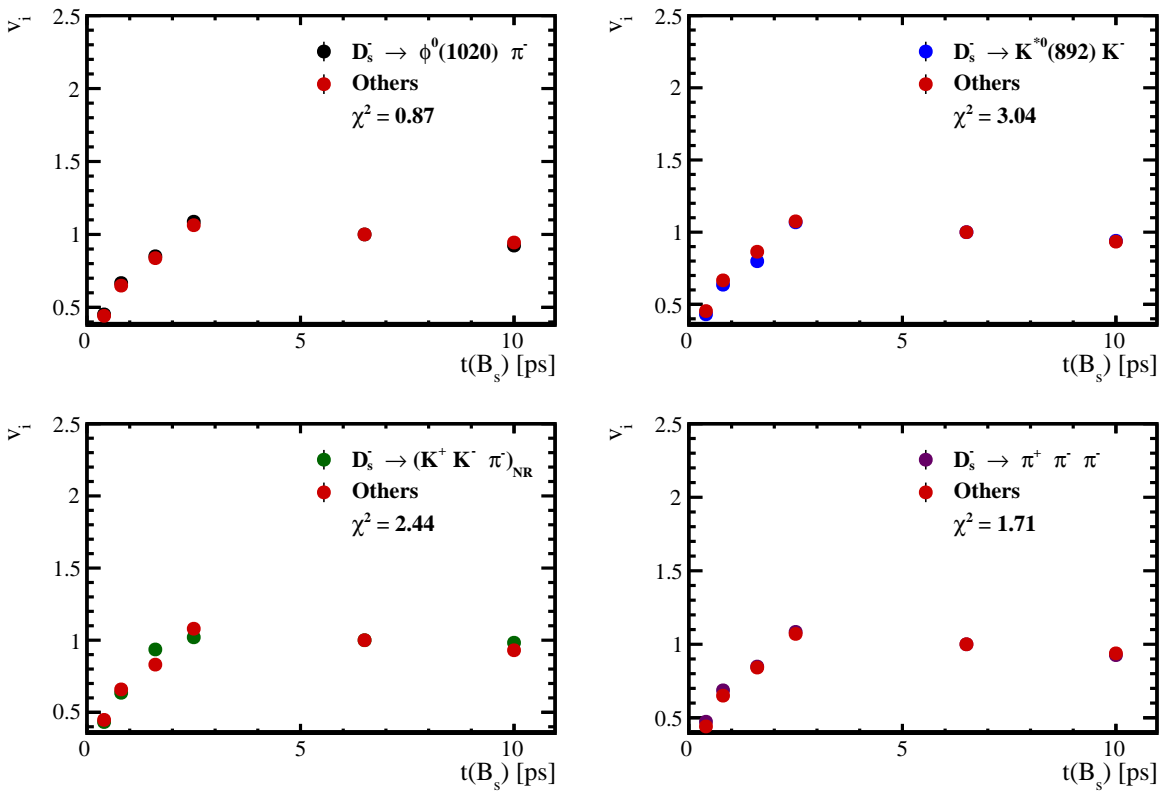


Figure 6.6: Comparison of the spline coefficients obtained from time-dependent fits to the $B_s^0 \rightarrow D_s\pi\pi\pi$ subsamples of different D_s final states. The comparison of one particular D_s state against all other states is shown.

404 Investigating the obtained spline coefficients from different D_s final states, good
 405 agreement is observed between all four channels and no need to distinguish between
 406 different final states in the time-dependent amplitude fit is found.

407 The comparison between spline coefficients for the different runs and L0 trigger categories
 408 is shown in Figure 6.7.

409 Significant deviations between spline coefficients obtained from the two different runs
 410 and L0 trigger categories can be observed. The deviations are most pronounced in the
 411 (0 – 5) ps region, where the majority of statistics is found. Therefore, the time-dependent
 412 efficiency has to be treated separately for the runs and L0 categories. This is achieved by

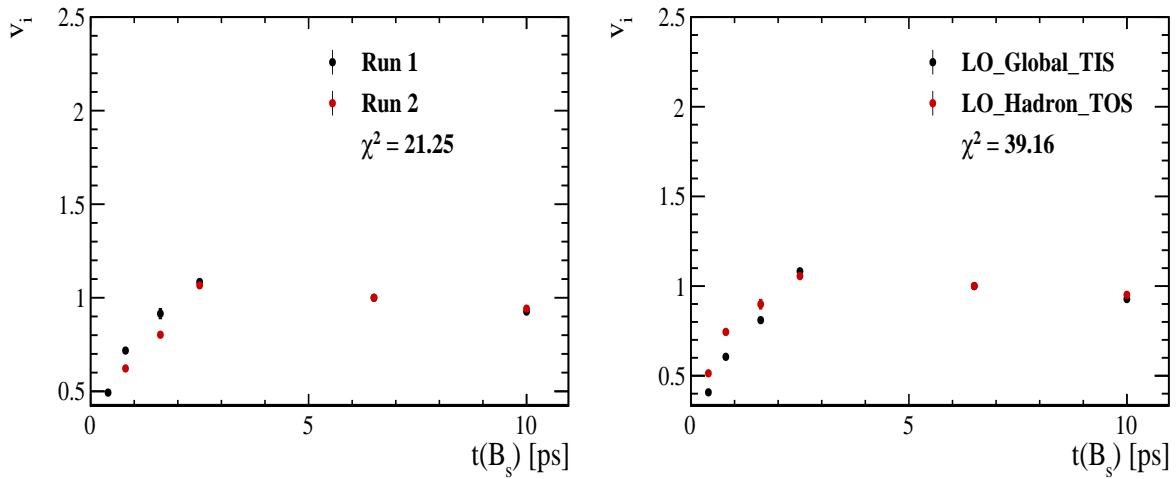


Figure 6.7: Comparison of the spline coefficients obtained from time-dependent fits to the $B_s^0 \rightarrow D_s\pi\pi\pi$ subsamples of (left) the different runs and (right) L0 trigger categories.

⁴¹³ implementing a simultaneous fit, where the acceptance description is allowed to vary in
⁴¹⁴ the subsamples.

⁴¹⁵ **6.2.2 Results**

⁴¹⁶ The nominal fit to $B_s^0 \rightarrow D_s\pi\pi\pi$ data using this configuration is shown in Figure ??.
⁴¹⁷ Note that the normalization of the splines in the following figures is not in scale. The fit
⁴¹⁸ parameters obtained from the described fits to data and simulation are summarised in
⁴¹⁹ Table 6.4.

Table 6.1: Time acceptance parameters for events in category [Run-I,L0-TOS].

Knot position	Coefficient	$B_s^0 \rightarrow D_s K\pi\pi$ data	$B_s^0 \rightarrow D_s K\pi\pi$ MC	Ratio
0.4	v_0	0.561 ± 0.038	0.546 ± 0.022	0.953 ± 0.060
0.8	v_1	0.826 ± 0.059	0.785 ± 0.034	0.910 ± 0.066
1.6	v_2	0.843 ± 0.087	0.905 ± 0.056	1.055 ± 0.095
2.5	v_3	1.154 ± 0.036	1.118 ± 0.028	0.930 ± 0.045
6.5	v_4	1.0 (fixed)	1.0 (fixed)	1.0 (fixed)
10.0	v_5	0.866 (interpolated)	0.897 (interpolated)	1.061 (interpolated)

Table 6.2: Time acceptance parameters for events in category [Run-I,L0-TIS].

Knot position	Coefficient	$B_s^0 \rightarrow D_s K\pi\pi$ data	$B_s^0 \rightarrow D_s K\pi\pi$ MC	Ratio
0.4	v_0	0.368 ± 0.031	0.412 ± 0.020	0.955 ± 0.077
0.8	v_1	0.583 ± 0.050	0.648 ± 0.033	0.910 ± 0.074
1.6	v_2	0.939 ± 0.101	0.953 ± 0.061	0.947 ± 0.096
2.5	v_3	1.052 ± 0.054	1.077 ± 0.035	1.003 ± 0.051
6.5	v_4	1.0 (fixed)	1.0 (fixed)	1.0 (fixed)
10.0	v_5	0.954 (interpolated)	0.932 (interpolated)	0.998 (interpolated)

Table 6.3: Time acceptance parameters for events in category [Run-II,L0-TOS].

Knot position	Coefficient	$B_s^0 \rightarrow D_s K\pi\pi$ data	$B_s^0 \rightarrow D_s K\pi\pi$ MC	Ratio
0.4	v_0	0.486 ± 0.009	0.482 ± 0.009	1.000 ± 0.000
0.8	v_1	0.691 ± 0.014	0.707 ± 0.015	1.000 ± 0.000
1.6	v_2	0.851 ± 0.024	0.926 ± 0.026	1.000 ± 0.000
2.5	v_3	1.061 ± 0.017	1.086 ± 0.018	1.000 ± 0.000
6.5	v_4	1.0 (fixed)	1.0 (fixed)	1.0 (fixed)
10.0	v_5	0.946 (interpolated)	0.925 (interpolated)	1.000 (interpolated)

Table 6.4: Time acceptance parameters for events in category [Run-II,L0-TIS].

Knot position	Coefficient	$B_s^0 \rightarrow D_s K\pi\pi$ data	$B_s^0 \rightarrow D_s K\pi\pi$ MC	Ratio
0.4	v_0	0.300 ± 0.007	0.482 ± 0.010	1.000 ± 0.000
0.8	v_1	0.476 ± 0.012	0.707 ± 0.016	1.000 ± 0.000
1.6	v_2	0.725 ± 0.023	0.926 ± 0.026	1.000 ± 0.000
2.5	v_3	1.064 ± 0.019	1.086 ± 0.018	1.000 ± 0.000
6.5	v_4	1.0 (fixed)	1.0 (fixed)	1.0 (fixed)
10.0	v_5	0.944 (interpolated)	0.925 (interpolated)	1.000 (interpolated)

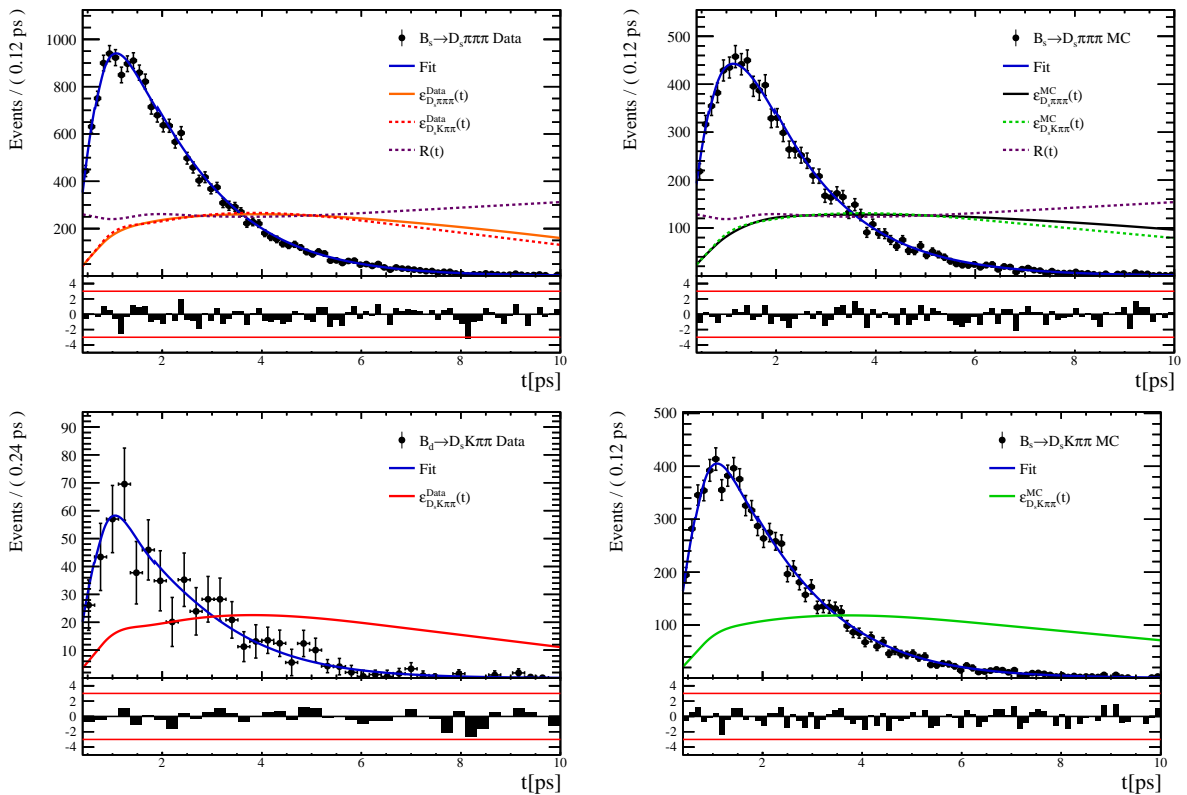


Figure 6.8

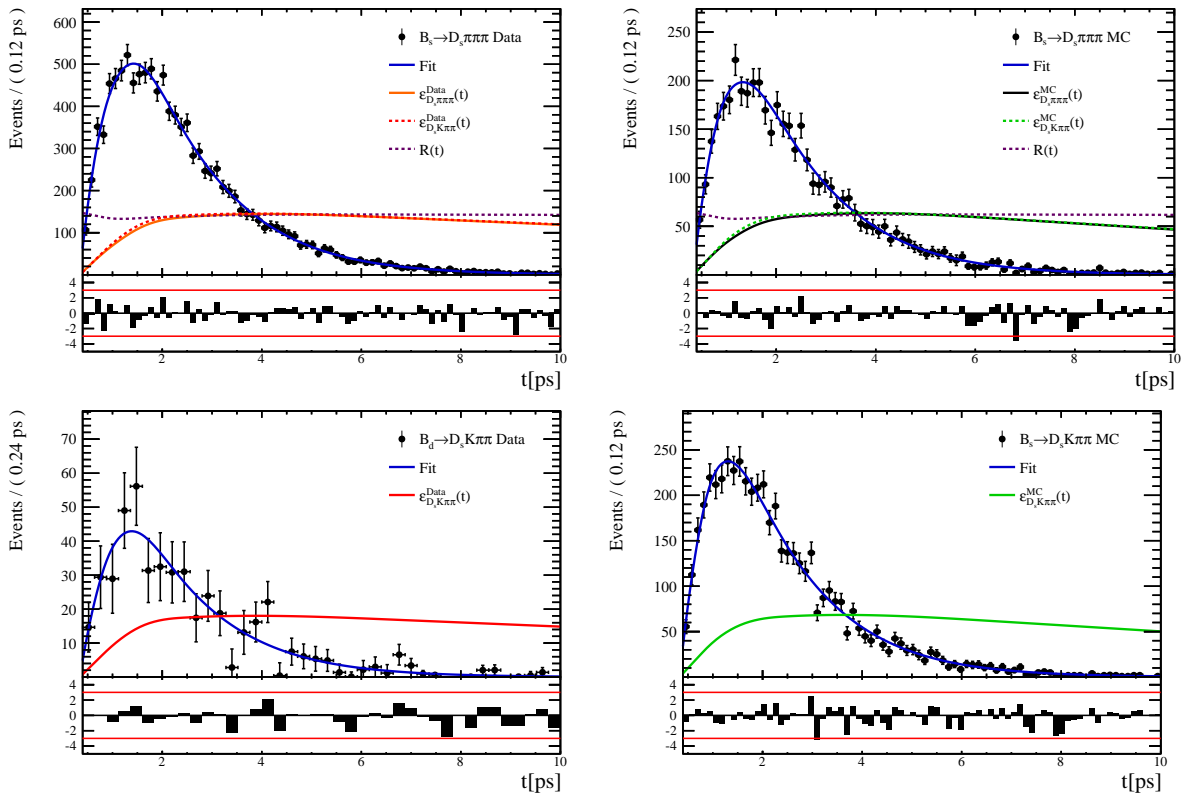


Figure 6.9:

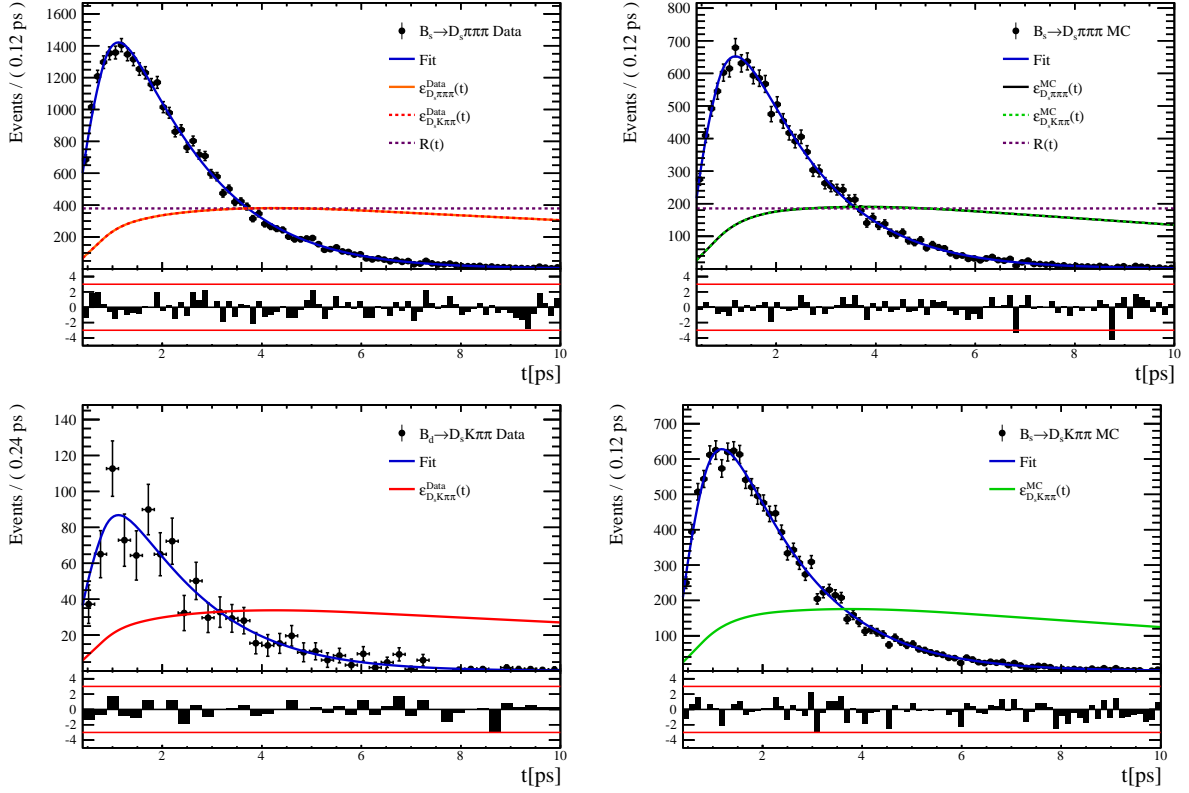


Figure 6.10

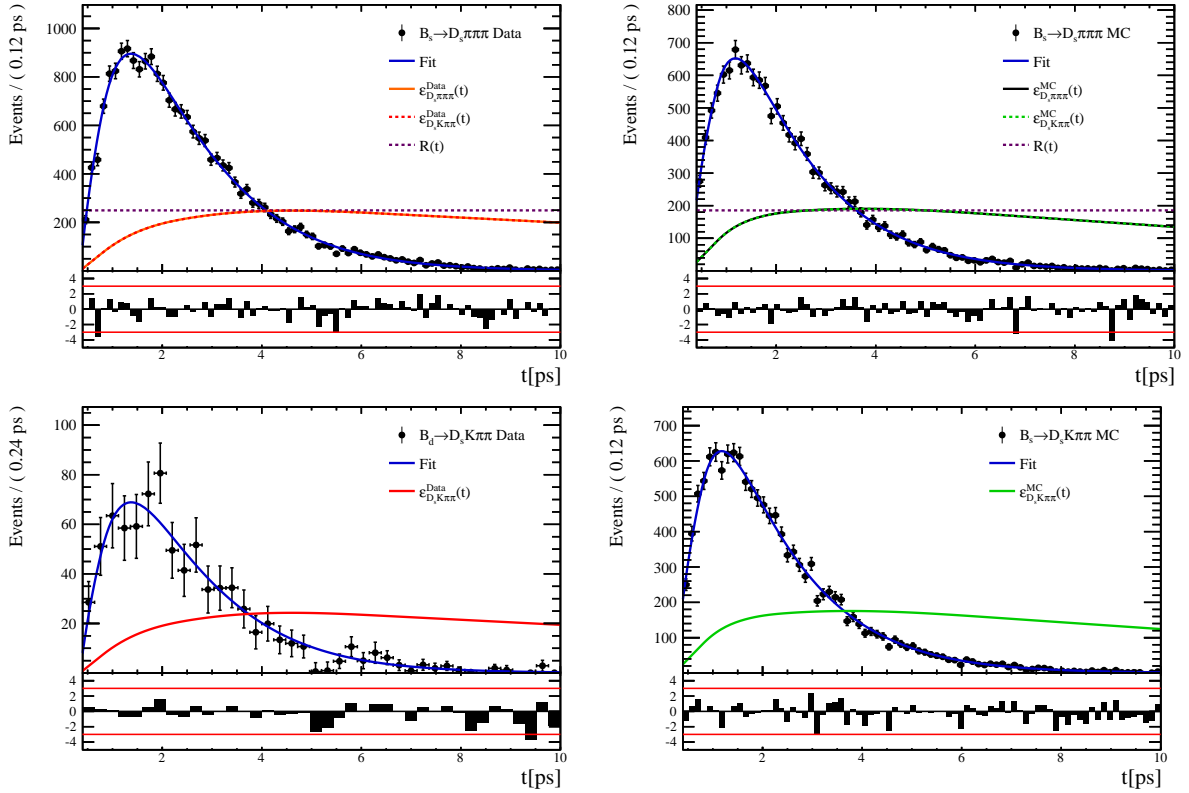


Figure 6.11:

420 **6.3 Phasespace acceptance**

421 7 Decay-time Resolution

422 The observed oscillation of B mesons is prone to dilution, if the detector resolution is
 423 of similar magnitude as the oscillation period. In the B_s^0 system, considering that the
 424 measured oscillation frequency of the B_s^0 [8] and the average LHCb detector resolution [13]
 425 are both $\mathcal{O}(50 \text{ fs}^{-1})$, this is the case. Therefore, it is crucial to correctly describe the
 426 decay time resolution in order to avoid a bias on the measurement of time dependent CP
 427 violation. Since the time resolution depends on the particular event, especially the decay
 428 time itself, the sensitivity on γ can be significantly improved by using an event dependent
 429 resolution model rather than an average resolution. For this purpose, we use the per-event
 430 decay time error that is estimated based on the uncertainty obtained from the global
 431 kinematic fit of the momenta and vertex positions (DTF) with additional constraints on
 432 the PV position and the D_s mass. In order to apply it correctly, it has to be calibrated.
 433 The raw decay time error distributions for $B_s^0 \rightarrow D_s\pi\pi\pi$ signal candidates are shown in
 434 Figure 7.1 for Run-I and Run-II data. Significant deviations between the two different
 435 data taking periods are observed due to the increase in center of mass energy from Run-I
 436 to Run-II, as well as (among others) new tunings in the pattern and vertex reconstruction.
 437 The decay time error calibration is consequently performed separately for both data taking
 438 periods.

439 For Run-I data, we use the calibration from the closely related $B_s^0 \rightarrow D_s K$ analysis
 440 which was performed on a data sample of prompt- D_s candidates combined with a random
 441 pion track from the PV. We verify the portability to our decay channel on MC.

442 For Run-II data, a new lifetime unbiased stripping line (LTUB) has been implemented
 443 which selects prompt- D_s candidates combined with random $K\pi\pi$ tracks from the PV.

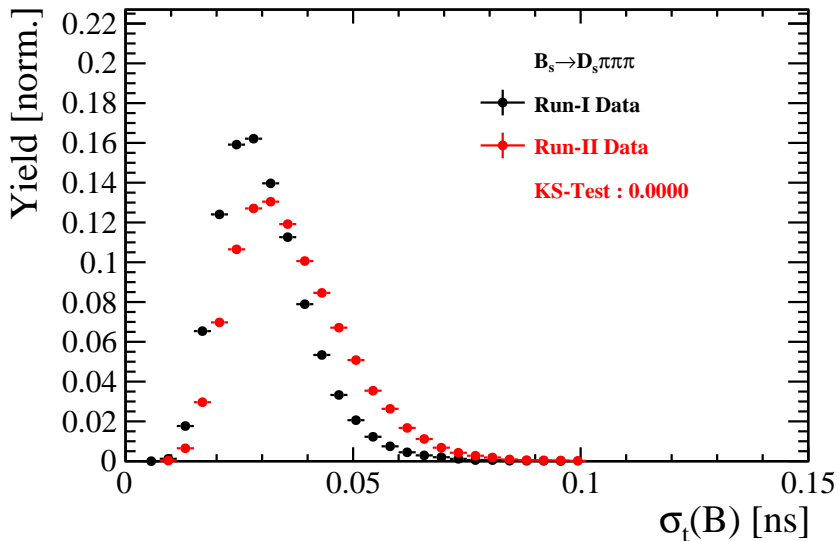


Figure 7.1: Distribution of the decay time error for $B_s^0 \rightarrow D_s\pi\pi\pi$ signal candidates for Run-I (black) and Run-II (red) data (sWeighted).

444 7.1 Calibration for Run-I data

445 For simulated $B_s^0 \rightarrow D_s K \pi\pi$ events, the spread of the differences between reconstructed
 446 decay time and true decay time, $\Delta t = t - t_{true}$, is a direct measure of the decay time
 447 resolution. The sum of two Gaussian pdfs with common mean but different widths is used
 448 to fit the distribution of the decay time difference Δt as shown in Fig. 7.2. The effective
 449 damping of the CP amplitudes due to the finite time resolution is described by the dilution
 450 \mathcal{D} . In the case of infinite precision, there would be no damping and therefore $\mathcal{D} = 1$ would
 451 hold, while for a resolution that is much larger than the B_s^0 oscillation frequency, \mathcal{D} would
 452 approach 0. For a double-Gaussian resolution model, the dilution is given by [14]

$$\mathcal{D} = f_1 e^{-\sigma_1^2 \Delta m_s^2 / 2} + (1 - f_1) e^{-\sigma_2^2 \Delta m_s^2 / 2}, \quad (7.1)$$

453 where σ_1 and σ_2 are the widths of the Gaussians, f_1 is the relative fraction of events
 454 described by the first Gaussian relative to the second and Δm_s is the oscillation frequency
 455 of B_s^0 mesons. An effective single Gaussian width is calculated from the dilution as,

$$\sigma_{eff} = \sqrt{(-2/\Delta m_s^2) \ln \mathcal{D}}, \quad (7.2)$$

456 which converts the resolution into a single-Gaussian function with an effective resolution
 457 that causes the same damping effect on the magnitude of the B_s oscillation. For the Run-I
 458 $B_s^0 \rightarrow D_s K \pi\pi$ MC sample the effective average resolution is found to be $\sigma_{eff} = 39.1 \pm 0.3$ fs.

459 To analyze the relation between the per-event decay time error δ_t and the actual
 460 resolution σ_t , the simulated $B_s^0 \rightarrow D_s K \pi\pi$ sample is divided into equal-statistics slices of
 461 δ_t . For each slice, the effective resolution is determined as described above. Details of the
 462 fit results in each slice are shown in appendix C. Figure 7.2 shows the obtained values
 463 for σ_{eff} as a function of the per-event decay time error σ_t . To account for the variable
 464 binning, the bin values are not placed at the bin center but at the weighted mean of the
 465 respective per-event-error bin. A linear function is used to parametrize the distribution.
 466 The obtained values are

$$\sigma_{eff}^{MC}(\sigma_t) = (0.0 \pm 0.0) \text{ fs} + (1.232 \pm 0.010) \sigma_t \quad (7.3)$$

467 where the offset is fixed to 0. For comparison, the calibration function found for $B_s^0 \rightarrow D_s K$
 468 MC is also shown in Figure 7.2 [14]:

$$\sigma_{eff}^{D_s K, MC}(\sigma_t) = (0.0 \pm 0.0) \text{ fs} + (1.201 \pm 0.013) \sigma_t. \quad (7.4)$$

469 Due to the good agreement between the scale factors for $B_s^0 \rightarrow D_s K$ and $B_s^0 \rightarrow D_s K \pi\pi$
 470 MC, we conclude that the resolution calibration for $B_s^0 \rightarrow D_s K$ data:

$$\sigma_{eff}^{D_s K}(\sigma_t) = (10.26 \pm 1.52) \text{ fs} + (1.280 \pm 0.042) \sigma_t \quad (7.5)$$

471 can be used for our analysis. The following calibration functions were used in the
 472 $B_s^0 \rightarrow D_s K$ analysis to estimate the systematic uncertainty on the decay-time resolution:

$$\sigma_{eff}^{D_s K}(\sigma_t) = (-0.568 \pm 1.570) \text{ fs} + (1.243 \pm 0.044) \sigma_t \quad (7.6)$$

$$\sigma_{eff}^{D_s K}(\sigma_t) = (0.0 \pm 0.0) \text{ fs} + (1.772 \pm 0.012) \sigma_t \quad (7.7)$$

474 The difference of the scale factors observed on $B_s^0 \rightarrow D_s K$ and $B_s^0 \rightarrow D_s K \pi\pi$ MC is
 475 assigned as additional systematic uncertainty.

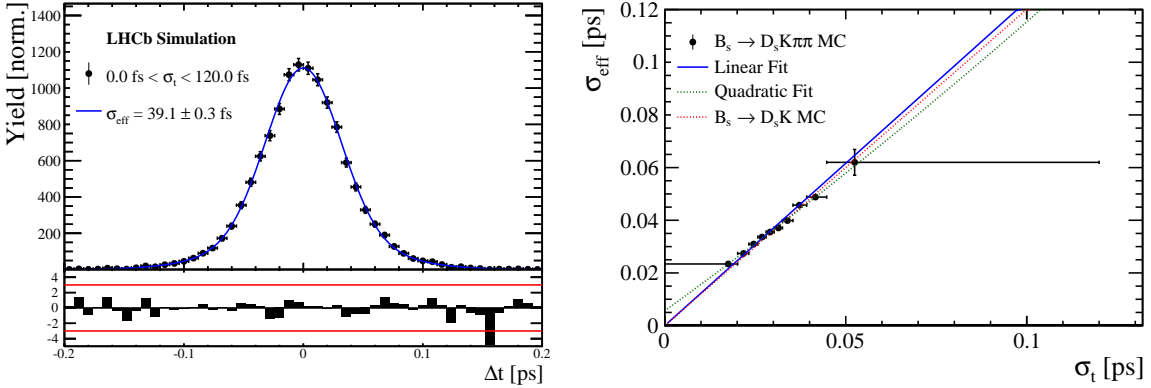


Figure 7.2: (Left) Difference of the true and measured decay time of $B_s^0 \rightarrow D_s K\pi\pi$ MC candidates. (Right) The measured resolution σ_{eff} as function of the per-event decay time error estimate σ_t for $B_s \rightarrow D_s K\pi\pi$ MC (Run-I). The fitted calibration curve is shown in blue.

476 7.2 Calibration for Run-II data

477 For the resolution calibration of Run-II data, a sample of promptly produced D_s candidates
 478 is selected using the `B02DsKPiPiLTUBD2HHHBeauty2CharmLine` stripping line. This
 479 lifetime-unbiased stripping line does not apply selection requirements related to lifetime
 480 or impact parameter, allowing for a study of the resolution. In order to reduce the rate
 481 of this sample it is pre-scaled in the stripping. Each D_s candidate is combined with a
 482 random kaon track and two random pion tracks which originate from the PV to obtain a
 483 sample of fake B_s candidates with a known true decay-time of $t_{\text{true}} = 0$. The difference of
 484 the measured decay time, t , of these candidates with respect to the true decay time is
 485 attributed to the decay time resolution.

486 The offline selection of the fake B_s candidates is summarized in Tab. 7.1. The selection
 487 is similar than the one for real data with the important difference that the D_s candidate
 488 is required to come from the PV by cutting on the impact parameter significance. Even
 489 after the full selection, a significant number of multiple candidates is observed. These
 490 are predominantly fake B_s candidates that share the same D_s candidate combined with
 491 different random tracks from the PV. We select one of these multiple candidates randomly
 492 which retains approximately 20% of the total candidates. The invariant mass distribution
 493 of the selected D_s candidates is shown in Fig. 7.3. To separate true D_s candidates from
 494 random combinations, the `sPlot` method is used to statistically subtract combinatorial
 495 background from the sample.

496 Figure 7.4 shows the `sWeighted` decay-time distribution for fake B_s candidates. Similar
 497 as in the previous section, the decay-time distribution is fitted with a double-Gaussian
 498 resolution model in slices of the per-event decay time error. Since some D_s candidates
 499 might actually originate from true B_s decays, the decay-time distribution of the fake B_s
 500 candidates might show a bias towards positive decay times. Therefore, we determine the
 501 decay-time resolution from the negative decay-time distribution only. Details of the fit
 502 results in each slice are shown in appendix C. The resulting calibration function:

$$\sigma_{\text{eff}}^{\text{Data}}(\sigma_t) = (9.7 \pm 1.7) \text{ fs} + (0.915 \pm 0.040) \sigma_t \quad (7.8)$$

is in good agreement with the one obtained for the $B_s \rightarrow J/\psi\phi$ (Run-II) analysis.

$$\sigma_{eff}^{J/\psi\phi}(\sigma_t) = (12.25 \pm 0.33) \text{ fs} + (0.8721 \pm 0.0080) \sigma_t \quad (7.9)$$

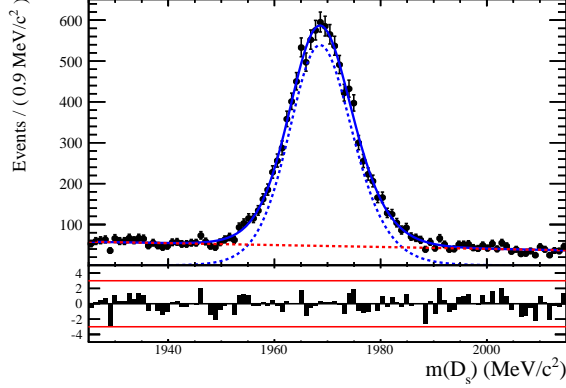


Figure 7.3: The invariant mass distribution for prompt D_s candidates.

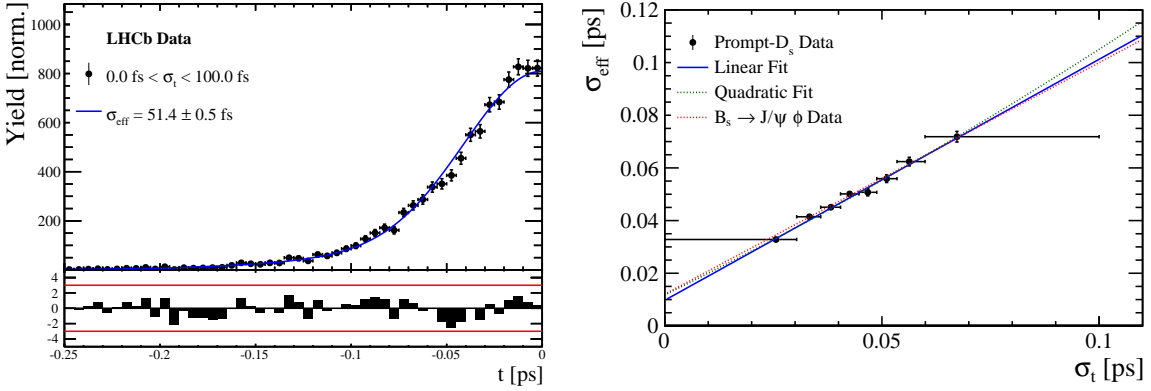


Figure 7.4: (Left) Decay-time distribution for fake B_s candidates from promptly produced D_s candidates, combined with random prompt $K\pi\pi$ bachelor tracks. (Right) The measured resolution σ_{eff} as function of the per-event decay time error estimate σ_t for fake B_s candidates (Run-II data). The fitted calibration curve is shown in blue.

Table 7.1: Offline selection requirements for fake B_s candidates from promptly produced D_s candidates combined with random prompt $K\pi\pi$ bachelor tracks.

	Description	Requirement
$B_s \rightarrow D_s K\pi\pi$	χ_{vtx}^2/ndof	< 8
	χ_{DTF}^2/ndof	< 15
	t	< 0 ps
$D_s \rightarrow hhh$	χ_{vtx}^2/ndof	< 5
	DIRA	> 0.99994
	χ_{FD}^2	> 9
	p_T	> 1800 MeV
	χ_{IP}^2	< 9
	$\chi_{IP}^2(h)$	> 5
	Wrong PV veto	$nPV = 1 \parallel \min(\Delta\chi_{IP}^2) > 20$
$D_s^- \rightarrow KK\pi^-$	D^0 veto	$m(KK) < 1840$ MeV
	D^- veto	$m(K^+K_\pi^-\pi^-) \neq m(D^-) \pm 30$ MeV
	Λ_c veto	$m(K^+K_\pi^-\pi^-) \neq m(\Lambda_c) \pm 30$ MeV
$D_s^- \rightarrow \phi\pi^-$	$m(KK)$	$= m_\phi \pm 20$ MeV
	PIDK(K^+)	> -10
	PIDK(K^-)	> -10
	PIDK(π^-)	< 20
$D_s^- \rightarrow K^*(892)K^-$	$m(KK)$	$\neq m_\phi \pm 20$ MeV
	$m(K^+\pi^-)$	$= m_{K^*(892)} \pm 75$ MeV
	PIDK(K^+)	> -10
	PIDK(K^-)	> -5
	PIDK(π^-)	< 20
$D_s^- \rightarrow (KK\pi^-)_{NR}$	$m(KK)$	$\neq m_\phi \pm 20$ MeV
	$m(K^+\pi^-)$	$\neq m_{K^*(892)} \pm 75$ MeV
	PIDK(K^+)	> 5
	PIDK(K^-)	> 5
	PIDK(π^-)	< 10
$D_s \rightarrow \pi\pi\pi$	PIDK(h)	< 10
	PIDp(h)	< 10
	D^0 veto	$m(\pi^+\pi^-) < 1700$ MeV
$X_s \rightarrow K\pi\pi$	$\chi_{IP}^2(h)$	< 40
	PIDK(K)	> 10
	PIDK(π)	< 5
	isMuon(h)	False
All tracks	p_T	> 500 MeV

504 **7.3 Cross-checks**

505 **7.3.1 Kinematic dependence**

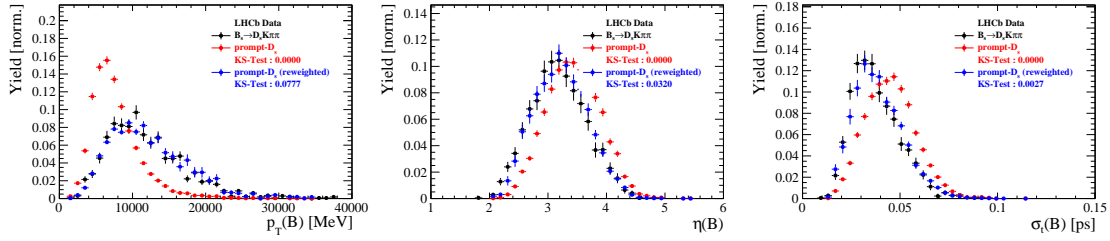


Figure 7.5

506 **7.3.2 DTF constraints**

507 8 B_s Production Asymmetry

Table 8.1: B_s production asymmetry for 2011 data.

p_T [GeV/c]	y	$A_P(B_s^0)_{\sqrt{s}=7 \text{ TeV}}$
(2.00, 7.00)	(2.10, 3.00)	$0.0166 \pm 0.0632 \pm 0.0125$
(2.00, 7.00)	(3.00, 3.30)	$0.0311 \pm 0.0773 \pm 0.0151$
(2.00, 7.00)	(3.30, 4.50)	$-0.0833 \pm 0.0558 \pm 0.0132$
(7.00, 9.50)	(2.10, 3.00)	$0.0364 \pm 0.0479 \pm 0.0068$
(7.00, 9.50)	(3.00, 3.30)	$0.0206 \pm 0.0682 \pm 0.0127$
(7.00, 9.50)	(3.30, 4.50)	$0.0058 \pm 0.0584 \pm 0.0089$
(9.50, 12.00)	(2.10, 3.00)	$-0.0039 \pm 0.0456 \pm 0.0121$
(9.50, 12.00)	(3.00, 3.30)	$0.1095 \pm 0.0723 \pm 0.0179$
(9.50, 12.00)	(3.30, 4.50)	$0.1539 \pm 0.0722 \pm 0.0212$
(12.00, 30.00)	(2.10, 3.00)	$-0.0271 \pm 0.0336 \pm 0.0061$
(12.00, 30.00)	(3.00, 3.30)	$-0.0542 \pm 0.0612 \pm 0.0106$
(12.00, 30.00)	(3.30, 4.50)	$-0.0586 \pm 0.0648 \pm 0.0150$

Table 8.2: B_s production asymmetry for 2012 data.

p_T [GeV/c]	y	$A_P(B_s^0)_{\sqrt{s}=8 \text{ TeV}}$
(2.00, 7.00)	(2.10, 3.00)	$0.0412 \pm 0.0416 \pm 0.0150$
(2.00, 7.00)	(3.00, 3.30)	$-0.0241 \pm 0.0574 \pm 0.0079$
(2.00, 7.00)	(3.30, 4.50)	$0.0166 \pm 0.0391 \pm 0.0092$
(7.00, 9.50)	(2.10, 3.00)	$0.0482 \pm 0.0320 \pm 0.0067$
(7.00, 9.50)	(3.00, 3.30)	$0.0983 \pm 0.0470 \pm 0.0155$
(7.00, 9.50)	(3.30, 4.50)	$-0.0430 \pm 0.0386 \pm 0.0079$
(9.50, 12.00)	(2.10, 3.00)	$0.0067 \pm 0.0303 \pm 0.0063$
(9.50, 12.00)	(3.00, 3.30)	$-0.1283 \pm 0.0503 \pm 0.0171$
(9.50, 12.00)	(3.30, 4.50)	$-0.0500 \pm 0.0460 \pm 0.0104$
(12.00, 30.00)	(2.10, 3.00)	$-0.0012 \pm 0.0222 \pm 0.0050$
(12.00, 30.00)	(3.00, 3.30)	$0.0421 \pm 0.0416 \pm 0.0162$
(12.00, 30.00)	(3.30, 4.50)	$0.0537 \pm 0.0447 \pm 0.0124$

508 9 K^- - π^+ Detection Asymmetry

509 The presented measurement of the CKM-angle γ using $B_s^0 \rightarrow D_s K \pi\pi$ decays is sensitive
 510 to a possible charge asymmetry of the kaon. This effect can be detector induced, because
 511 kaons are known to have a nuclear cross-section which is asymmetrically dependent on
 512 the sign of their charge. It is indispensable to determine the detector induced charge
 513 asymmetry of the kaon, as fitting without taking this effect into account would introduce
 514 a 'fake' CP violation.

515
 516 Instead of determining the single track detection asymmetry of a kaon, it is found [15]
 517 that the combined two track asymmetry of a kaon-pion pair is much easier to access.
 518 Therefore the two track asymmetry is used, which is defined as

$$A^{det}(K^-\pi^+) = \frac{\epsilon^{det}(K^-\pi^+) - \epsilon^{det}(K^+\pi^-)}{\epsilon^{det}(K^-\pi^+) + \epsilon^{det}(K^+\pi^-)}. \quad (9.1)$$

519 $A^{det}(K^-\pi^+)$ can further be expressed, assuming no CP violation in Cabibbo-favoured
 520 charm modes, as [16]

$$\begin{aligned} A^{det}(K^-\pi^+) &= \frac{N(D^+ \rightarrow K^-\pi^+\pi^+) - N(D^- \rightarrow K^+\pi^-\pi^-)}{N(D^+ \rightarrow K^-\pi^+\pi^+) + N(D^- \rightarrow K^+\pi^-\pi^-)} \\ &\quad - \frac{N(D^+ \rightarrow K_s^0\pi^+) - N(D^- \rightarrow K_s^0\pi^-)}{N(D^+ \rightarrow K_s^0\pi^+) + N(D^- \rightarrow K_s^0\pi^-)} \\ &\quad - A(K^0), \end{aligned} \quad (9.2)$$

521 where possible CP violation in the $D^+ \rightarrow K_s^0\pi^+$ mode is predicted to be smaller than
 522 10^{-4} in the Standard Model [17]. Using Eq. 9.2, the two track $K^-\pi^+$ asymmetry is
 523 obtained from the difference in asymmetries in the $D^+ \rightarrow K^-\pi^+\pi^+$ and $D^+ \rightarrow K_s^0\pi^+$
 524 modes. $A(K^0)$ is the asymmetry in the neutral kaon system and has to be taken into
 525 account as a correction.

526
 527 We use a dedicated LHCb tool to determine $A^{det}(K^-\pi^+)$ for all data taking periods
 528 used in this analysis. A detailed description, along with all plots can be found in [16].
 529 The tool provides large calibration samples of $D^\pm \rightarrow K^\pm\pi^\pm\pi^\pm$ and $D^\pm \rightarrow K_s^0\pi^\pm$ decays,
 530 which are used to determine the asymmetry following Eq. 9.2. Several weighting steps are
 531 performed to match the kinematics of the calibration samples to our signal decay sample:
 532 First, weights are assigned to the K^\pm and π^\pm of the $D^\pm \rightarrow K^\pm\pi^\pm\pi^\pm$ sample, using p, η
 533 of the K^\pm and p_T , η of the π^\pm from our $B_s^0 \rightarrow D_s K \pi\pi$ signal decay. Then, weights are
 534 assigned to the $D^\pm (p_T, \eta)$ and the $\pi^\pm (p_T)$ of the $D^\pm \rightarrow K_s^0\pi^\pm$ sample to match the cor-
 535 responding, weighted distributions of the $D^\pm \rightarrow K^\pm\pi^\pm\pi^\pm$ sample. In a last step, weights
 536 are assigned to match the bachelor pions ϕ distributions between the two calibration
 537 samples.

538 After the samples are correctly weighted, fits are performed to the invari-
 539 ant $m(K^-\pi^+\pi^+)/m(K^+\pi^-\pi^-)$ and $m(K_s^0\pi^+)/m(K_s^0\pi^-)$ distributions to determine
 540 $A^{det}(K^-\pi^+)$. The PDFs used to describe the invariant mass distributions consist of
 541 gaussian functions for the signal component and exponentials describing the residual
 542 background. The detection asymmetry is determined separately for every year and (since

543 it is a charge asymmetry effect) magnet polarity. Serving as an example for Run I
 544 and Run II, the fits used to determine $N(D^+ \rightarrow K^-\pi^+\pi^+)/N(D^- \rightarrow K^+\pi^-\pi^-)$ and
 545 $N(D^+ \rightarrow K_s^0\pi^+)/N(D^- \rightarrow K_s^0\pi^-)$ for 2011, magnet up data and 2015, magnet up data
 546 are shown in Figure 9.1 and 9.2 respectively.

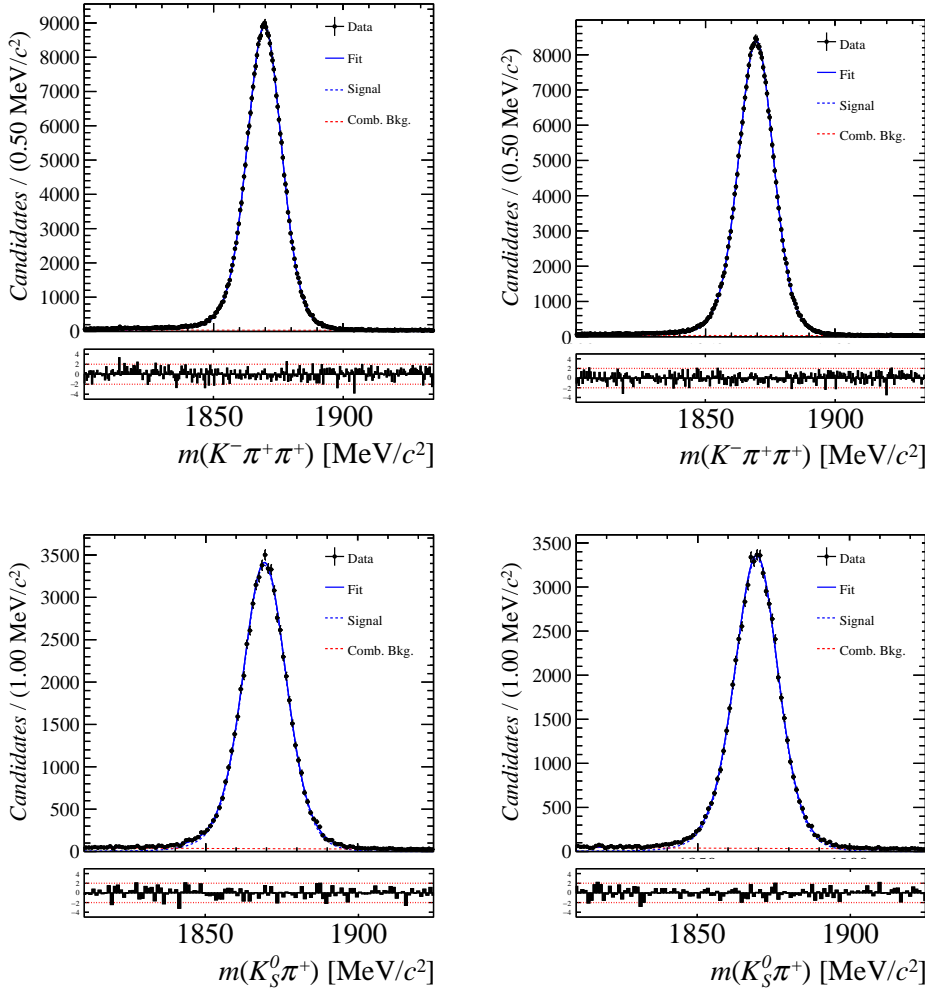


Figure 9.1: Distributions of the invariant mass of (top) $D^\pm \rightarrow K^\pm\pi^\pm\pi^\pm$ and (bottom) $D^\pm \rightarrow K_s^0\pi^\pm$ candidates for Run I data from the calibration samples. A fit described in the text is overlaid.

547 The obtained values of $A^{det}(K^-\pi^+) + A(K^0)$ for all years and polarities are shown in
 548 Table 9.1.

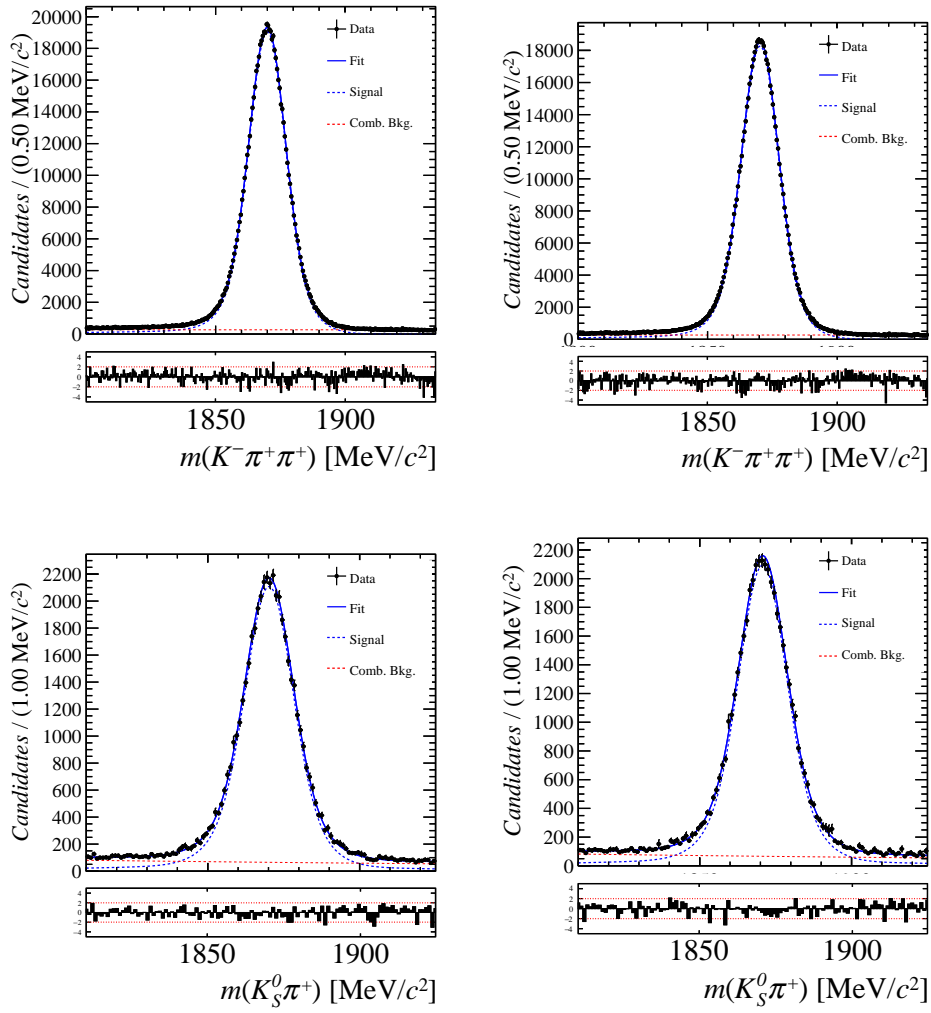


Figure 9.2: Distributions of the invariant mass of (top) $D^\pm \rightarrow K^\pm \pi^\pm \pi^\pm$ and (bottom) $D^\pm \rightarrow K_S^0 \pi^\pm$ candidates for Run 2 data from the calibration samples. A fit described in the text is overlaid.

Data sample	$A^{det}(K^-\pi^+) + A(K^0)$ [%]
Run I	
2011, mag. up	-2.01 \pm 0.32
2011, mag. down	-0.16 \pm 0.28
2011, average	-1.09 \pm 0.21
2012, mag. up	-0.90 \pm 0.20
2012, mag. down	-1.01 \pm 0.22
2012, average	-0.96 \pm 0.15
Run II	
2015, mag. up	-1.36 \pm 0.36
2015, mag. down	-0.96 \pm 0.24
2015, average	-1.16 \pm 0.22
2016, mag. up	0.50 \pm 0.88
2016, mag. down	1.23 \pm 0.72
2016, average	0.87 \pm 0.57

Table 9.1: Summary of the K^- - π^+ detection asymmetry obtained from the fits to the Run1 and Run2 calibration samples.

549 10 Time dependent fit

550 This section will cover the phasespace integrated, time dependent fit to $B_s^0 \rightarrow D_s h\pi\pi$ data,
 551 which is described by the PDF formulated in Eq. 2.6. For the phasespace integrated fit to
 552 $B_s^0 \rightarrow D_s K\pi\pi$ data, the sensitivity to the CKM phase γ will depend on the magnitude of
 553 the coherence factor κ , defined in Eq. 2.7, which is added as an additional fit parameter. In
 554 order to avoid any pollution of the final data samples by background events, both samples
 555 are weighted using the sWeights obtained by the fits to the invariant mass distributions,
 556 described in Sec. 4. This fit approach is commonly known as *sFit*. As additional input to
 557 the fit, the tagging information (Sec. 5), as well as the decay time acceptance (Sec. 6)
 558 and resolution (Sec. 7) is used and fixed to the values obtained by the dedicated studies.
 559 Taking all inputs into account, the final time dependent fit PDF is given by

$$\mathcal{P}\mathcal{D}\mathcal{F}(t, \vec{\lambda}) = \left(\epsilon(t) \cdot \int P(x, t, q_t, q_f) dx \right) \times \mathcal{R}(t - t'), \quad (10.1)$$

560 where $\int P(x, t, q_t, q_f) dx$ is the PDF given by Eq. 2.6, $\epsilon(t)$ is the efficiency due to the
 561 time acceptance effects and $\mathcal{R}(t - t')$ is the Gaussian time resolution function.

562 10.1 sFit to $B_s^0 \rightarrow D_s \pi\pi\pi$ data

563 The phasespace-integrated, time-dependent fit is performed to the full sWeighted sample
 564 of selected candidates from Run I and 2015+2016 Run II data, containing both possible
 565 magnet polarities and D_s final states. In the fit, the values of Γ_s and $\Delta\Gamma_s$ are fixed to the
 566 latest PDG report. All tagging parameters are fixed to the central values found in the
 567 tagging calibration, described in Sec. 5. Due to the fact that the $B_s^0 \rightarrow D_s \pi\pi\pi$ decay is
 568 flavour specific, the CP-coefficients can be fixed to $C = 1$ and $D_f = D_{\bar{f}} = S_f = S_{\bar{f}} = 0$,
 569 reducing Eq. 2.6 to

$$\int P(x, t, q_t, q_f) dx = [\cosh\left(\frac{\Delta\Gamma t}{2}\right) + q_t q_f \cos(\Delta m_s t)] e^{-\Gamma t}. \quad (10.2)$$

570 Note that in this case, the dependence on the coherence factor κ is dropped and the
 571 same relation as found for $B_s^0 \rightarrow D_s \pi$ decays is recovered. Therefore, the only free fit
 572 parameter left is Δm_s . The data distribution with the overlaid fit is shown in Fig. xXx
 573 and the obtained value for the mixing frequency is

$$\Delta m_s = xx.xxx \pm 0.yyy. \quad (10.3)$$

574 10.2 sFit to $B_s^0 \rightarrow D_s K\pi\pi$ data

575 10.3 Results

A Details of multivariate classifier

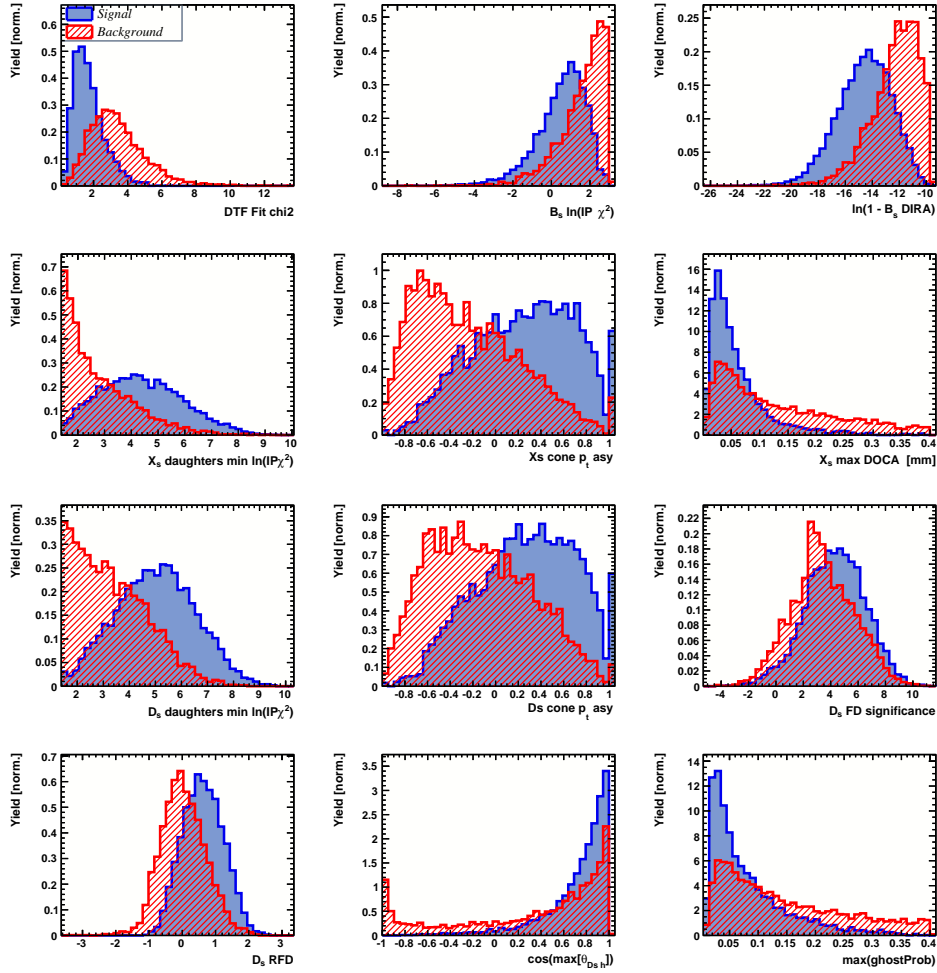


Figure 1.1: Variables used to train the BDTG.

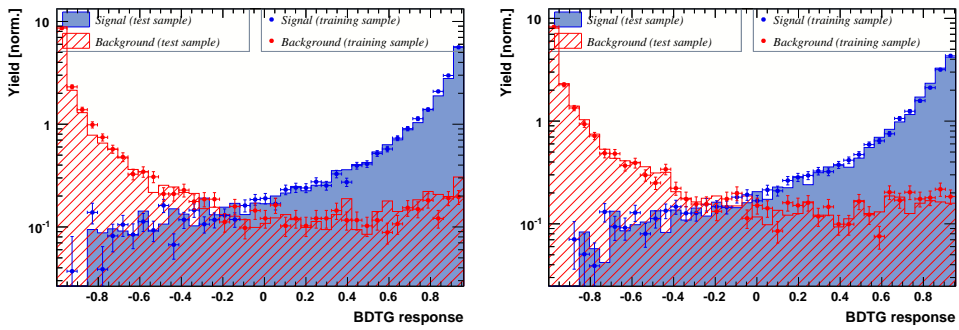


Figure 1.2: Response of the classifier trained on the even (left) and odd (right) sample.

577 B Detailed mass fits

578 In this section, all fits to the mass distribution of $B_s^0 \rightarrow D_s\pi\pi\pi$ and $B_s^0 \rightarrow D_sK\pi\pi$
 579 candidates are shown. The fits are performed simultaneously in run period (Run-I, Run-
 580 II), D_s final state ($D_s \rightarrow KK\pi$ non-resonant, $D_s \rightarrow \phi\pi$, $D_s \rightarrow K^*K$, or $D_s \rightarrow \pi\pi\pi$) and
 581 L0 trigger category.

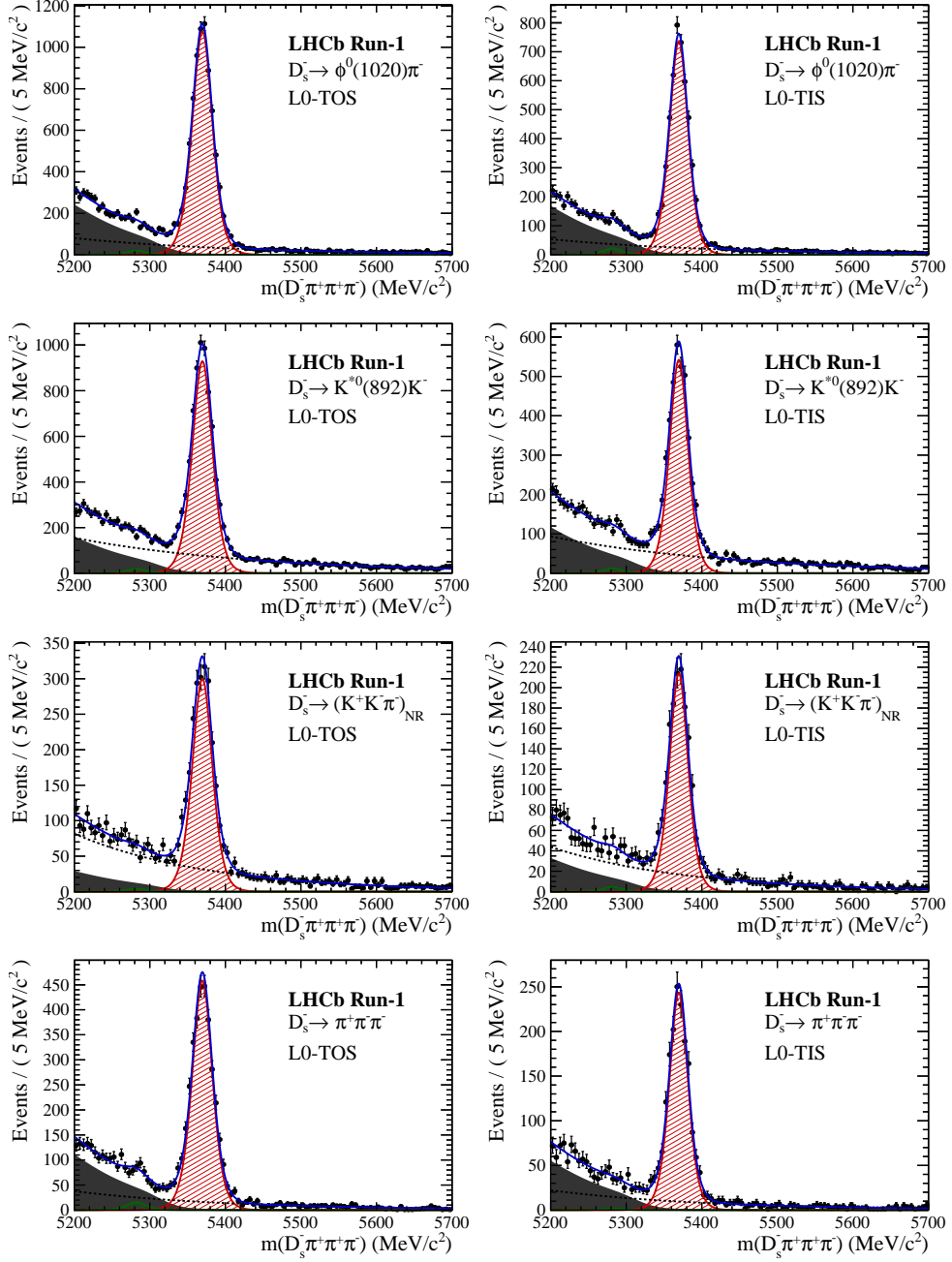


Figure 2.1: Invariant mass distributions of $B_s^0 \rightarrow D_s\pi\pi\pi$ candidates for Run-I data.

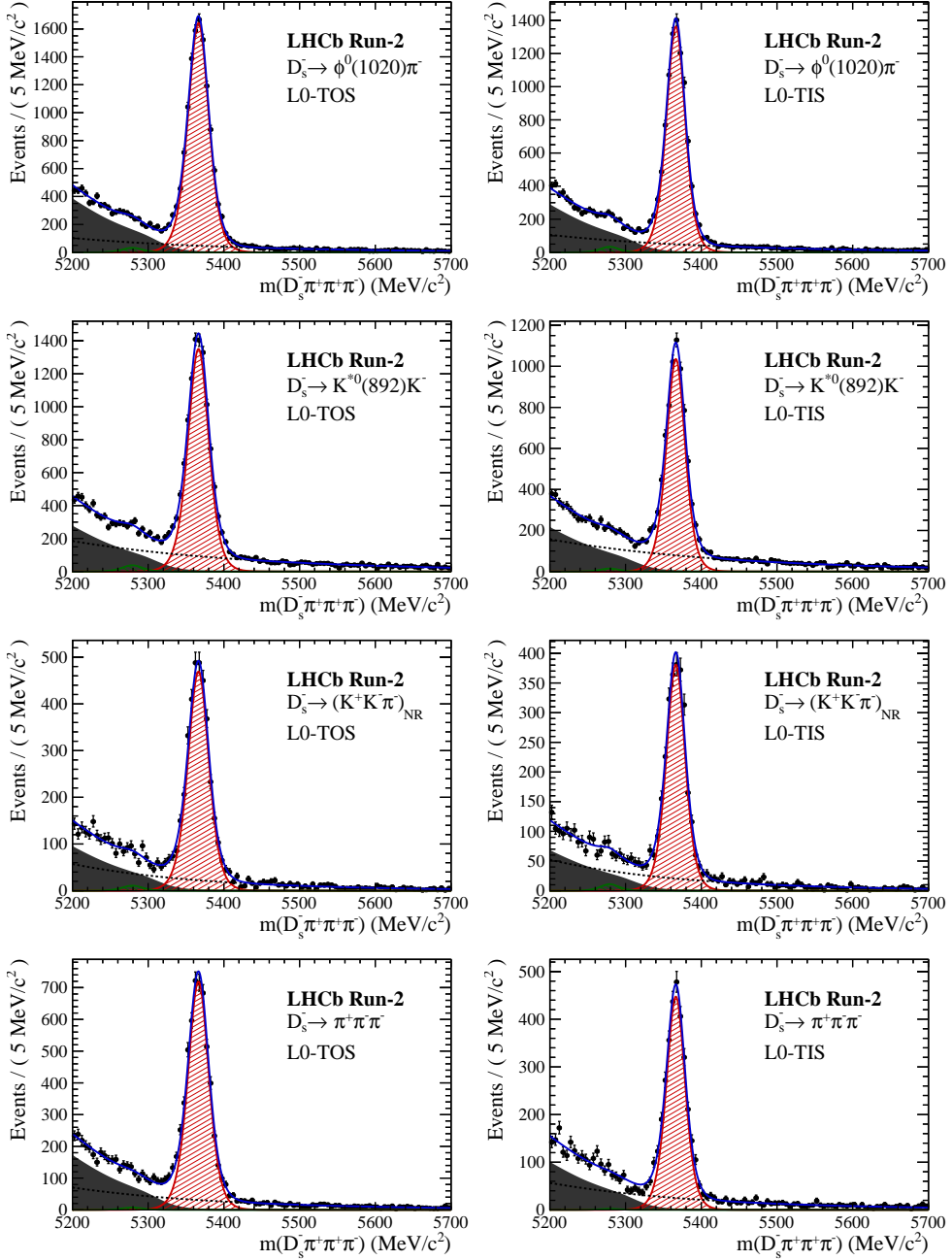


Figure 2.2: Invariant mass distributions of $B_s^0 \rightarrow D_s\pi\pi\pi$ candidates for Run-II data.

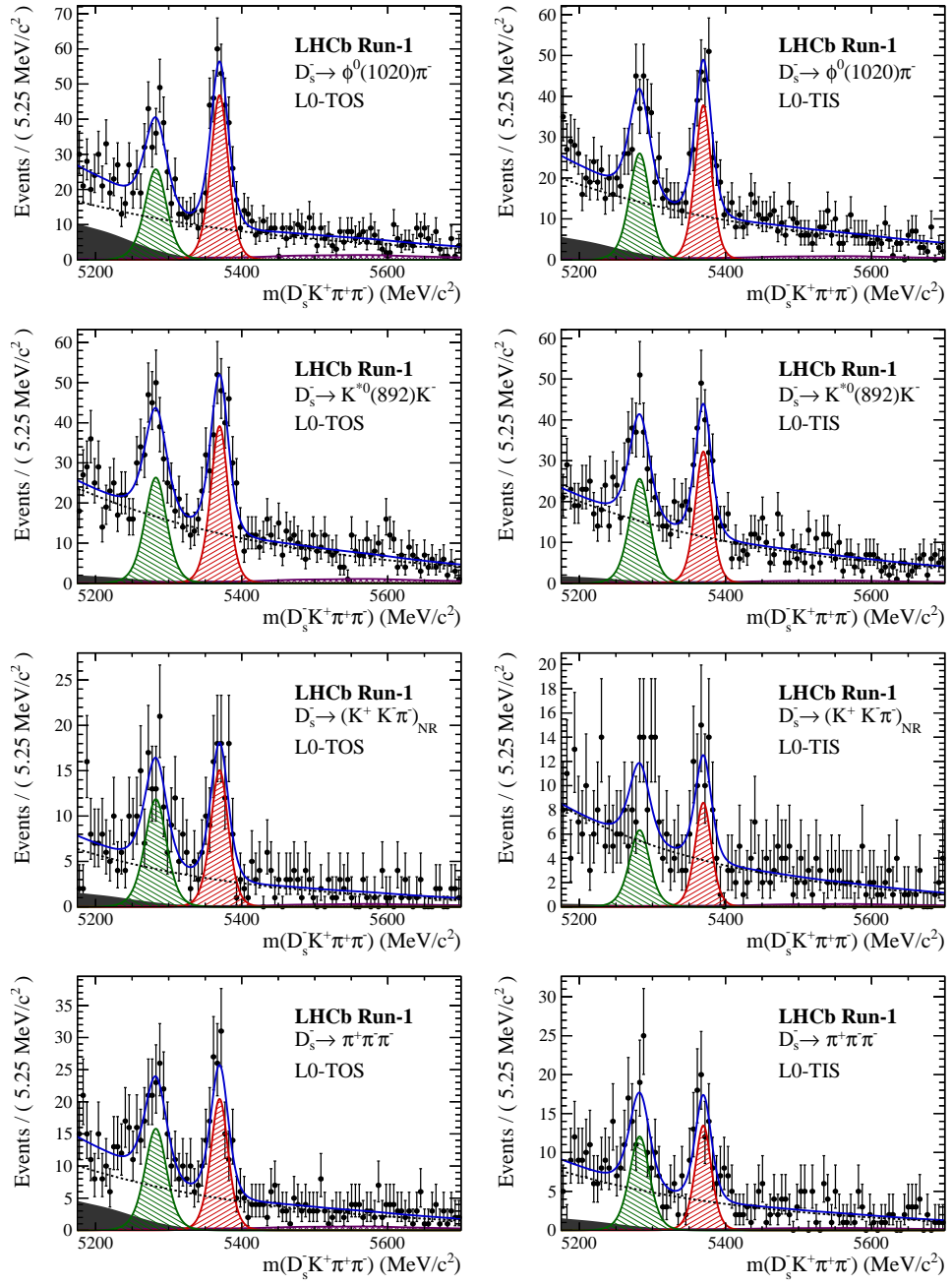


Figure 2.3: Invariant mass distributions of $B_s^0 \rightarrow D_s K \pi\pi$ candidates for Run-I data.

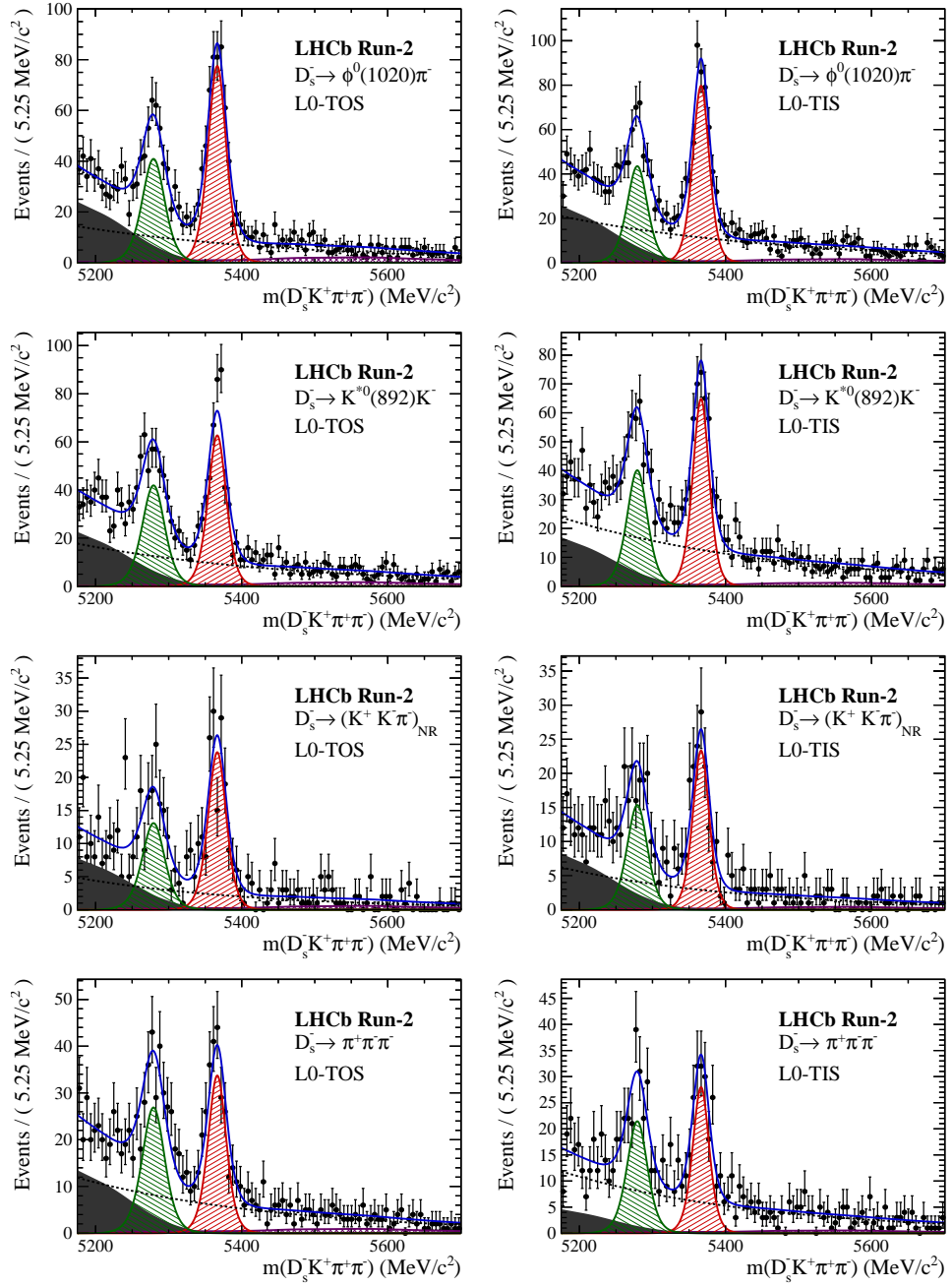


Figure 2.4: Invariant mass distributions of $B_s^0 \rightarrow D_s K \pi\pi$ candidates for Run-II data.

582 C Decay-time Resolution fits

583 This section contains all fits to the distributions of the decay time difference Δt between
 584 the true and the reconstructed decay time of the truth-matched B_s^0 candidates on MC.
 585 The fits are performed in bins of the decay time error σ_t , where an adaptive binning
 586 scheme is used to ensure that approximately the same number of events are found in each
 587 bin.

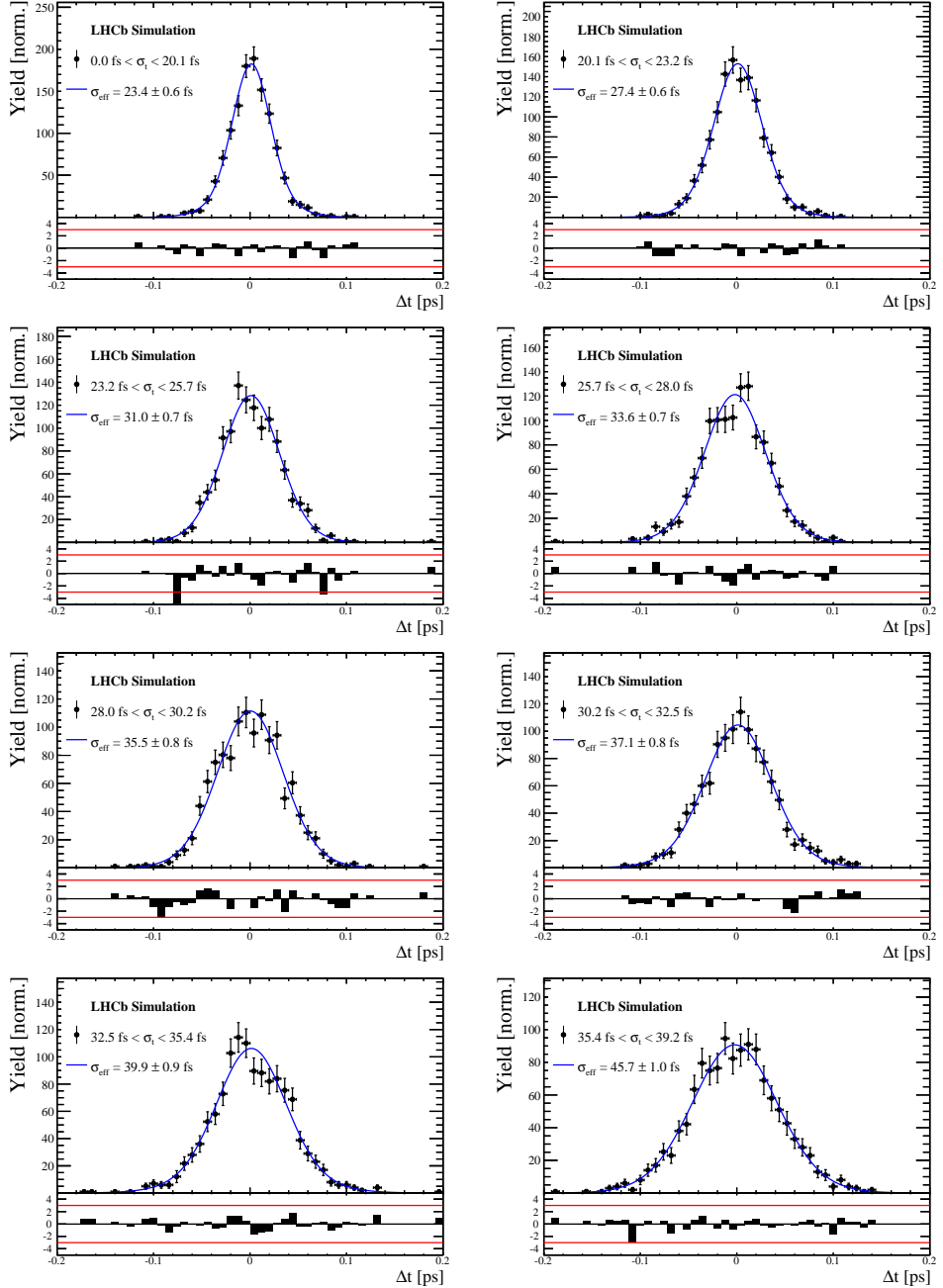


Figure 3.1: Difference of the true and measured decay time of $B_s^0 \rightarrow D_s K \pi\pi$ MC candidates in bins of the per-event decay time error estimate..

σ_t Bin [fs]	σ_1 [fs]	σ_2 [fs]	f_1	D	σ_{eff} [fs]
0.0 - 20.1	19 ± 0.675	33.8 ± 1.77	0.75 ± 0	0.917 ± 0.00406	23.4 ± 0.599
20.1 - 23.2	23.4 ± 0.86	37.4 ± 1.95	0.75 ± 0	0.888 ± 0.00477	27.4 ± 0.621
23.2 - 25.7	28.1 ± 1.02	38.7 ± 2.32	0.75 ± 0	0.86 ± 0.00563	31 ± 0.671
25.7 - 28.0	30.1 ± 1.12	43.2 ± 2.56	0.75 ± 0	0.837 ± 0.00651	33.6 ± 0.734
28.0 - 30.2	32.4 ± 1.12	44.2 ± 2.59	0.75 ± 0	0.819 ± 0.00694	35.5 ± 0.756
30.2 - 32.5	32.6 ± 1.38	49.2 ± 3.04	0.75 ± 0	0.805 ± 0.00792	37.1 ± 0.841
32.5 - 35.4	34.4 ± 1.19	54.7 ± 2.85	0.75 ± 0	0.778 ± 0.0086	39.9 ± 0.879
35.4 - 39.2	41.9 ± 1.8	56.9 ± 4.18	0.75 ± 0	0.719 ± 0.00997	45.7 ± 0.962
39.2 - 44.7	42.2 ± 1.56	68.1 ± 4.01	0.75 ± 0	0.687 ± 0.0114	48.8 ± 1.08
44.7 - 120.0	55.5 ± 2.59	83 ± 14.7	0.75 ± 0	0.546 ± 0.0521	62 ± 4.89

Table 3.1: Measured time resolution for $B_s \rightarrow D_s K\pi\pi$ MC in bins of the per-event decay time error estimate.

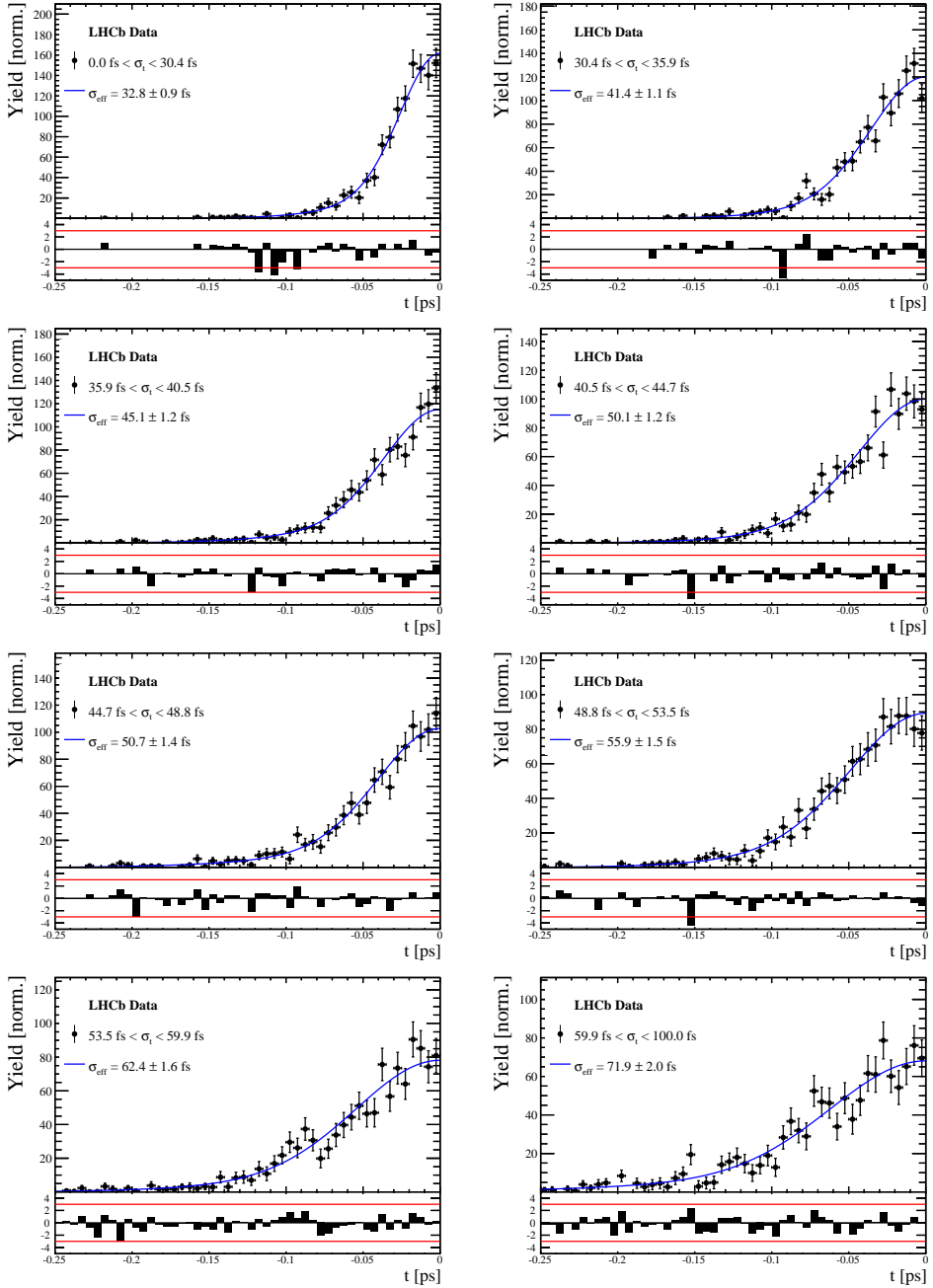


Figure 3.2: Decay-time distribution for fake B_s candidates from promptly produced D_s candidates, combined with random prompt $K\pi\pi$ bachelor tracks, for bins in the per-event decay time error estimate.

σ_t Bin [fs]	σ_1 [fs]	σ_2 [fs]	f_1	D	σ_{eff} [fs]
0.0 - 30.4	25.4 ± 1.03	50.7 ± 2.77	0.75 ± 0	0.844 ± 0.00822	32.8 ± 0.942
30.4 - 35.9	34.5 ± 1.46	60.2 ± 3.48	0.75 ± 0	0.763 ± 0.0108	41.4 ± 1.08
35.9 - 40.5	35.6 ± 1.35	71.3 ± 3.84	0.75 ± 0	0.726 ± 0.0121	45.1 ± 1.18
40.5 - 44.7	42.3 ± 1.65	73.3 ± 4.21	0.75 ± 0	0.673 ± 0.0132	50.1 ± 1.24
44.7 - 48.8	39.6 ± 1.64	84.8 ± 5.07	0.75 ± 0	0.666 ± 0.0145	50.7 ± 1.36
48.8 - 53.5	47.6 ± 1.94	82.4 ± 5.48	0.75 ± 0	0.611 ± 0.0157	55.9 ± 1.46
53.5 - 59.9	53 ± 2.15	95.3 ± 6.84	0.75 ± 0	0.541 ± 0.0174	62.4 ± 1.63
59.9 - 100.0	60.5 ± 2.8	125 ± 14	0.75 ± 0	0.443 ± 0.0204	71.9 ± 2.03

Table 3.2: Measured time resolution for prompt- D_s data in bins of the per-event decay time error estimate.

588 D MC corrections

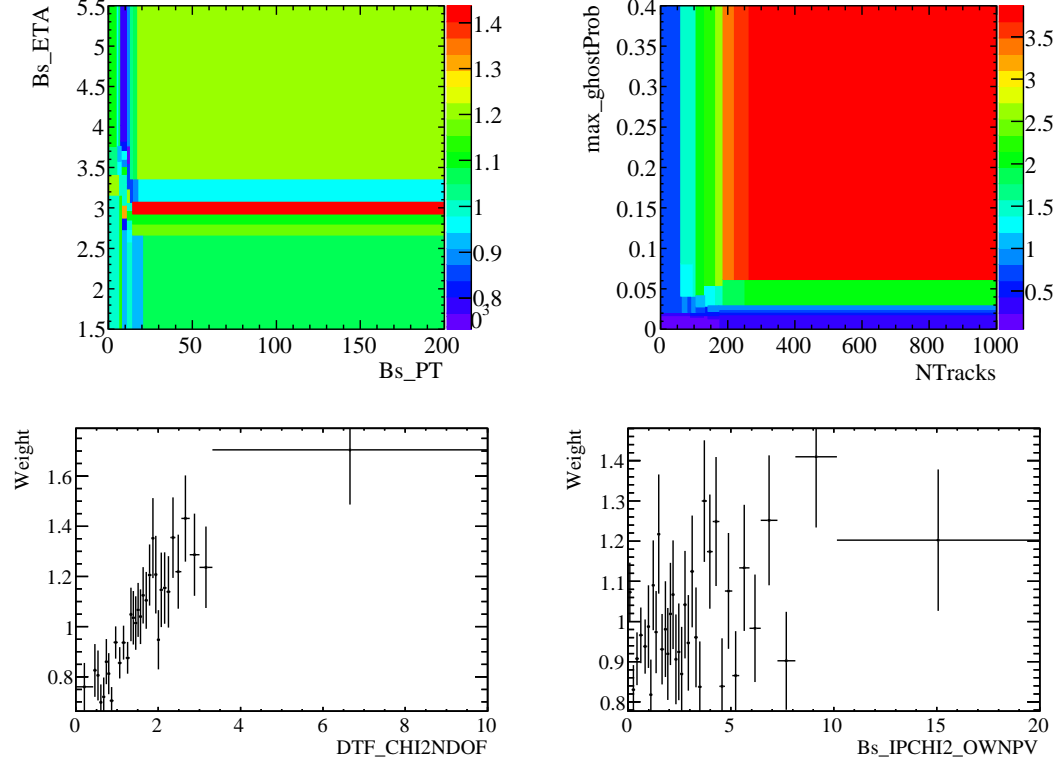


Figure 4.1: Weights applied to correct for Data/MC differences.

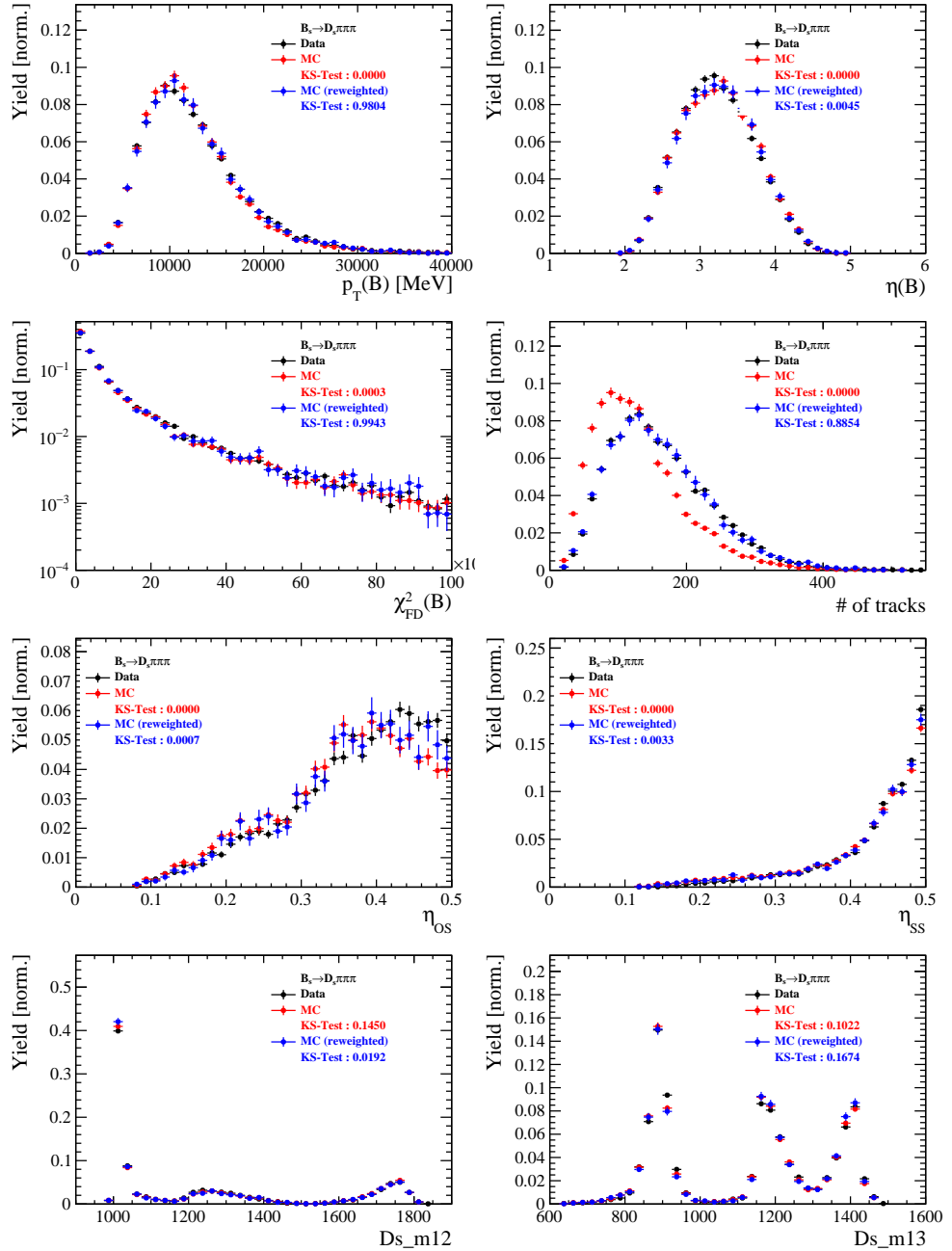


Figure 4.2: Comparison of selected variables for $B_s \rightarrow D_s \pi\pi\pi$ decays.

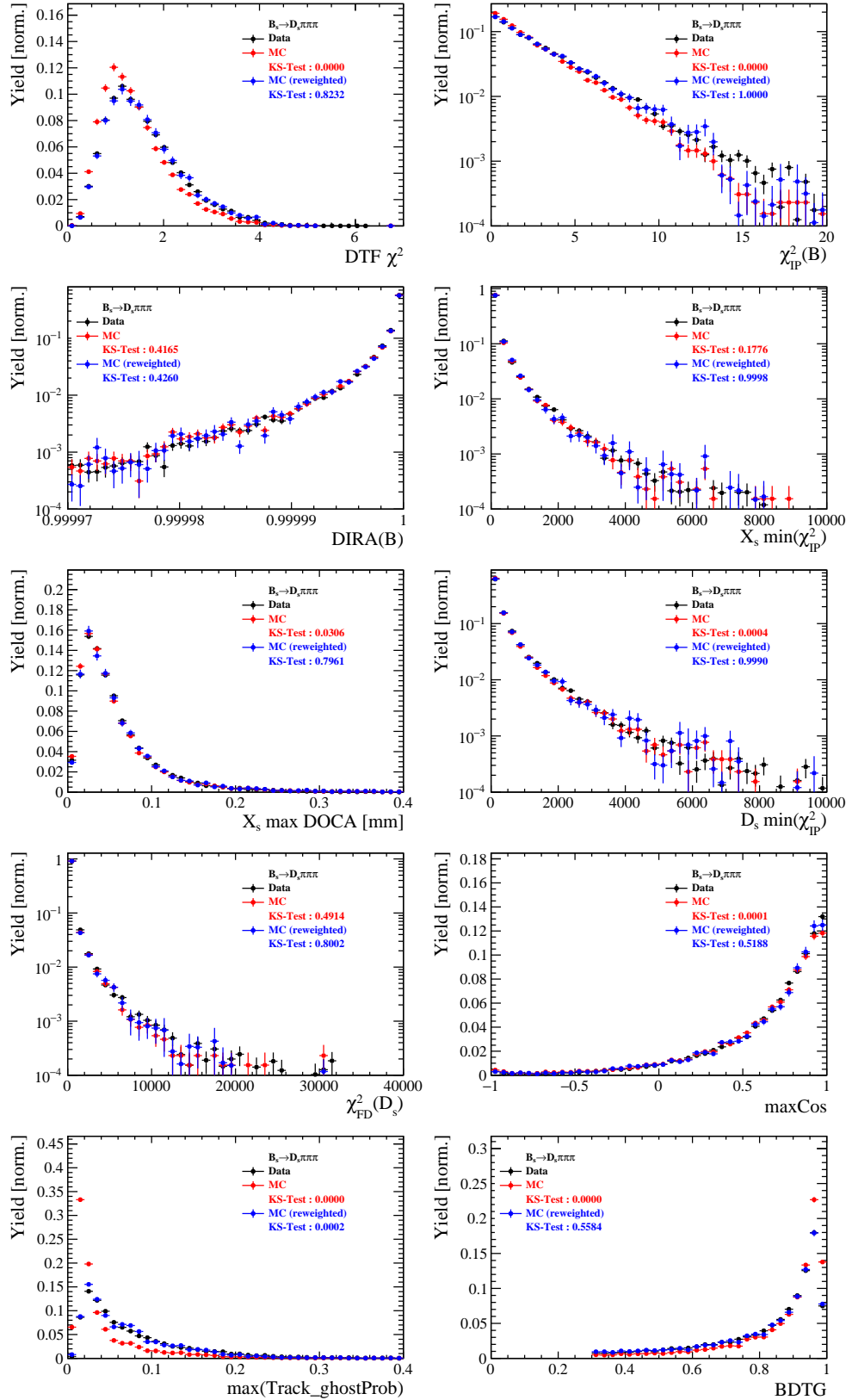


Figure 4.3: Comparison of BDTG input variables and classifier response for $B_s \rightarrow D_s \pi\pi\pi$ decays.

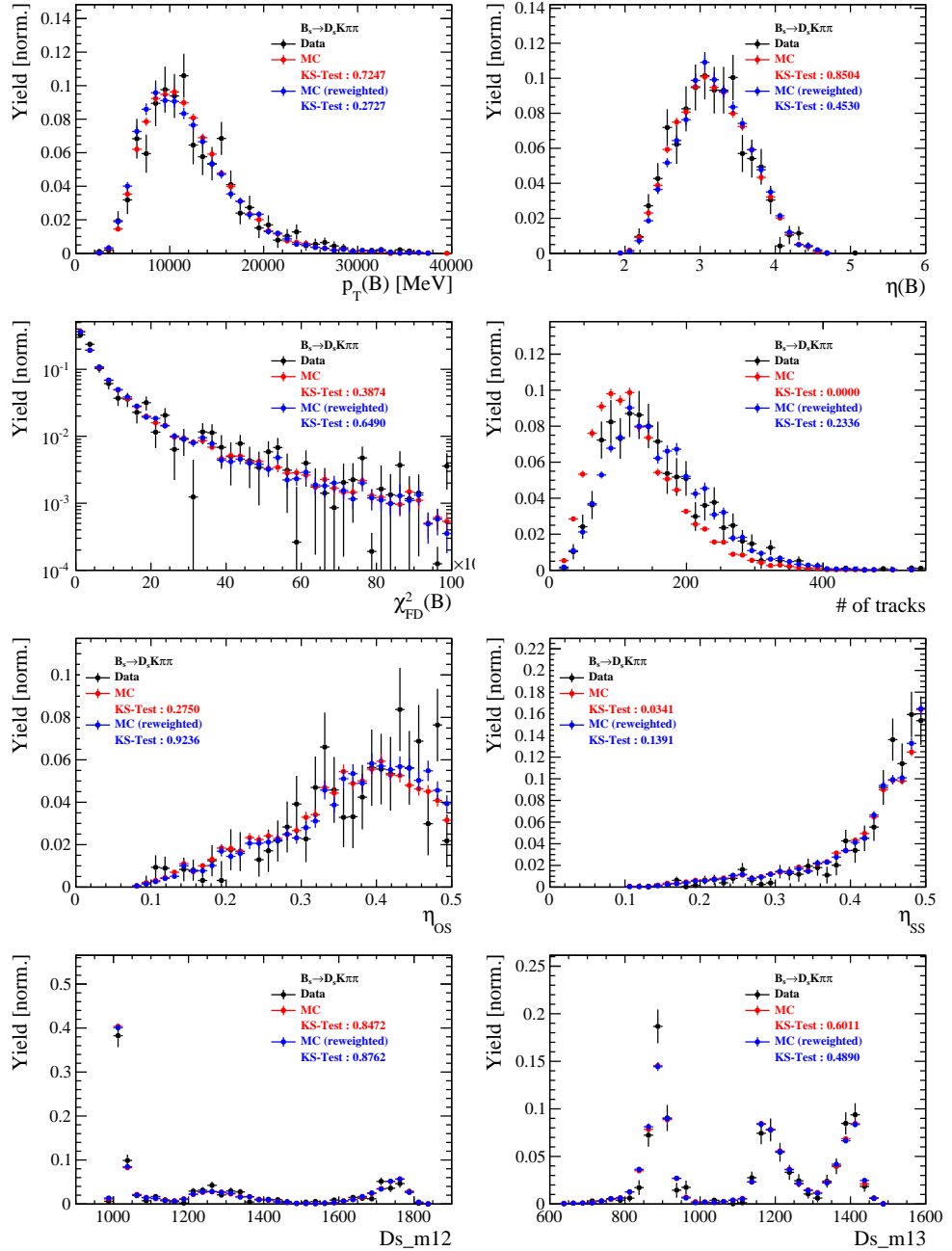


Figure 4.4: Comparison of selected variables for $B_s \rightarrow D_s K\pi\pi$ decays.

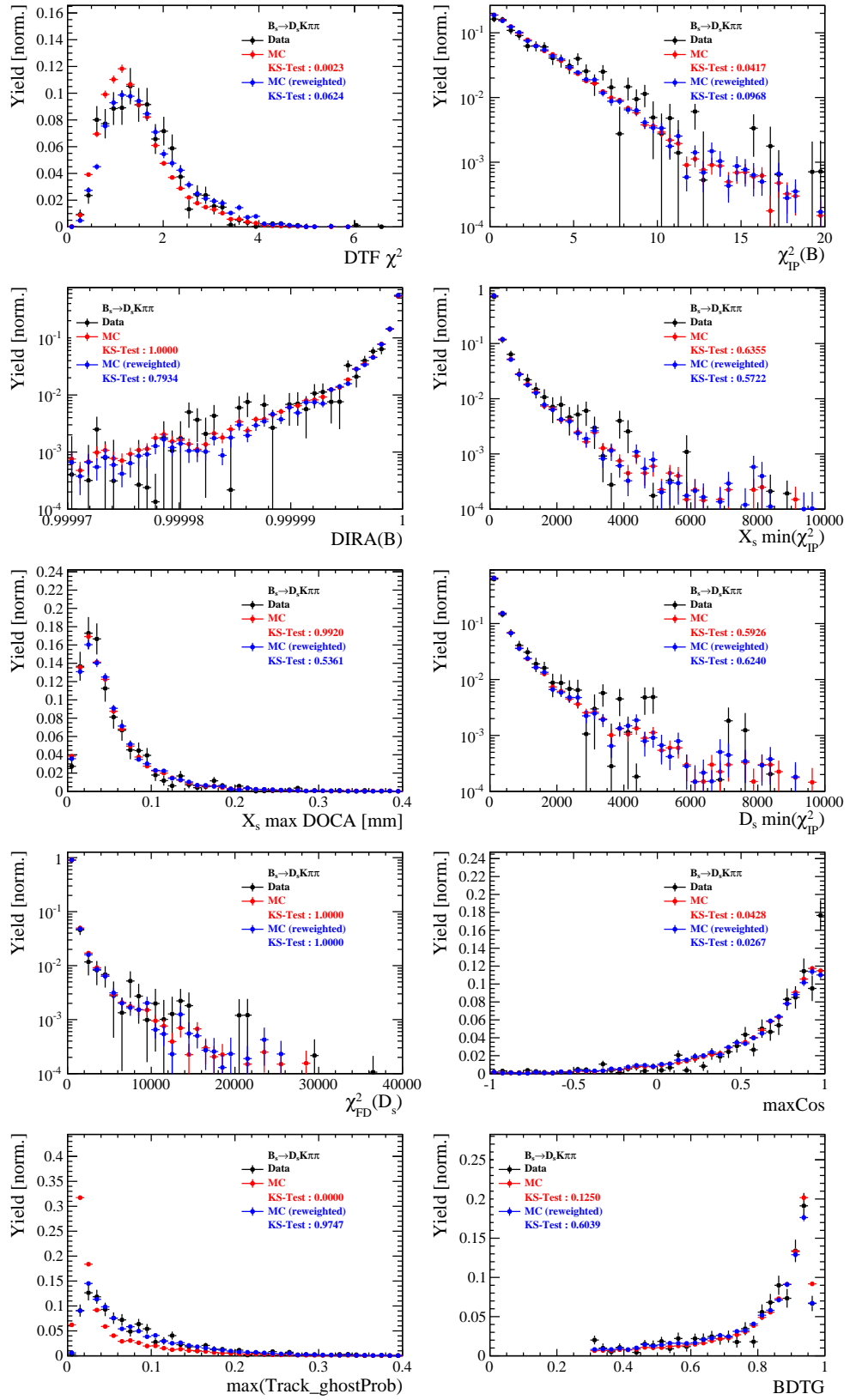


Figure 4.5: Comparison of BDTG input variables and classifier response for $B_s \rightarrow D_s K \pi \pi$ decays.

589 **E Data distributions**

590 **E.1 Comparison of signal and calibration channel**

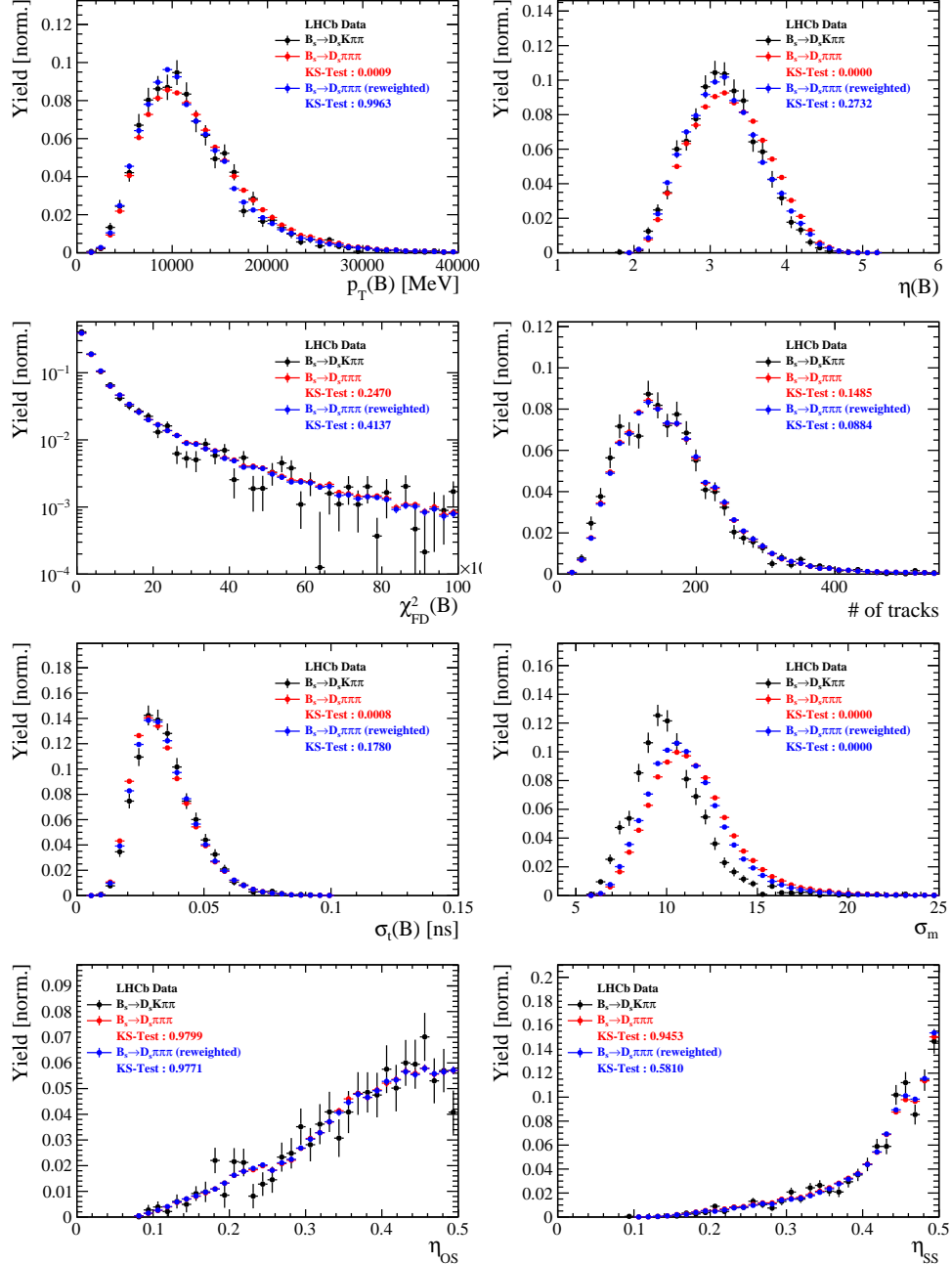


Figure 5.1: Comparison of selected variables.

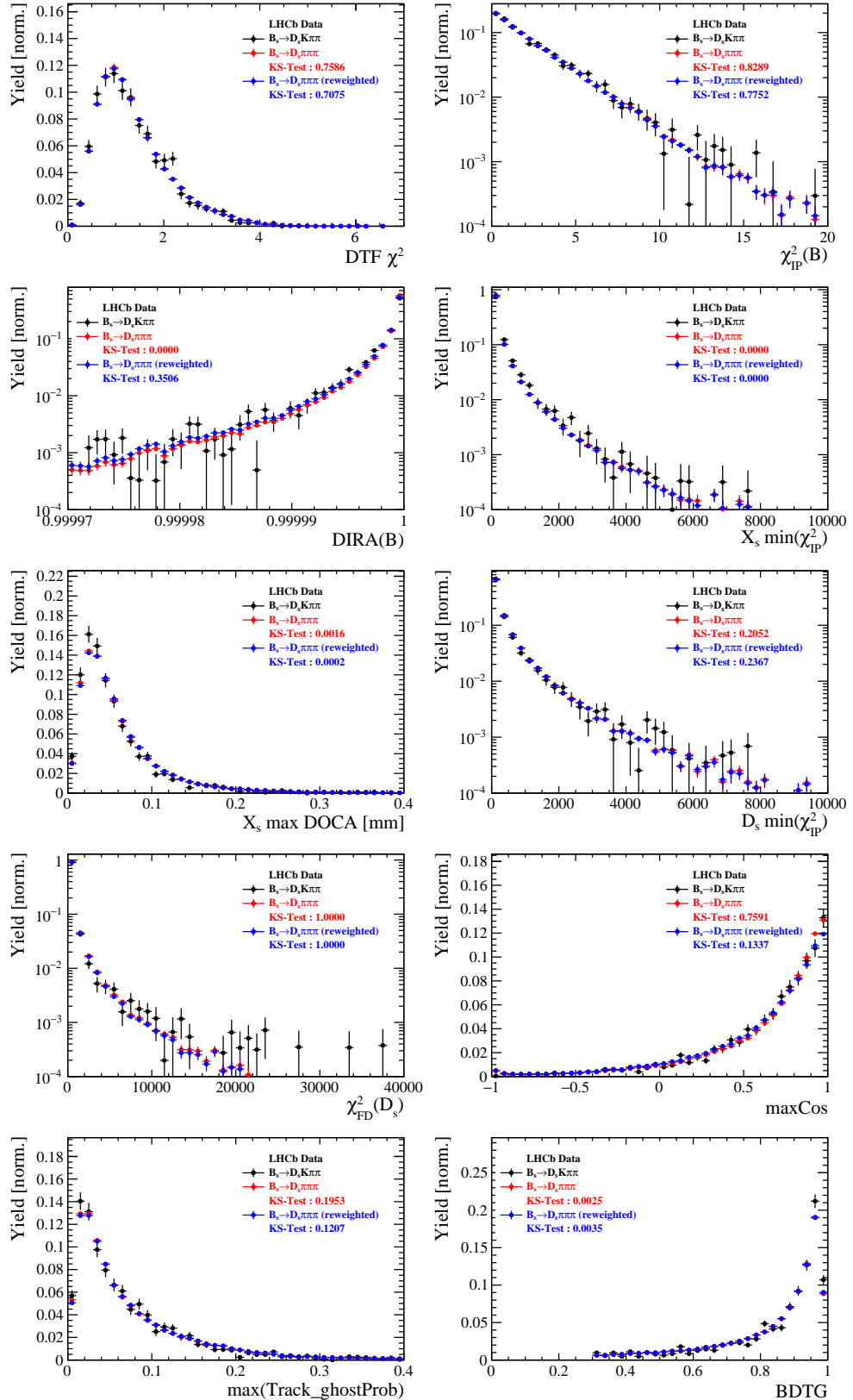


Figure 5.2: Comparison of BDTG input variables and classifier response.

591 E.2 Comparison of Run-I and Run-II data

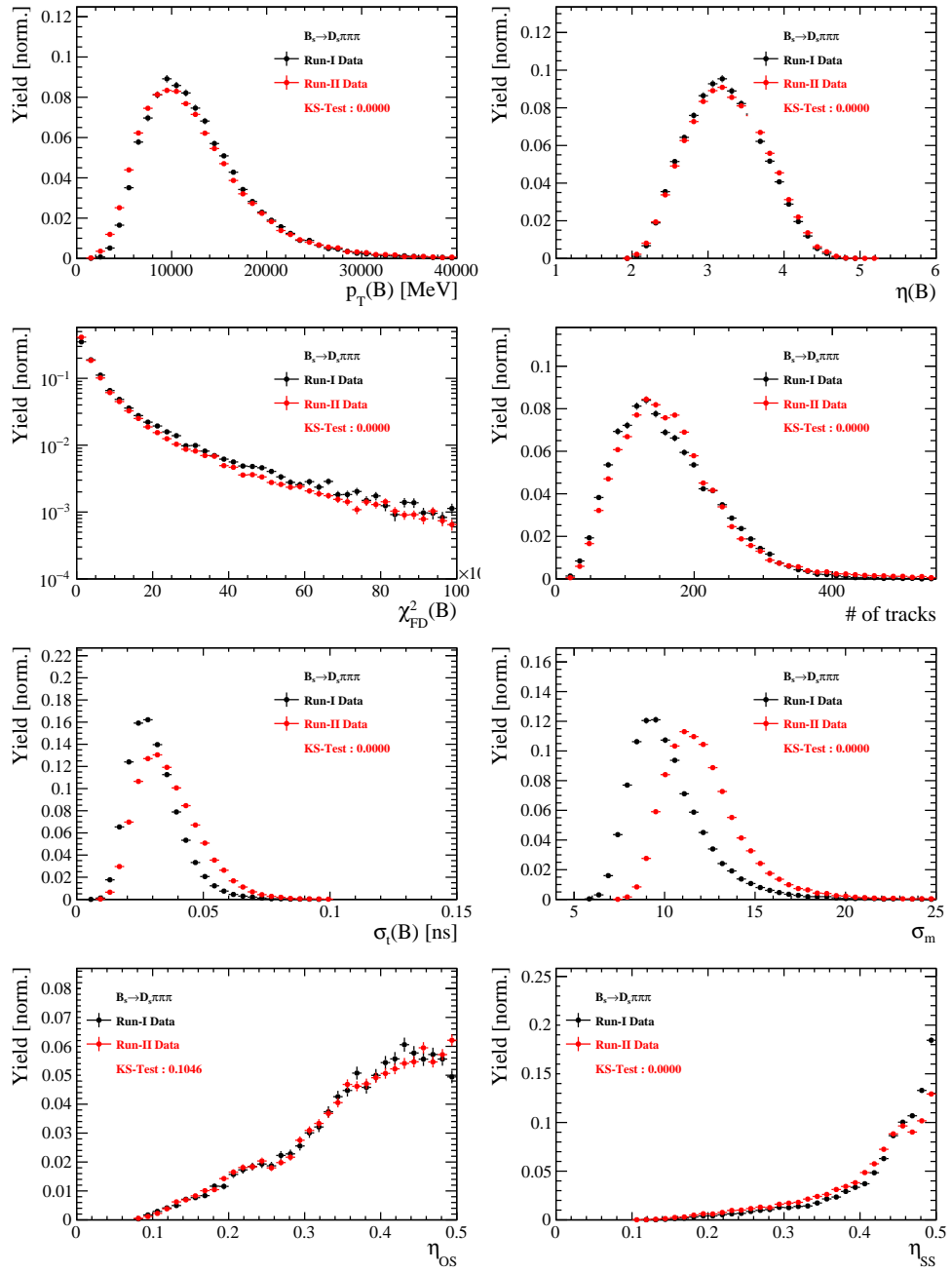


Figure 5.3: Comparison of selected variables.

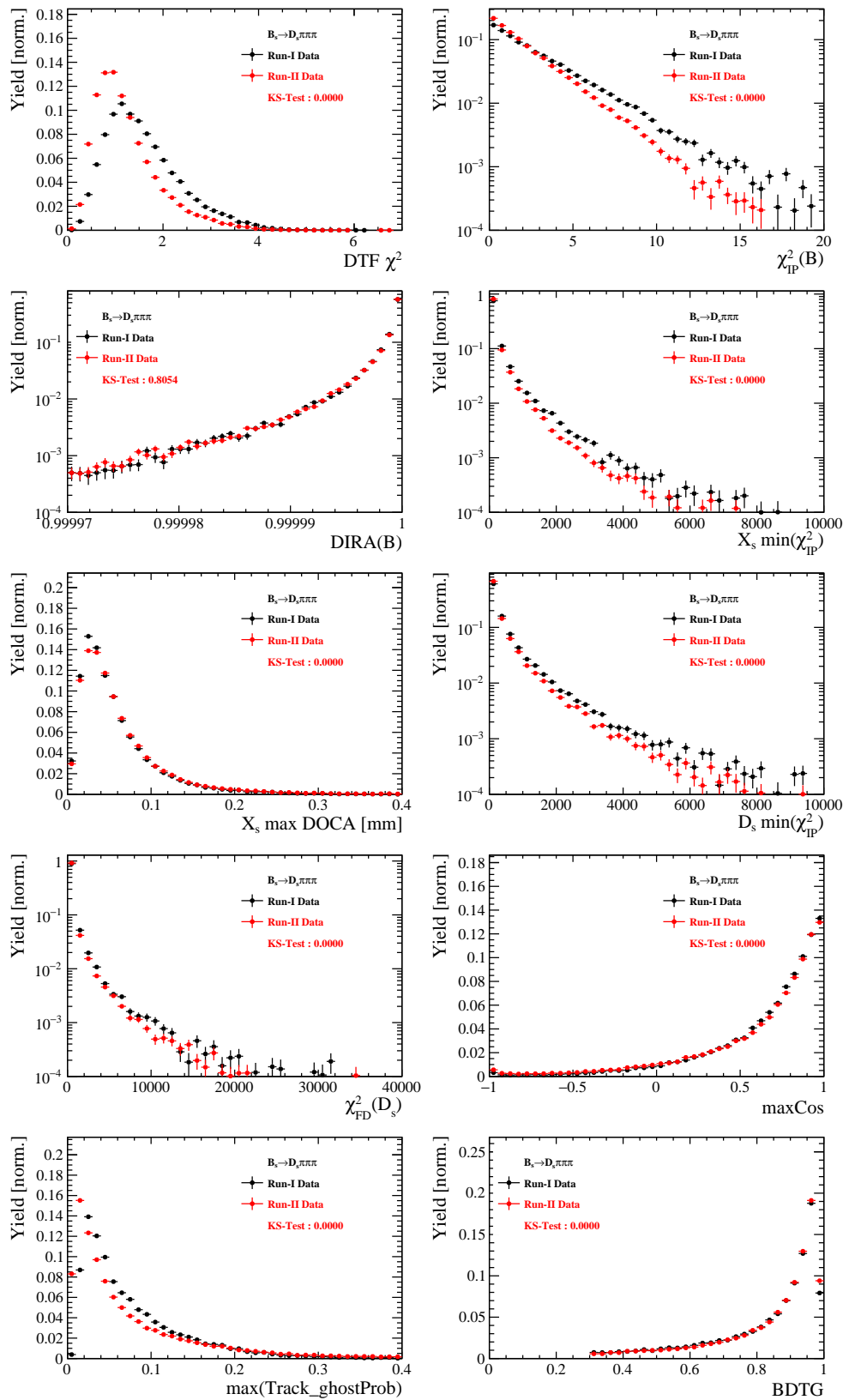


Figure 5.4: Comparison of BDTG input variables and classifier response.

592 E.3 Comparison of D_s final states

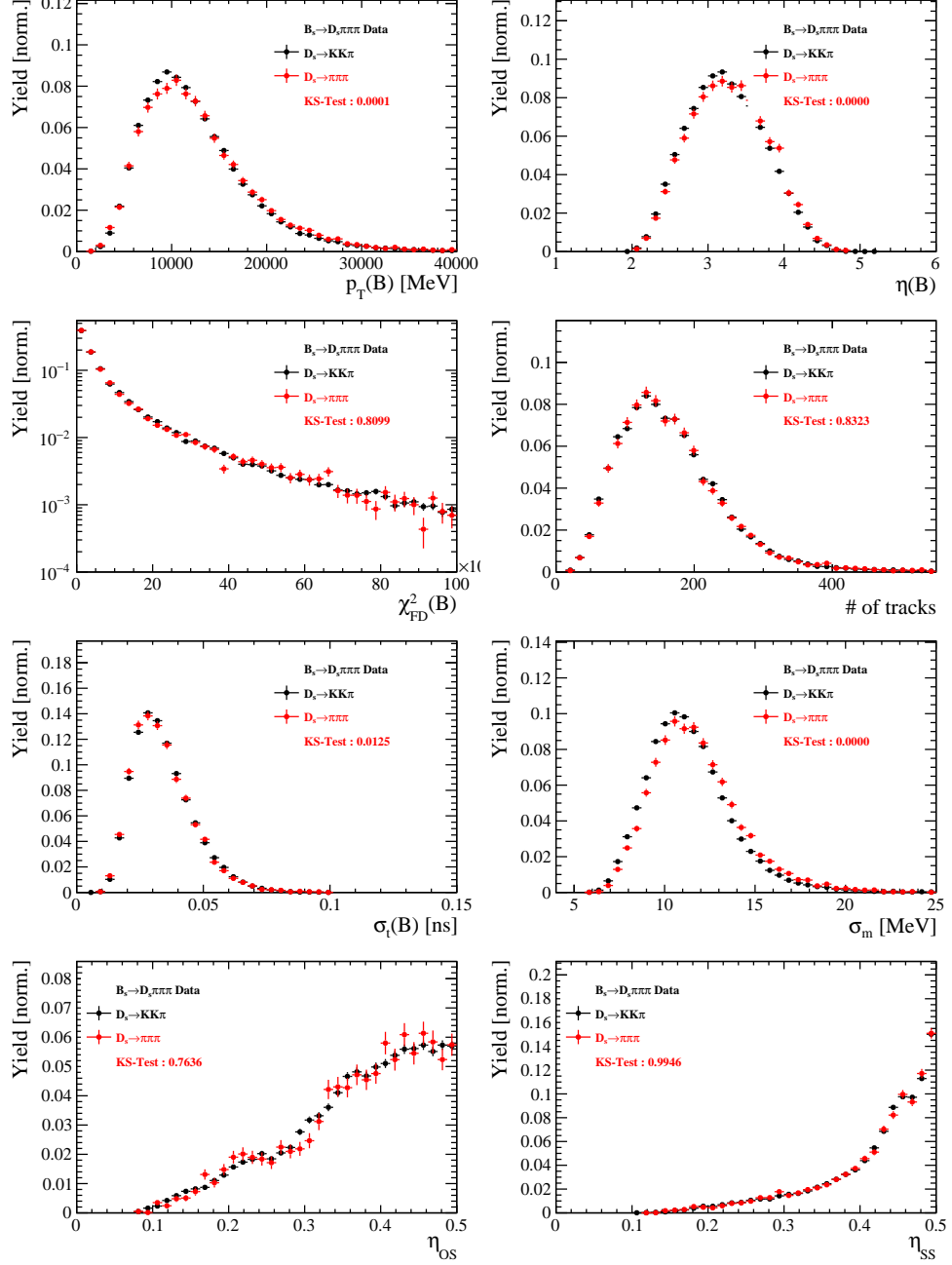


Figure 5.5: Comparison of selected variables.

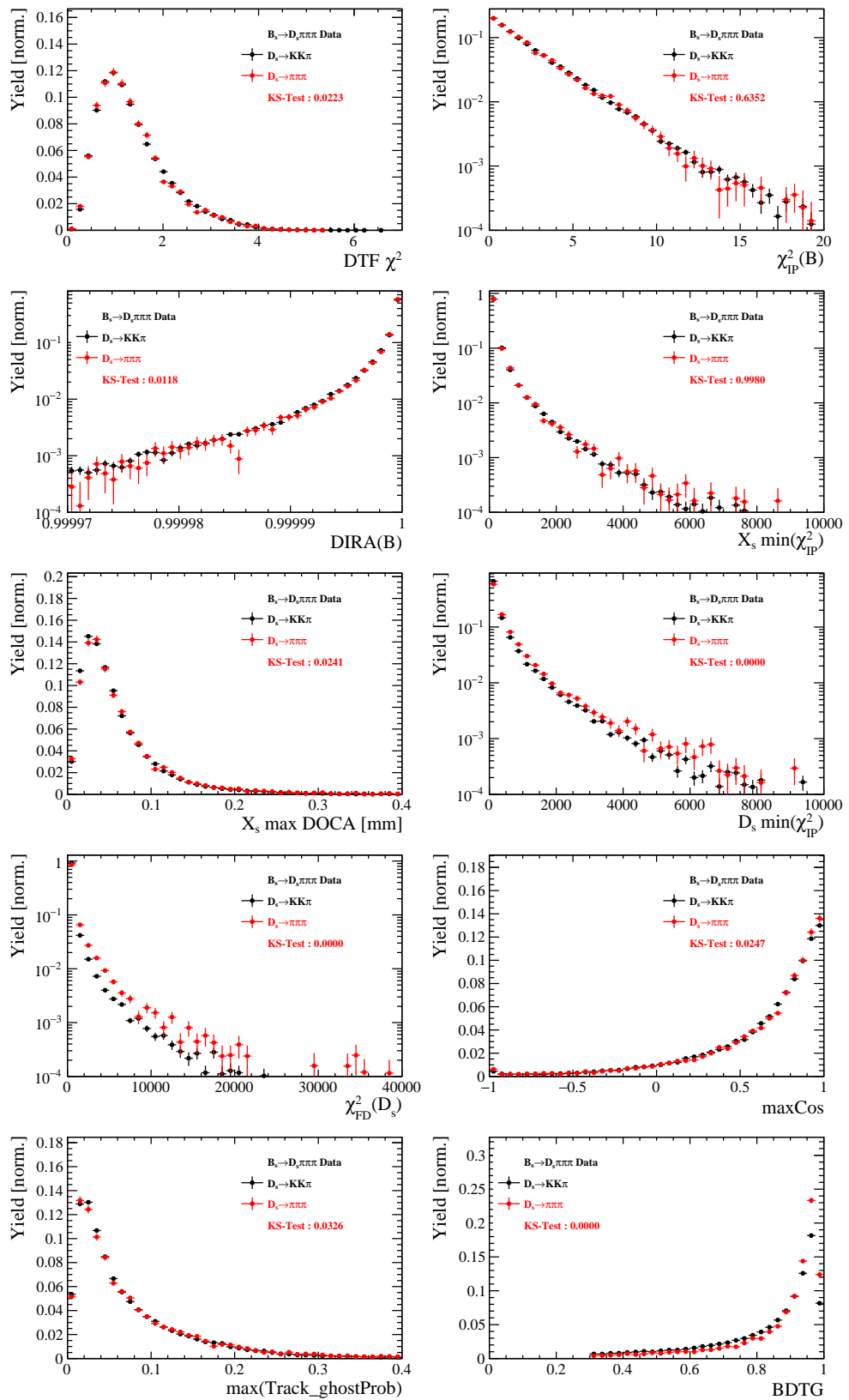


Figure 5.6: Comparison of BDTG input variables and classifier response.

593 E.4 Comparison of trigger categories

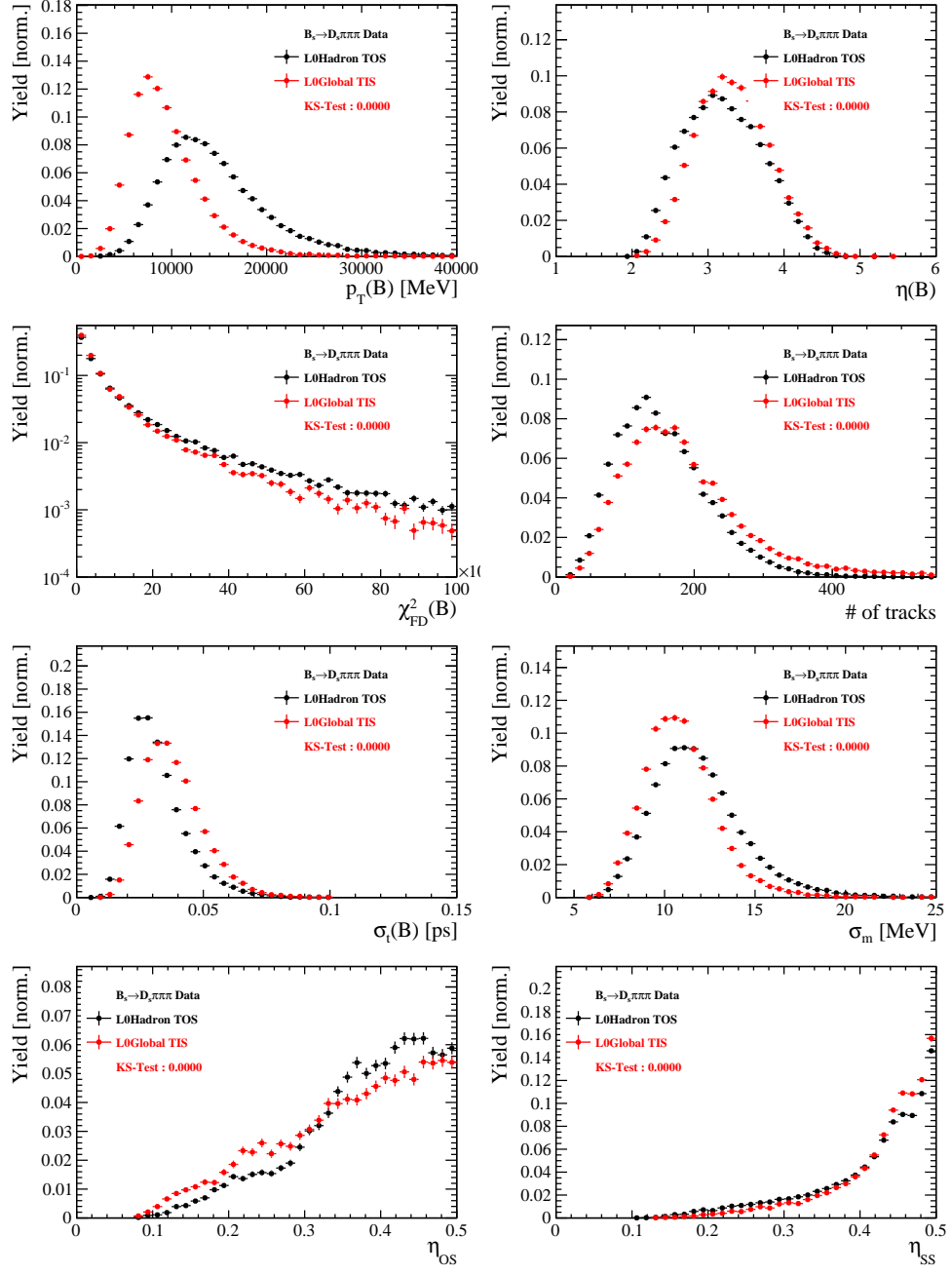


Figure 5.7: Comparison of selected variables.

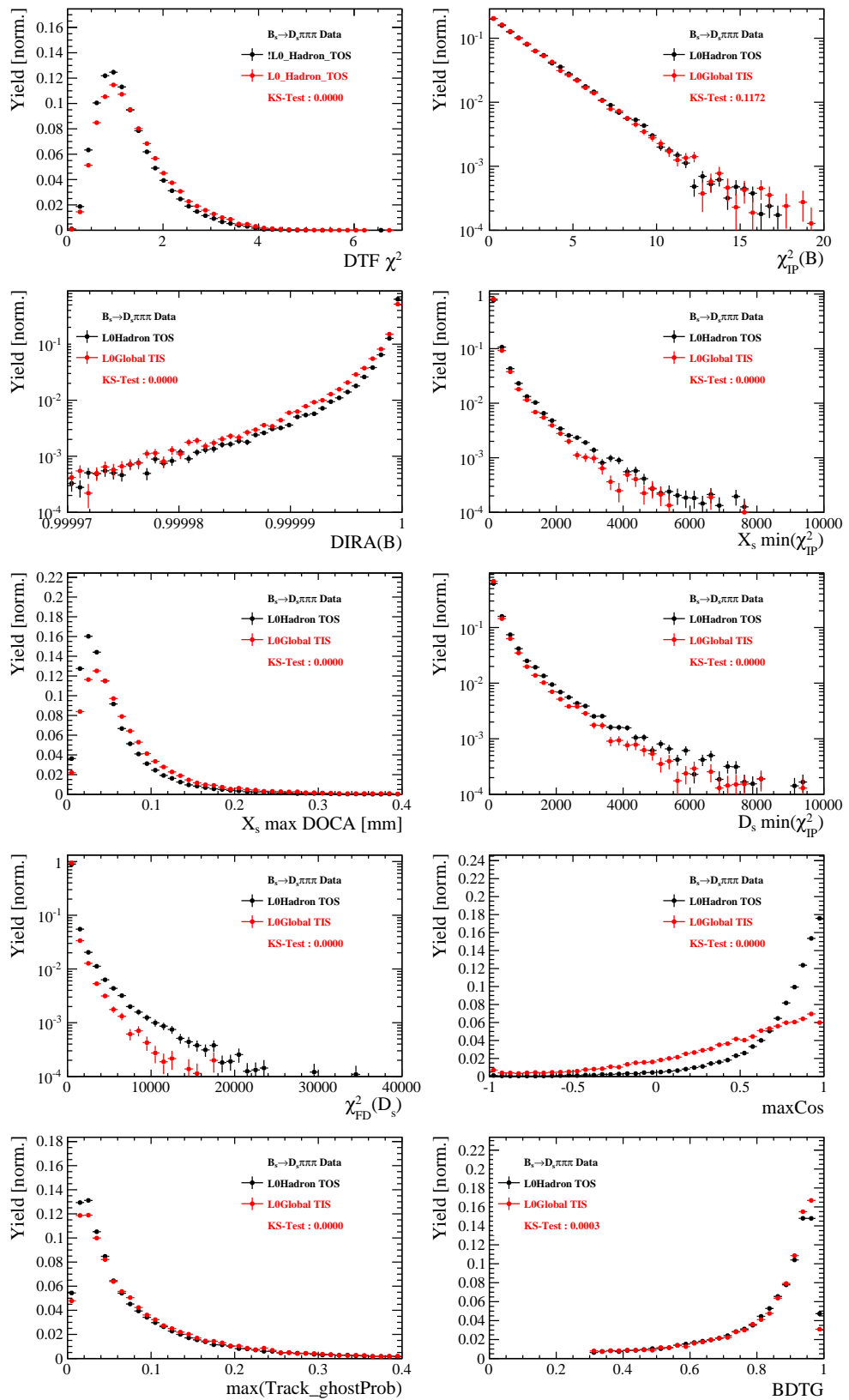


Figure 5.8: Comparison of BDTG input variables and classifier response.

594 E.5 Comparison of B_s and B_d decays

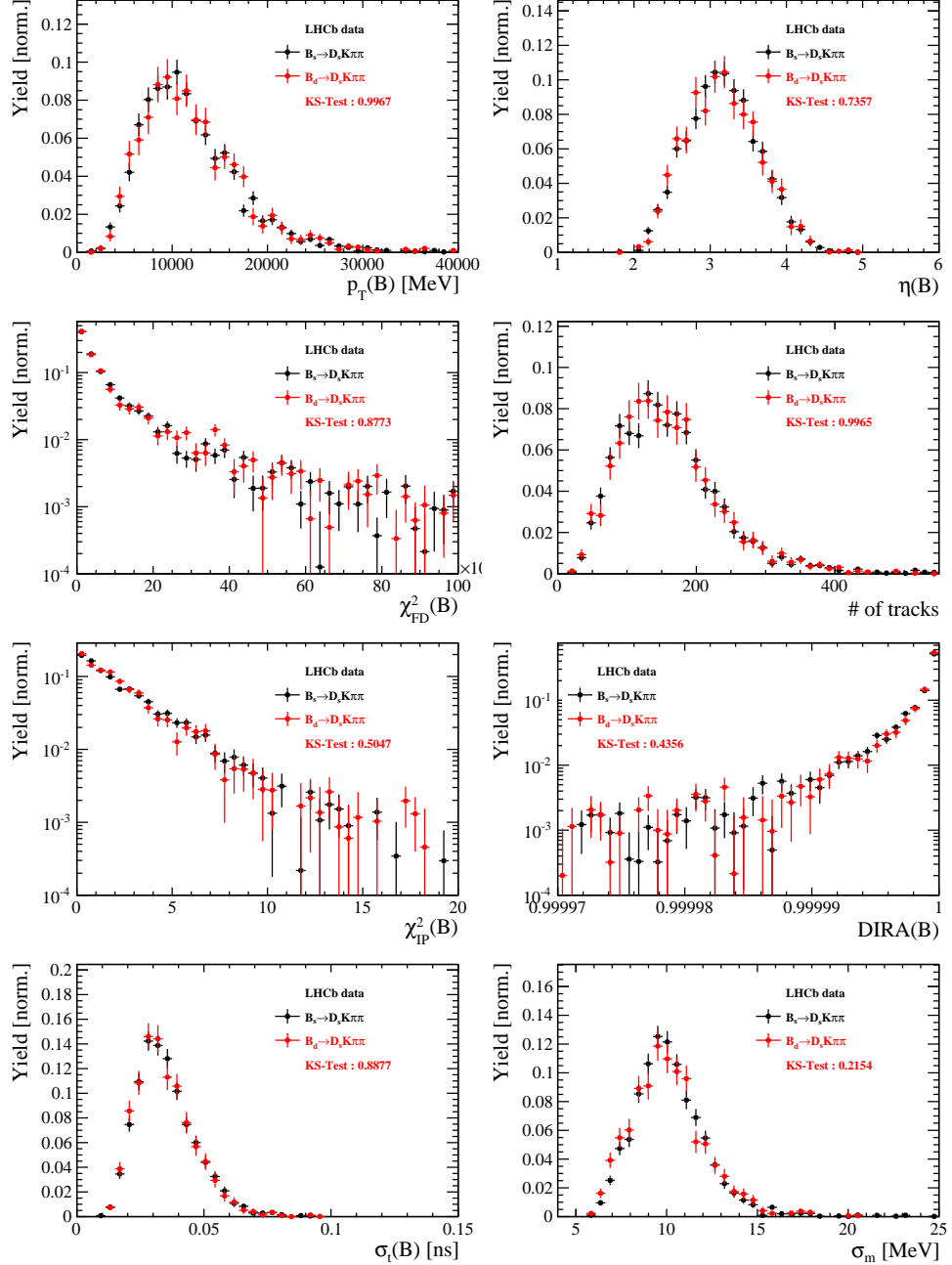


Figure 5.9: Comparison of selected variables.

595 References

- [596] [1] R. Fleischer, *New strategies to obtain insights into CP violation through $B(s) \rightarrow D(s)$, $D(s) \rightarrow K\pi$, $D(s)^* \rightarrow K\pi$, ... and $B(d) \rightarrow D\pi$, $D^* \rightarrow \pi\pi$, ... decays*, Nucl. Phys. **B671** (2003) 459, [arXiv:hep-ph/0304027](#).
- [599] [2] K. De Bruyn *et al.*, *Exploring $B_s \rightarrow D_s^{(*)\pm} K^\mp$ Decays in the Presence of a Sizable Width Difference $\Delta\Gamma_s$* , Nucl. Phys. **B868** (2013) 351, [arXiv:1208.6463](#).
- [601] [3] S. Blusk, *First observations and measurements of the branching fractions for the decays $\bar{B}_s^0 \rightarrow D_s^+ K^- \pi^+ \pi^-$ and $\bar{B}^0 \rightarrow D_s^+ K^- \pi^+ \pi^-$* .
- [603] [4] LHCb, S. Blusk, *Measurement of the CP observables in $\bar{B}_s^0 \rightarrow D_s^+ K^-$ and first observation of $\bar{B}_{(s)}^0 \rightarrow D_s^+ K^- \pi^+ \pi^-$ and $\bar{B}_s^0 \rightarrow D_{s1}(2536)^+ \pi^-$* , 2012. [arXiv:1212.4180](#).
- [605] [5] A. Hoecker *et al.*, *TMVA: Toolkit for Multivariate Data Analysis*, PoS **ACAT** (2007) 040, [arXiv:physics/0703039](#).
- [607] [6] M. Pivk and F. R. Le Diberder, *sPlot: A statistical tool to unfold data distributions*, Nucl. Instrum. Meth. **A555** (2005) 356, [arXiv:physics/0402083](#).
- [609] [7] N. L. Johnson, *Systems of frequency curves generated by methods of translation*, Biometrika **36** (1949), no. 1/2 149.
- [611] [8] Particle Data Group, K. A. Olive *et al.*, *Review of particle physics*, Chin. Phys. **C38** (2014) 090001, and 2015 update.
- [613] [9] LHCb, R. Aaij *et al.*, *A new algorithm for identifying the flavour of B_s^0 mesons at LHCb*, JINST **11** (2016), no. 05 P05010, [arXiv:1602.07252](#).
- [615] [10] LHCb collaboration, R. Aaij *et al.*, *Opposite-side flavour tagging of B mesons at the LHCb experiment*, Eur. Phys. J. **C72** (2012) 2022, [arXiv:1202.4979](#).
- [617] [11] Heavy Flavor Averaging Group, Y. Amhis *et al.*, *Averages of b-hadron, c-hadron, and τ -lepton properties as of summer 2014*, [arXiv:1412.7515](#), updated results and plots available at <http://www.slac.stanford.edu/xorg/hfag/>.
- [620] [12] T. M. Karbach, G. Raven, and M. Schiller, *Decay time integrals in neutral meson mixing and their efficient evaluation*, [arXiv:1407.0748](#).
- [622] [13] LHCb collaboration, R. Aaij *et al.*, *LHCb detector performance*, Int. J. Mod. Phys. **A30** (2015) 1530022, [arXiv:1412.6352](#).
- [624] [14] LHCb, R. Aaij *et al.*, *Measurement of CP asymmetry in $B_s^0 \rightarrow D_s^\mp K^\pm$ decays*, Submitted to: JHEP (2017) [arXiv:1712.07428](#).
- [626] [15] H. Gordon, R. W. Lambert, J. van Tilburg, and M. Vesterinen, *A Measurement of the $K\pi$ Detection Asymmetry*, Tech. Rep. LHCb-INT-2012-027. CERN-LHCb-INT-2012-027, CERN, Geneva, Feb, 2013.

- 629 [16] A. Davis *et al.*, *Measurement of the instrumental asymmetry for $K^- \pi^+$ -pairs at LHCb*
630 *in Run 2*, Tech. Rep. LHCb-PUB-2018-004. CERN-LHCb-PUB-2018-004, CERN,
631 Geneva, Mar, 2018.
- 632 [17] I. I. Y. Bigi and H. Yamamoto, *Interference between Cabibbo allowed and doubly*
633 *forbidden transitions in $D \rightarrow K(S), K(L) + \pi$'s decays*, Phys. Lett. **B349** (1995)
634 363, arXiv:hep-ph/9502238.